A Computational Study of Hydrogen-bonded Molecular Crystals

Martin Walker

Abstract

The current climate in research has focused on the rational design of new materials with desirable characteristics. The demand for their full characterisation has in turn placed a new importance on structural chemistry, and important developments have taken place as a consequence. For instance an important probe to understand the interactions between molecules is to use variable pressure, and this has been exploited experimentally through the design and implementation of the diamond anvil compression cell (DAC). Using a DAC to study molecular materials at high pressure can result in problems, however: in X-ray diffraction the physical presence of the cell restricts access to reciprocal space, resulting in experimental structures of lower precision and often missing hydrogen atom location data. Traditionally the solution has been sought in neutron diffraction where hydrogen (deuterium) atoms scatter more intensely and so contribute more to the scattering pattern. This introduces another set of problems, however, in that the assumption is made that the isotope substitution does not alter the overall structure. In addition expense and time delays are incurred through this protracted experimental route.

This thesis reports the development of a computational technique which can be used to reliably locate hydrogen atoms without the need for neutron diffraction data. The project reports rigorous testing on cases of varying difficulty, from the simple to the more complex. The test cases selected were also of industrial and environmental importance, so determining their complete structures under high pressure conditions was in itself a desirable outcome. Computationally completed structures were then compared to neutron diffraction results or used as the model to be refined against the neutron diffraction pattern.

Acknowledgements

I would like to acknowledge help from a number of people whom I have relied on for knowledge and support throughout my PhD. Dr. Carole Morrison, my supervisor, who has proved instrumental in motivation, finding new directions to take my work and much, much more. Dr. David Allan, who performed much of the crystallography. Prof. David Rankin for making me welcome within his group and sharing his vast academic knowledge. Dr Simon Parsons for teaching me crystallography and acting as my second supervisor. Dr Colin Pulham for answering all my spectroscopy queries. Dr. Bill Marshall for performing neutron studies. All members of each of these groups, past and present, for providing and integrating me into a social and academic network.

I would like to thank my friends and family for their patience and tolerance allowing me to work free from outside concerns.

Declaration

This thesis has been written entirely by me and has not been submitted in any previous application for a degree. Except where stated, all the work detailed in this thesis has been carried out by me. Some original work in this thesis has been reported in the published papers listed in Appendix 2.

Martin Walker

Table of Contents

Chapter 1

Introduction to First-Principles Calculations

In 1933 Paul Dirac and Erwin Schrodinger shared the Nobel Prize in physics "for the discovery of new productive forms of atomic theory." Atomic theory describes the nature of matter, which is divided into atoms, upon which the laws of mathematics are applied in order to describe their motion. Since, in principal, only physical constants are required the properties of matter are calculated entirely from first principles.

Atomic theory thus provided the underlying physics to understand the nature of matter. Direct application of the theory, however, yielded problems and as Dirac stated:

"*The fundamental laws necessary for the mathematical treatment of a large part of physics and the whole of chemistry are thus completely known, ……and the difficulty lies only in the fact that application of these laws leads to equations that are too complex to be solved*."[1]

Whilst in general Dirac's statement is correct it refers to an exact solution, which remains unobtainable to this day. By taking onboard some simple approximations, however, workable solutions are available. Work in this field yielded another Nobel prize in 1998 to Walter Kohn "for his development of the density-functional theory" and John A. Pople "for his development of computational methods in quantum chemistry." Nowadays, atomistic simulations find applications across all branches of the physical sciences, e.g. the rational design of materials for use in fusion reactors[2], rational drug design, catalytic pathway and studies protein folding studies[3].

Simulations are by no means flawless, and the approximations and assumptions used are not always applicable to every situation. For example, one of the most widely used assumptions is the Born Oppenheimer (B-O) approximation, which states that, since the nuclei move very slowly relative to the electrons, they can be regarded as stationary within an electric potential. Whilst the validity of the B-O approximation has been shown with time, in certain situations it fails to predict

experimental observables. For example it prevents atoms from quantum tunnelling, and if it proved necessary to describe this phenomenon in the simulation more complicated modelling techniques need to be applied to allow for this.

There are many different theories applied to first-principle simulations (ab initio - based on molecular wavefunction, DFT - based on electron density) and within each, approximations give rise to a hierarchy of calculations; from the basic to the very sophisticated. The different assumptions each different theory adopts can have associated pitfalls. The modeller is therefore required to carefully select a theory which will best suit the needs of the system leading away from a "one size fits all" approach. In selecting an appropriate theory the modeller must take into account the size and complexity of the system; large systems can take a prohibitively long time to run and so approximations to further simplify the system are required, whilst complex systems may need a more physical representation and so assumptions cannot be made. In all cases utmost on the mind of computational modellers is that the system to be modelled is realistic. Simulations are rarely regarded as a complete entity, experiments are still required to confirm results and in many cases experiments provide an initial point from which the simulations extend.

The purposes of simulations can be roughly placed in three groups:

- *Prediction* – simulations are used to predict the properties of a material to guide experimentalists towards their eventual goal, e.g. lead drug development.
- *Unavailable experiment* – simulations are used where experimental conditions are too dangerous, or expensive or just inaccessible, e.g. modelling of the earth's core.
- *Recreation* – simulations are used to recreate experimental observables to better explain experiments or to develop theoretical techniques.

Recent software and hardware developments have allowed researchers to extend gas phase simulations and model the condensed phase. With this a new demand has been placed on simulations to aid in the rational design of new materials with desirable characteristics. One valuable experimental probe is the application of

pressure to test the nature of interactions between molecules. Experimentally the diamond anvil compression cell can be used, with the resulting high-pressure crystal structures obtained in a standard X-ray diffractometer. A number of problems are associated with this procedure, however, with the most serious being that hydrogen atom positions are often impossible to locate. This limitation is particularly critical for molecular materials where the dominant packing force between molecules tends to be hydrogen bonding. Prior to the availability of reliable computational modelling the only routes to completing high-pressure crystal structures were either manual, based on experimental intuition on the part of the crystallographer, or the expensive and time-consuming option of a neutron diffraction study.

Simulations have been used locate hydrogen atoms in ambient pressure structures. Milman and Winkler[4] took a selection of complex inorganic systems and calculated the hydrogen atom positions. The resulting structures met experimental observations and were found to be a considerable improvement over structures prior to the computational treatment.

The work presented in this thesis reports on the development of new computational procedures to identify the most likely positions of hydrogen atoms in a series of compounds studied by high pressure X-ray crystallography. Compounds investigated were sodium formate dihydrate, nitric acid monohydrate, nitric acid dihydrate, acetic acid and hydroxylamine. X-ray experiments were used to provide heavy-atom positions and unit-cell parameters. In many cases the simulated results were obtained prior to gaining access to neutron facilities, allowing the theoretical models to be used as the initial models in the neutron diffraction refinements. In this way the results obtained from the modelling work could be validated.

References

[1] P. Dirac, *Proc Roy. Soc*. **123**, 714, 1929.

[2] A. D. Turnbull, D.P. Brennan, M. S. Chu, L. L. Lao, *Fusion Science and Technology,* **48**, 875, 2005.

[3] V. Daggett, *Chem. Rev*. **106**, 1898, 2006.

[4] V. Milman, B. Winkler, *Ziet. f. Kris*., **216**, 99, 2001.

Chapter 2

Experimental and Computational Methods

2.1 Introduction to Diffraction methods

It is hard to understate the importance of diffraction methods in modern chemical research. Determining the structure of a material in the solid state (its 'crystal structure') is a routine chemical analysis tool, and a highly desirable step towards obtaining full structural characterisation.

In its simplest form the diffraction of radiation by matter can be considered as an extension to Young's slit experiment,[1] where a beam of monochromatic light (of wavelength λ) passes through slits separated by a distance '*d*'. The resulting diffraction pattern is cast onto a screen of distance '*L*' from the slits (Figure 2.1). Young hypothesised that the light could interfere coherently or incoherently to build up a diffraction pattern which followed the equation

$$\frac{n\lambda}{d} = \frac{x}{L} \qquad \textbf{Equation 2.1}$$

where *x* is the distance between the bands of light and *n* is an integer where a band is present [also referred to as the order of the band (zero for the central band)].

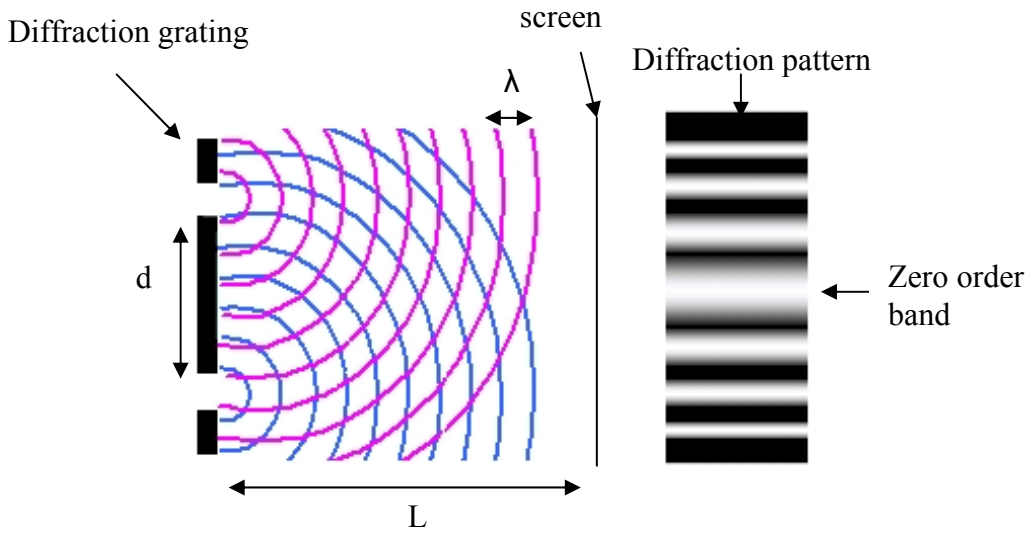

Figure 2.1. Schematic diagram of Young's slit experiment. Wave crests of radiation originating from the upper slit (pink) interacting with those originating from the lower slit (blue) result in light bands (coherent radiation); crests interacting with troughs cancel out, leading to dark bands (incoherent radiation).

Young used Equation 2.1 to determine the wavelength of the light used (as *d* and *L* were known). In modern diffraction experiments the atoms in a crystal act as the slits, and in order to generate a clear diffraction pattern (i.e. *d* and λ to be of similar magnitude), the beam of light is replaced by an X-ray or neutron beam. In this way if the wavelength of light is known the distance between the atoms can be calculated. In practice copper or molybdenum are used as anodes and produce X-rays with wavelengths of 0.70926 Å and 1.54051 Å, respectively.

Naturally, actual crystal diffraction[2] is considerably more complicated than a simple two-slit experiment. A crystal contains many atoms in three dimensions,

which can be described as a periodic repeat of the simplest irreducible unit referred to as a unit cell (Figure 2.2).

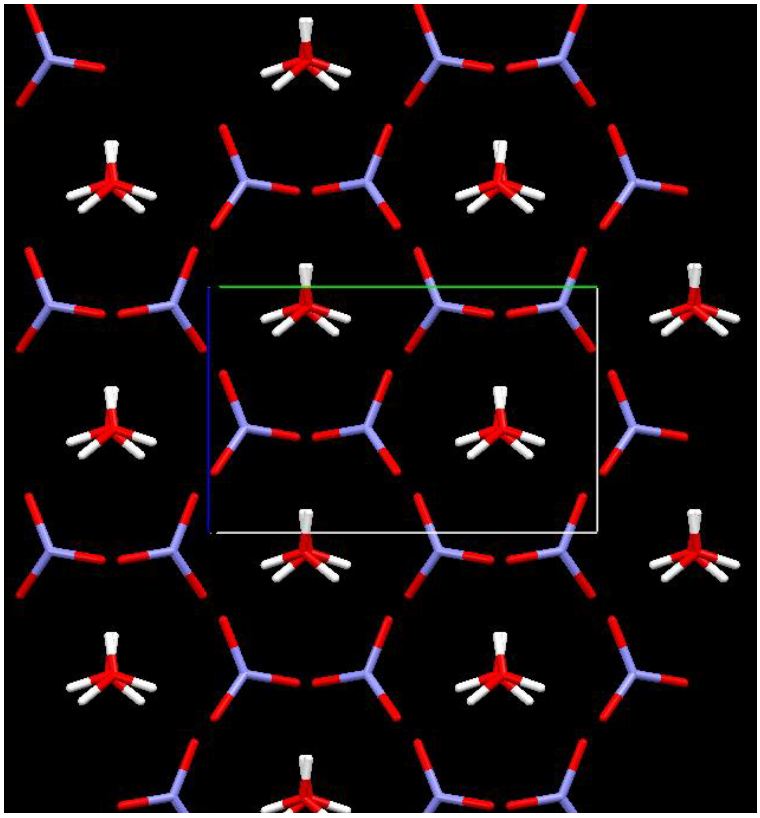

Figure 2.2. The crystal structure of nitric acid monohydrate. The boxed area represents the smallest repeating unit, i.e. a unit cell.

Since the unit cell is no longer a simple 1-dimensional distance but a complete set of 3D coordinates, the resulting diffraction pattern is no longer a series of bands but instead a set of distinct spots, spread out in three-dimensional reciprocal space (also referred to as an Ewald sphere, see Figure 2.3).

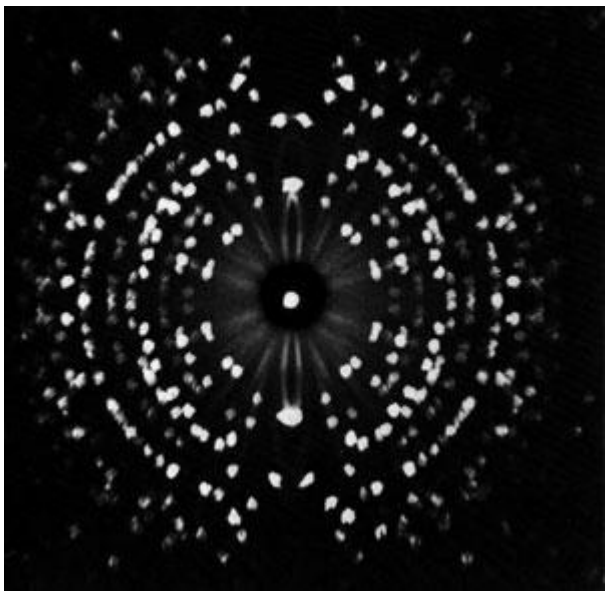

Figure 2.3 A diffraction pattern from a single aluminium potassium sulfate crystal[3]

A unit cell is easily obtained from the first few reflections. The positions of the diffraction spots determine the unit cell (in effect the diffraction pattern is the unit cell in reciprocal space). The distances between the spots are converted from reciprocal space to meaningful atomic distances using the Bragg law (Equation 2.2), which can be easily visualised as diffraction from two planes spaced by a distance, d (Figure 2.4).

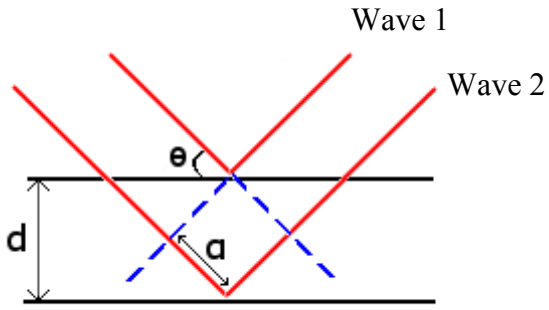

Figure 2.4. Wave 2 has travelled a distance of 2α further than wave 1. If 2α is an integer value of the X-ray wavelength used then the waves will interfere coherently. If, however, the value of 2α is not an integer value then the cosine waves will interact incoherently, and given enough planes will provide no scattering. Changing the angle θ will alter the distance 2α. In that way a tuneable X-ray source is not required to scan all possible distances.

The distance between the diffracting planes can be calculated using the Bragg equation:

$2d \sin\theta = n\lambda$ **Equation 2.2**

Where d is the distance between planes, θ is the diffraction angle and λ is the X-ray wavelength.

The positions of the spots in a diffraction pattern are based on translational symmetry, for example a translation of a complete unit cell along one of its axis will superimpose perfectly on the crystal environment. Each translational symmetry element will be responsible for a different aspect of the diffraction pattern. Crystals

which possess the same symmetry elements are grouped together into space groups. In some cases the choice of a larger unit cell can result in a larger number of symmetry operations that are applicable. Such cells are referred to as centred cells, with the smaller cell referred to as the primitive. Whilst translational symmetry dictates the position of the spots, the relative intensities of the spots are related to the atom scattering. A heavy atom with many electrons (e.g. iodine) will scatter X-rays strongly and produce bright reflections, whilst a light atom with only one electron (i.e. hydrogen) will produce much lower intensity reflections. The net effect of this is that in a diffraction experiment the hydrogen atoms are difficult to locate, especially in the presence of heavy atoms. This is not the case for neutron scattering, where the relative scattering power of a particular element (and isotope) is dictated by its neutron scattering factor (Table 2.1).

Atomic Nucleus	Neutron scattering factor (fm)	Coherent scattering cross section (10^{-24} cm^2)	Incoherent scattering cross section (10^{-24} cm^2)	Absorbance (10^{-24} cm^2)
^{1}H	- 3.741	1.8	80.3	0.3
^{2}D	+ 6.671	5.6	2.1	0.0
B	+ 5.304	3.5	1.7	767.0
C	+ 6.646	5.6	0.0	0.0
N	+ 9.362	11.0	0.5	1.9
O	+5.803	4.2	0.0	0.0

Table 2.1. Neutron scattering lengths (scattering factors) of selected atoms[4].

Note the large incoherent scattering cross section of hydrogen, the result of which is that a large background scattering is recorded and any coherent scattering is difficult to observe. To rectify this deuterium, which has a much lower incoherent scattering cross section, is used in the place of hydrogen. As the two elements are essentially the same the assumption is made that deuterating the sample will not change the structure. Naturally this assumption will not always hold, in cases where entropy (free energy) is responsible for structural components, deuteration may dramatically alter the structure.

2.1.1 Diffraction samples

Crystal diffraction can be observed from two different types of material: single crystal or powder (essentially a large collection of crystallites). In the former, the diffracting planes are composed from atoms in the crystal lattice. The crystal is rotated in three dimensions so that a complete Ewald sphere may be generated. In some cases symmetry will reduce the number of angles that are required to build a full sphere of diffraction. Deuterating the sample is less important for single crystal neutron diffraction as the incoherent scattering from the many crystal planes act to cancel out. Powder diffraction makes use of the same basic concepts but, instead of rotating the sample, all angles are harvested based on the assumption that the crystallites in the powder will be randomly arranged to therefore permit all possible diffractions. As each crystal orientation cannot be separated, however, all interatomic distances are represented in a one-dimensional fashion (i.e. a radial distribution curve, or graph of interatomic distance). This loss of data does render powder

patterns tougher to solve, but once a reasonable model is found that is commensurate with the powder pattern it can be trusted to a high level of certainty.

2.2 High pressure X-ray diffraction

Obtaining the crystal structure of a material under conditions of high pressure can be achieved using a diamond anvil cell (DAC) (see Figure 2.5).[5] The DAC is a small and simple device which can be mounted easily on a standard X-ray diffractometer. Depending on the specific design of the DAC, external pressures of up to 100 GPa are possible.[6]

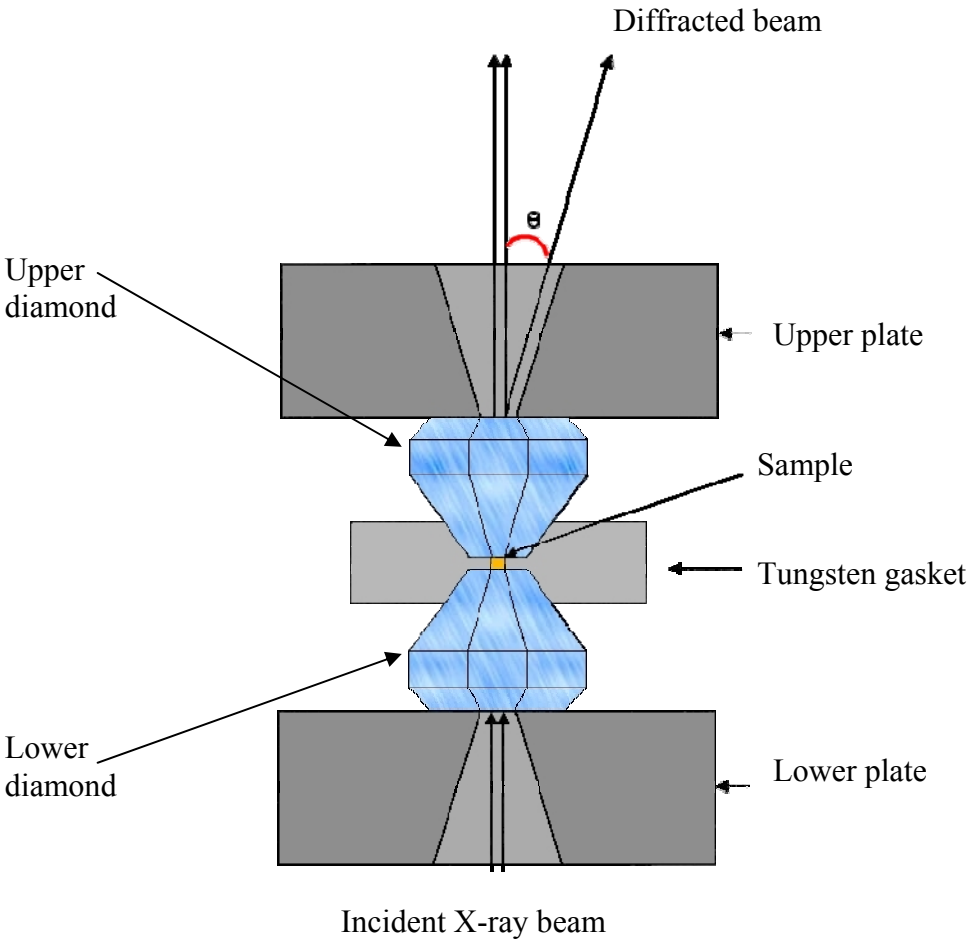

Figure 2.5. Schematic diagram of a diamond anvil cell.

The diamond anvil cell achieves high pressures by squeezing two diamonds together by the simple mechanism of tightening screws linking the upper and lower plates; as the point of contact between them is small the pressure achieved is high. The sample is contained by a small hole drilled through a tungsten gasket, with the two diamonds acting as a base and lid. To ensure the applied force is isotropic a liquid such as a methanol/ethanol (4:1) mixture is added.[7] This liquid can only act as a hydrostatic medium as long as it remains as a fluid and so different liquids are required over different pressure regimes. To calibrate the pressure exerted a ruby chip is added to the sample. The frequency of the ruby fluorescence blue shifts as the pressure increases and follows a well established equation, thereby allowing a straightforward determination of the external pressure.[8]

In high-pressure diffraction experiments the presence of the lower plate on the DAC only allows the incident beam to pass through the sample should it fall within a cone permitted by the DAC design; similarly only diffraction which falls within the cone angle on the upper plate can be collected. This greatly limits experimental access to the reciprocal diffraction space, where a typical data collection will be only ca. 30% compared to a standard diffraction experiment. The effect of this is that intensity statistics are greatly reduced. For the heavier atoms this has little impact. For the lighter atoms, however, such as hydrogen, it has greater implications, and often results in a failure of these atoms to be located. Whilst in some cases the hydrogen atoms are of little consequence, there are others in which the lightest of atoms plays a pivotal role in the properties of a material. The obvious examples are molecular compounds, where hydrogen bonding is the dominant

intermolecular interaction largely responsible for dictating the crystal packing arrangement. Thus, the failure to locate hydrogen atoms in these cases is highly unsatisfactory.

To resolve the problems of incomplete structures further experimental techniques can be used. For example, a higher intensity beam can be used to generate the needed reliable intensity statistics. This requires access to a synchrotron radiation source. At this point the experiment loses its 'in house' nature, and carries associated time and financial costs. Similarly, neutron diffraction can be used, but this too can be problematic. Firstly, neutrons are expensive to generate and so central facilities are required, with similar time and financial constraints as incurred with synchrotron experiments. The neutron flux is also much lower than the X-ray flux, and so larger (crystal) samples are required to generate reasonable diffraction patterns. In addition a deuterated sample is required to generate cleaner powder diffraction patterns, and finally a different means of inducing pressure is required. This last problem was overcome with the introduction of the Paris-Edinburgh cell, which achieves high pressures through the use of tungsten carbide anvils and a hydraulic press in a similar manner to that of the DAC. A measurement of pressure is taken by including, for example, NaCl or other similar compounds that have well established equations of state, along with the sample material. The tungsten carbide is effectively transparent to the neutrons and so only the sample is recorded, allowing easy elucidation of the complete high-pressure structure. Neutron diffraction has the added bonus of allowing use of a time-of-flight (TOF) detector, which gives better resolution using a pulsed broadband frequency source. Atomic distances can therefore be calculated

from the angle of diffraction and the time (after pulse) of detection.

2.3 Introduction to Simulations

2.3.1 Gas phase

Gas-phase simulations are the simplest and the basis for more complex techniques, so our discussion will begin here. All properties of matter are related to energy in some form, so finding a solution to Schrödinger's equation ($\hat{H}\Psi=E\Psi$) results in the ability to calculate the properties of matter. It is easier to solve Schrödinger's equation when it is separated into its component form (Equation 2.3).

$$\hat{H} = -\sum_i \frac{\hbar^2}{2m_e} \nabla_i^2 - \sum_k \frac{\hbar^2}{2m_k} \nabla_k^2 - \sum_i \sum_k \frac{e^2 Z_k}{r_{ik}} + \sum_{i<j} \frac{e^2}{r_{ij}} + \sum_{k<l} \frac{e^2 Z_k Z_l}{r_{kl}}$$

Equation 2.3. Schrödinger's equation, where m_e is the mass of an electron, m_k is the mass of nucleus k, i and j correspond to all electrons while k and l correspond to all nuclei, r_{ab} is the distance between particles a and b, Z_k is the atomic number of nucleus k, e is the charge of an electron (1.602×10^{-19} C) and ∇^2 is the Laplacian operator.

From equation 2.3, we observe that the Hamiltonian, $\hat{H}$, is the sum of the kinetic energy of the electrons, the kinetic energy of the nuclei, and the Coulombic interaction of the electrons and nuclei. Note that the kinetic terms and the attractive Coulombic potentials are all negative, whilst the repulsive terms are positive. Hence, while the kinetic and attractive terms act to stabilise the system, the repulsive terms will destabilise it. Equation 2.3 can be further simplified by taking into account the Born-Oppenheimer (B-O) approximation[9], that is, the nuclei are stationary whilst the

electrons move around them. The effect of the B-O approximation is that the kinetic energy of the nuclei is reduced to zero and the nucleus-nucleus interaction can be treated separately. Hence the last term in Equation 2.3 is a constant given the positions of all nuclei *k* and *l*, and no longer needs to be calculated with the wave function, and correlation is eliminated in the third expression. The effect of this is to split Schrödinger's equation into two parts, an electronic part and an ionic part, where the nuclei will not respond to the electron motion. A problem still remains in that the fourth term is impossible to solve exactly. The two electrons, *i* and *j*, are intimately related and as electron *i* moves the potential observed for electron *j* changes, to which its response cannot be instantaneous. Since the repulsion between two electrons is a considerable energy (1389 kJ mol^{-1} when separated by 1 Å) it cannot simply be ignored.

Hartree suggested that instead of ignoring the electron-electron repulsion, the correlation between the electrons could be ignored[10]. In this approach, which is known as the self consistent field (SCF), an electron experiences the potential of the average field generated by the other electrons present. If we start with the simple singular electron Hamiltonian (Equation 2.4)

$$h_i = -\frac{\nabla^2_i}{2} - \sum_{k=1}^{M} \frac{Z_k}{r_{ik}} \qquad \textbf{Equation 2.4}$$

In this expression the nuclei-nuclei interaction term has been removed. A complete all-electron Hamiltonian can be made up from the sum of all the single-electron Hamiltonians (Equation 2.5).

$$\hat{H} = \sum_{i=1}^{N} h_i$$ **Equation 2.5**

In this solution all electron-electron interactions are ignored, and as previously stated this is a significant contribution to the energy. This procedure offers the tremendous advantage of being able to solve the Schrödinger equation one electron at a time. By adding a potential that is generated by the other electrons to Equation 2.4, an averaged electron-electron repulsion is included (see Equation 2.6). In this way only the correlation between electrons is omitted.

$$h_i = -\frac{\nabla_i^2}{2} - \sum_{k=1}^{M} \frac{Z_k}{r_{ik}} + V_i\{j\}$$

Equation 2.6 The electronic Hamiltonian operator expressed for electron *i*. $V_i\{j\}$ is the potential electron i experiences, generated by the other electrons present.

The SCF approach is not the full story, as a minimum-energy wavefunction is still required. Hartree suggested a method which entailed guessing an initial wavefunction and solving a set of single-electron Hamiltonians to produce a new set of wavefunctions. The quality of each set of wavefunctions can be graded; the better the wave function the lower the energy it will produce. Still this method is flawed, in that it does not account for the indistinguishable nature of electrons, nor does it account for the Pauli exclusion principle[11]. This principle is a special case of the Pauli principle which states: when the labels of any two identical fermions are exchanged, the total wavefunction changes phase (positive becomes negative and

vice versa). This implies that in a triplet state $^3\Psi$ can be expressed as shown in Equation 2.7

$$^3\Psi = \Psi_a(\alpha_a)\,\Psi_b(\alpha_b) = -\,\Psi_a(\alpha_b)\,\Psi_b(\alpha_a)$$

Equation 2.7. The product of a wavefunction 'a' acting on fermion 'a' with the wavefunction of 'b' acting on fermion 'b' is equivalent to negative the product of wavefunction 'a' acting on fermion 'b' with the wavefunction of 'b' acting on fermion 'a'.

In Hartree's SCF approach this is clearly not the case, furthermore there is no mechanism by which a change can occur. The changing of electron spin in this manner is known as exchange, a solution to which was first proposed by Fock[12]. Fock proposed that Slater determinants (Equation 2.8) could be used as a mechanism to allow exchange within the Hartree formulism.

$$\Psi_{\text{slater determinant}} = \frac{1}{\sqrt{n!}} \begin{pmatrix} \Psi_1(\alpha_1) & \Psi_2(\alpha_1) & \bullet\bullet\bullet & \Psi_n(\alpha_1) \\ \Psi_1(\alpha_2) & \Psi_2(\alpha_2) & \bullet\bullet\bullet & \Psi_n(\alpha_2) \\ \bullet & \bullet & \bullet & \bullet \\ \bullet & \bullet & \bullet & \bullet \\ \bullet & \bullet & \bullet & \bullet \\ \Psi_1(\alpha_n) & \Psi_2(\alpha_n) & \bullet\bullet\bullet & \Psi_n(\alpha_n) \end{pmatrix}$$

Equation 2.8. The general expression for a Slater determinant, where *n* is the number of fermions.

Referring to each wavefunction on each line accounts for the fact that electrons are indistinguishable from each other and mechanical exchange can occur: swapping any two lines changes the sign of the determinant. This can be illustrated with a two-electron example,

$$^3\Psi_{\text{slater determinant}} = \frac{1}{\sqrt{2}}\begin{pmatrix} \Psi_a(\alpha_a)\ \Psi_b(\alpha_a) \\ \Psi_a(\alpha_b)\ \Psi_b(\alpha_b) \end{pmatrix}$$

generated the determinant $^3\Psi_{SD} = \frac{\Psi_a(\alpha_a)\Psi_b(\alpha_b) - \Psi_a(\alpha_b)\Psi_b(\alpha_a)}{\sqrt{2}}$

and of course should the exchange occur any two lines in the matrix are swapped, leading to

$$^3\Psi_{\text{slater determinant}} = \frac{1}{\sqrt{2}}\begin{pmatrix} \Psi_a(\alpha_b)\ \Psi_b(\alpha_b) \\ \Psi_a(\alpha_a)\ \Psi_b(\alpha_a) \end{pmatrix}$$

generating the determinant $^3\Psi_{SD} = \frac{\Psi_a(\alpha_b)\Psi_b(\alpha_a) - \Psi_a(\alpha_a)\Psi_b(\alpha_b)}{\sqrt{2}}$

Including Slater determinants to solve the repulsion between two electrons results in the following:

$$\int {}^3\Psi_{SD} \frac{1}{r_{12}} \, {}^3\Psi_{SD} \, dr_1 \, d\omega_1 \, dr_2 \, d\omega_2$$

$$= \int \frac{\Psi_a(\alpha_a)\Psi_b(\alpha_b)-\Psi_a(\alpha_b)\Psi_b(\alpha_a)}{\sqrt{2}} \frac{1}{r_{12}} \frac{\Psi_a(\alpha_a)\Psi_b(\alpha_b)-\Psi_a(\alpha_b)\Psi_b(\alpha_a)}{\sqrt{2}} \, dr_1 \, d\omega_1 \, dr_2 \, d\omega_2$$

$$= \int \left(\frac{\Psi_a{}^2(\alpha_a)^2}{\sqrt{2}} \frac{\Psi_b{}^2(\alpha_b)^2}{\sqrt{2}} \frac{1}{r_{12}} \right) dr_1 \, d\omega_1 \, dr_2 \, d\omega_2$$

$$-2 \int \left(\frac{\Psi_a \, \Psi_{\mathbf{b}} \, (\alpha_a)^2}{\sqrt{2}} \frac{\Psi_a \, \Psi_{\mathbf{b}} \, (\alpha_b)^2}{\sqrt{2}} \frac{1}{r_{12}} \right) dr_1 \, d\omega_1 \, dr_2 \, d\omega_2$$

$$+ \int \left(\frac{\Psi_b{}^2(\alpha_b)^2}{\sqrt{2}} \frac{\Psi_a{}^2(\alpha_a)^2}{\sqrt{2}} \frac{1}{r_{12}} \right) dr_1 \, d\omega_1 \, dr_2 \, d\omega_2$$

which simplifies to

$$= \frac{1}{2} \int \left(\Psi_a{}^2(\alpha_a)^2 \, \Psi_b{}^2(\alpha_b)^2 \frac{1}{r_{12}} \right) dr_1 \, d\omega_1 \, dr_2 \, d\omega_2$$

$$- \int \left(\Psi_a \, \Psi_{\mathbf{b}} \, (\alpha_a)^2 \, \Psi_a \, \Psi_{\mathbf{b}} \, (\alpha_b)^2 \frac{1}{r_{12}} \right) dr_1 \, d\omega_1 \, dr_2 \, d\omega_2$$

$$+ \frac{1}{2} \int \left(\Psi_b{}^2(\alpha_b)^2 \, \Psi_a{}^2(\alpha_a)^2 \frac{1}{r_{12}} \right) dr_1 \, d\omega_1 \, dr_2 \, d\omega_2$$

As the first and last terms are identical this can be referred to with two terms: (i) an electron repulsion term (the positive/destabilising terms) and (ii) an electron exchange term (the negative/stabilising term). If this solution is applied to a singlet

state the exchange term is zero due to the orthogonal nature of the electrons, i.e. the exchange term is $-\int\left(\Psi_a\,\Psi_{\mathbf{b}}\,(\alpha_a\,\beta_a)\,\Psi_a\,\Psi_{\mathbf{b}}\,(\alpha_b\,\beta_a)\,\frac{1}{r_{12}}\right)dr_1\,d\omega_1\,dr_2\,d\omega_2$, the $\alpha_a\,\beta_a$ term is zero reducing the full exchange to zero, leaving just the repulsion term.

One pressing question still remains, namely what function will best represent the wavefunction? The most obvious function is to use one which will closely match the electronic orbitals. Slater type orbitals (STO)[13] fit experimental electron orbitals to numerical wave functions, and have the form of Equation 2.9.

$$\Psi_{STO} = \left(\frac{\zeta^3}{\pi}\right)^{\frac{1}{2}} e^{(-\zeta r)}$$

Equation 2.9 A Slater type orbital. The pre-exponential factor, represents the weighting of the function, *r* is the radius and ζ is the orbital exponent.

Slater functions closely fit the molecular orbitals, but they are complicated to manipulate mathematically and cannot be integrated analytically, which in turn leads to long computation time.

Another method, developed by Boyes[14], uses a combination of Gaussian type orbitals (GTOs), which take the form of Equation 2.10.

$$\Psi_{GTO} = \left(\frac{2\alpha}{\pi}\right)^{\frac{3}{4}} e^{(-\zeta r^2)}$$

Equation 2.10 A Gaussian type orbital. Note the post exponential factor is now a function of r^2.

The advantage of using Gaussian functions is that mathematical manipulation is simpler (e.g. multiplication of two Gaussian functions results in another Gaussian). This results in rapid simulations but with a loss of accuracy, since Gaussian functions do not provide as accurate a fit against experimental wavefunctions as their Slater counterparts. However, a combination of GTOs may be used to generate a function closely fitting to the STO[15] and still produce rapid simulations (Figure 2.6).

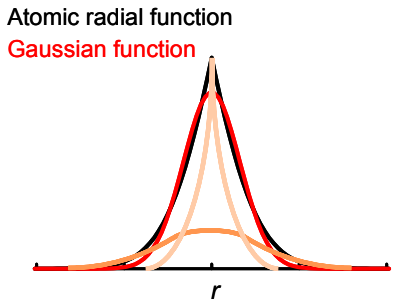

Figure 2.6 Graphical representation of a linear combination of Gaussian functions to approximate a more realistic atomic radial function.

Gaussian basis sets are not without problems; by their very nature they are incomplete. Increasing the number of basis functions used can minimise this, but increasing the basis set increases the time of calculation and this can become prohibitively expensive. The incompleteness of a basis set can lead to further problems in the basis set superposition error (BSSE). This occurs when a neighbouring atom's basis set overlaps and is allowed to optimise and account for some of the neighbouring atom's electrons. In most cases the small change in energy due to the BSSE is inconsequential, but when calculating the binding energy of a model (for example two molecules) the BSSE can increase the binding by up to 40%. To compensate for the BSSE, Boyes and Bernard[16] suggested that to calculate the

binding strength, instead of removing all trace of the atom, just the core and electrons are removed. This leaves the basis set in place to account for the same energy it did previously. Using the counterpoise correction accounts for the overestimation of binding energy, but the new calculated binding energy is now too low. This underestimation of binding energy is due to the initial dimer relaxation, the BSSE allows the two molecules to approach closer that they would in an infinite basis set, thus the binding energy will be smaller in this fictional model than it would in reality.

2.3.2 Pseudopotentials

The computational cost of the basis set can be further reduced by use of pseudopotentials. Pseudopotentials are used to represent the core for large atoms, for example iodine, ($1s^2$, $2s^2$, $2p^6$, $3s^2$, $3p^6$, $3d^{10}$, $4s^2$, $4p^6$, $4d^{10}$, $5s^2$, $5p^5$), the majority of whose electrons will take no part in the reactivity, with only the $5s^2$ and $5p^5$ valence electrons worth considering. The other electrons act to shield the valence electrons from the core. These electrons may not need full quantum mechanical treatment and can be simplified. The core may be replaced with a potential to approximate the nucleus and core electrons, allowing the basis sets to focus on the more important valence electrons.

2.3.3 Plane wave basis sets

Gaussian basis sets lend themselves well to gas-phase calculations as they are easy to model and easy to isolate. In condensed phases the BSSE can become considerable and to circumvent this, a different approach to designing a basis set, based on plane waves, can be used. The electronic structure of a crystal can be simplified with Brillouin's theory, using the Brillouin zone to represent the electronic structure. Any electron outside this region is equivalent to some electron inside it. Plane waves can be used[17], expressed to a maximum limit, to represent the electrons within the Brillouin zone. Using this interpretation even empty space has a basis set associated with it, removing the BSSE. Plane waves have the further added advantage of allowing efficient force calculation and using fast Fourier transforms (FFT) to calculate kinetic energy / potential energy easily.

The main disadvantages of plane waves are that a large number of plane waves are required to represent the orbitals. Furthermore, close to atomic centres the wavefunctions required to model core electron repulsions are prohibitively high. The second issue is easiest to remedy with pseudopotentials, discussed in the previous section. In this case pseudopotentials smooth the core potential while no change is made to the valence potential, allowing the basis-set energy cutoff to be expressed to a lower level (Figure 2.7)[18].

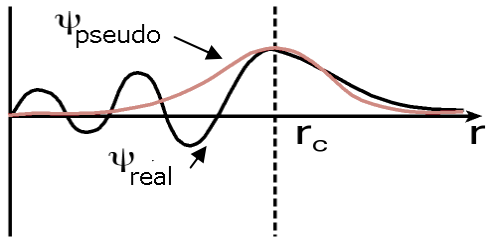

Figure 2.7 A pseudopotential used to represent the high-frequency cone, decreasing the need to use high-frequency plane waves.

Since plane waves require periodic boundary conditions they are used to simulate condensed phases. The large number of plane-wave basis functions required implies a level of theory which uses linear scaling (or close to linear scaling) with respect to number of basis functions is required. One such method is Density Functional Theory (DFT), which is discussed below.

2.3.4 Electron correlation

Hartree's method with Fock's Slater determinant (Hartree Fock or HF) is a powerful entry-level calculation, and still widely used today. However, there is one major limitation with it: the absence of an electron correlation term. The net effect of this is to allow electrons too close to one another, and to ignore how the motion of one electron directly effects another. It is therefore an insufficient model for induced dipole - induced dipole (or Van der Waals) interactions. Hartree Fock theory still finds uses in modern simulations for systems where correlation is only a small part of the energy (ca. 1%). Electron correlation can be included as an extension to HF theory, using methods such as the Møller Plesset pertubation theory (e.g. MP2 etc)[19], Configuration Interaction (CI) and Coupled Cluster (CC) theory. However, these theories require considerable computational expense.

In 1964 Hohenberg and Kohn wrote a pivotal paper[20] reporting how energy can be calculated directly from the electron density, by a method known as density functional theory (DFT). A later paper by Kohn and Sham[21] showed how DFT may be approached in a similar manner to HF, self consistently. Whilst Hohenberg and Kohn successfully demonstrated that the principle of DFT was exact, one major hurdle remains to this day: the functional which maps the electron density onto energy is not known.

DFT was developed from Thomas-Fermi theory,[22,23] and is a quantum mechanical approach to the many-body problem. The Thomas-Fermi theory begins by assuming the system consists of N independent, homogeneous electrons interacting with an external potential (ω). Rehashing Schrödinger's equation the total energy can be made to relate to three terms:

$$E = \Psi\hat{H}\Psi = T + U + W$$

Equation 2.11 Schrödinger's equation, where T describes the kinetic energy of the system, U describes the electron-electron repulsion and W describes the interaction between the electrons and an external field.

Equation 2.11 can be further extended by expanding the terms *T*, *U* and *W*

$$T = \frac{1}{2} \int \hat{H}\Psi^{*}(r)\, \hat{H}\Psi(r)\, dr$$

$$W = \int \rho(\mathbf{r})\, \omega(\mathbf{r})\, dr$$

$$U = \frac{1}{2} \int\int \rho(\mathbf{r})\, \rho(\mathbf{r'})\, v(\mathbf{r}-\mathbf{r'})\, g(\mathbf{r}, \mathbf{r'})\, d^3r\ d^3r$$

*where ρ is the electron density, v is the interaction potential for electron-electron repulsion and g(**r, r'**) is the pair-correlated function*

The pair correlation function has a simple purpose, to give the probability of finding an electron at position **r'** given the presence of an electron at **r**. The effect of this function can be clearly seen: as g(**r**, **r'**) tends to 1, |**r** – **r'**| tends to ∞.

The term where g = 1 is equivalent to the pure Hartree equation, which ignores exchange and correlation. This observation inspired the splitting of the g term to g = 1 + (g - 1) allowing the U term to be further expanded (Equation 2.12).

$$U = \frac{1}{2} \int\int \rho(\mathbf{r})\, \rho(\mathbf{r'})\, v(\mathbf{r} - \mathbf{r'})\ d^3r\ d^3r + \frac{1}{2} \int\int \rho(\mathbf{r})\, \rho(\mathbf{r'})\, v(\mathbf{r} - \mathbf{r'})\, (g(\mathbf{r}, \mathbf{r'}) - 1)\, d^3r\ d^3r$$

Equation 2.12 The electron-electron repulsion. The first term describes the Hartree-only energy (no correlation or exchange) and the second term accounts for both exchange and correlation as a fraction of the Hartree energy.

Hartree-Fock theory scales as 3*N* special variables and 1*N* spin variables, and post H-F theories which include electron correlation scale even less favourably. DFT bypasses the old problem of electron-electron interactions by relating energy to electron density and since electron density is dependent on just 3 spatial variables, scaling factors are minimized. DFT is split into three categories:

1. Local Density Approximation (LDA) – Early DFT was applied to constant, slowly varying density ($\rho(\mathbf{r})$), which is a fair assumption when applied to metals, conductors and semiconductors. However, for molecular systems where electron density varies wildly the approximation is no longer valid. LDA operates by applying a grid to the system; each component of the grid is assigned a single electron density. A functional is then applied to map the density to energy, based on equations derived from a model of the free-electron gas.

2. Generalised Gradient Approximation (GGA) – GGA is a post LDA method where extensions were made to account for the curvature of the electron density better. GGA operates by applying the same grid as the LDA but with each component a density and a gradient is associated, both of which are used to calculate energy. This is the commonly used DFT method for molecular systems and has found many uses in chemistry. As previously mentioned the strengths of DFT are the favourable scaling and that it also has some hold on electron correlation (a good local correlation but with no long range correlation). DFT estimates both exchange and correlation whereas the HF method calculates exchange exactly but ignores electron correlation. Hybrid DFT, the next extension, uses DFT to calculate most of the energy, but uses HF for calculating an exact exchange.

3. Hybrid DFT - These functionals take the best of both worlds, using small amounts of HF, LDA and GGA. Commonly used functionals are Becke's three parameters (B3)[24], in which Becke parameterised the amount of HF, LDA and GGA in accordance to a set of training compounds. The resulting functional translates remarkably well across many systems. However, since they were derived by fitting to a training set of compounds, if you stray from this then you should anticipate the functionals to work less well. The hybrid functionals based on Becke's parameter set have found enormous success, and due to their favourable scaling, in many cases have replaced the more intensive Møller Plesset calculations.

2.3.5 Representing more complex systems

The majority of the techniques discussed previously pertain to gas-phase simulations. Solid-phase simulations need special treatment as a periodic boundary condition is needed. As discussed earlier plane waves lend themselves particularly well to periodic models and since a large number of plane waves are required, DFT is the theory of choice. A couple of problems still remain, namely summing the Coulomb potential to infinity and representing a system of infinite electrons. To combat the of a slowly converging Coulomb sum, Ewald's summation can be used used. The Ewald sum is a relatively simple mathematical manipulation. By separating the summation into two parts, short-range and long-range, its convergence can be accelerated.

The problem of representing the electrons is more complex. As mentioned previously the Brillouin zone can be used to represent the electronic structure, but how to sample the Brillouin remains a concern. In practice the Brillouin zone is sampled at

specific points or K-points. Each K-point represents one point on the electronic band of the material, should the material have a complex band structure many k-points are required. Molecular materials often have a simple band structure and so minimal K-point sampling is required.

Chemists now have at their disposal a computational model to describe condensed matter based on first principles. This is a relatively recent achievement, due to the advances in software and hardware that were necessary to be able to deal with the complexities of real solid-state problems. Computation is now ideally placed to answer many of the intriguing questions that experimental models pose.

References

[1] C. Jönsson, *Z. Phys.,* **161,** 454 (1965).

[2] C. Hammond, The Basics of Crystallography and Diffraction, second ed. Oxford University Press.

[3] H. J. Milledge, Department of Geology, University College, London.

[4] V. F. Sears, *Neutron News*, **3**, 26 (1992).

[5] J. M. Besson, R. J. Nelmes, G. Hamel, J. S. Loveday, G. Weill, S. Hull. *Physica B,* **180-181**, 907 (1992).

[6] L. Merrill and W. A. Bassett, *Rev. Sci. Instrum.,* **45,** 290 (1974).

[7] W. C. Marshall and D. J. Francis, *J. Appl. Cryst.,* **35**, 122 (2002).

[8] G. J. Piermarini, S. Block, J. D. Barnett and R. A. Forman, *J. Appl. Phys.,* **46**, 2774 (1975).

[9] M. Born and R. Oppenheimer, *Annalen der Physik*, 389, 457 (1927).

[10] D. R. Hartree, Proc. R. Soc. London, **113**, 621 (1928).

[11] P. W. Atkins, Physical Chemistry, sixth ed., Oxford University Press.

[12] V. Fock, *Z. Phys*. **61**, 126 (1930)

[13] J. C. Slater, *Phys. Rev.*, **36**, 57 (1930).

[14] J. M. Foster and S. F. Boys, *Rev. Mod. Phys.,* **32**, 303 (1960).

[15] W. J. Hehre, R. F. Stewart, and J. A. Pople, *J. Chem. Phys*., **51,** 2657 (1969).

[16] S. F. Boys, F. Bernardi, *Mol. Phys.,* **19**, 553 (1970).

[17] R. Carr and M. Parinello, *Phys. Rev. Lett.,* **55**, 2471 (1985).

[18] D. Vanderbilt, *Phys. Rev. B*, **41,** 7892 (1990)

[19] C. Møller and M. S. Plesset, *Phys. Rev.*, **46**, 618 (1934).

[20] P. Hohenberg and W. Kohn, *Phys. Rev*. B, **136**, 864 (1964).

[21] W. Kohn and L. J. Sham. *Phys. Rev. A*, **140**, 1133 (1965).

[22] L. H. Thomas, *Proc. Cambridge Philos. Soc*., **23**, 542 (1927).

[23] E. Fermi, *Z. Phys*., **48**, 73 (1927).

[24] A. D. Becke, *J. Chem. Phys*., **98**, 5648 (1993).

Chapter 3

Sodium Formate Dihydrate

3.1 Introduction

Sodium formate (HCOONa) finds uses across many industries and is also of environmental importance (e.g. aqueous solutions are used to absorb SO_2 in thermoelectric power plants). The most notable industrial applications are as additives in drilling fluids for the oilfields. Solutions of sodium formate with water-soluble polymers are used to prevent plugging or build-up of damaging metal carbonates, bicarbonates or sulfates. Knowledge of the high-pressure behaviour of sodium formate hydrates is therefore highly desirable. To date only anhydrous sodium formate has been studied at high-pressure,[1] and little work on the hydrated species has been reported. In this work we focus on the dihydrate of sodium formate, and report a new structural phase obtained at 17 kbar.

Structures obtained from high-pressure X-ray crystallographic measurements are often incomplete as the Merrill-Basset diamond anvil cell[2] necessarily limits the diffraction dataset that can collected. Although this poses no problem for good scattering (heavy) atoms, poor scattering (i.e. hydrogen) atoms are often impossible to locate. This shortcoming is particularly serious for molecular systems, where hydrogen bonding is the dominant intermolecular interaction. At this point there are two methods available to assist completion of the structure: computational modelling or high pressure neutron diffraction. In this study we were fortunate to be able to do both. The computational study was completed prior to obtaining neutron diffraction data, which thereby served to validate the computational result.

In our computational work we take the partially complete experimental structure (i.e. the unit cell parameters and heavy-atom positions have been refined) and use quantum mechanical modelling (plane-wave density functional theory, PW-DFT) and molecular dynamics (MD) calculations to locate the missing hydrogen atoms.[3] Although force fields do exist that would be capable of handling our system (such as that put forward by Nardelli[4], that can describe the interactions between water hydrogen atoms and oxygen atoms bound to molecules), these have been parameterised for ambient pressure conditions. For that reason, the use of a quantum mechanical model is essential.

In this chapter we report on the new high-pressure phase obtained for sodium formate dihydrate at 17 kbar, with the hydrogen atoms found computationally. The

complete structure subsequently obtained by high-pressure neutron diffraction is then presented, and found to be in agreement with our X-ray and computational studies. We also report a computational study on the ambient pressure polymorph, which was used as an initial benchmark to assess the accuracy of the PW-DFT simulation method.

3.2 Experimental and Computation Methodology

3.2.1 High Pressure X-Ray Diffraction

The crystals were grown by loading and pressurising a saturated aqueous solution of sodium formate in a Merrill-Bassett diamond-anvil cell[2] equipped with 600 μm culet diamonds and a tungsten gasket. The gasket had been pre-indented to a thickness of 100 μm and had a 200 μm hole drilled through it. After the nucleation of several crystallites, the temperature was cycled close to the point at which the crystals redissolved so that the number of crystallites could be progressively reduced. Finally, a single crystal was obtained at a pressure of 17 kbar.

Diffraction data were collected at room temperature on a Bruker Smart APEX diffractometer[5] with graphite-monochromated MoKα radiation (λ = 0.71073 Å). High-pressure data collection and processing procedures were as described by Dawson et al.[6] Absorption corrections for the intensity data were applied in two stages with the programs SHADE[7] and SADABS[8].

The final structural model was solved and refined using the CRYSTALS suite of programs[9]. All non-hydrogen atoms were refined using isotropic atomic displacement parameters. The formate hydrogen atom was placed geometrically, while the hydrogen atoms associated with the water molecules were placed on idealised positions, at a distance of 0.9 Å from their parent oxygen atoms, along the direction of likely hydrogen bonds. The hydrogen atom positions were allowed to vary during the subsequent refinements using a riding constraint. The structural parameters to the final fit, along with the refinement statistics, are listed in Tables 3.1 and 3.2.

Pressure / GPa	
Crystal system	Monoclinic
Space Group	$P2_1$
a (Å)	7.6852(9)
b (Å)	3.5113(3)
c (Å)	8.1103(17)
β (˚)	111.780(14)
Volume (Å^3)	202.23(6)
$2\theta_{max}$ (°)	22.455
Z	2
Reflections collected	369
No. Unique [Rmerge]	109 [0.035]
No. $F>3\sigma(F)$	104
Parameters	25
R1 [$F>3\sigma(F)$]	0.0827
wR2 (F, all data)	0.0918
S	1.1988
$\Delta\rho_{max}$ (e Å^{-3})	0.31
$\Delta\rho_{min}$ (e Å^{-3})	-0.24

Table 3.1 Experimental parameters for the high-pressure phase of sodium formate dihydrate.

3.2.2 Computational methods

Equilibrium structures for the sodium formate dihydrate series (i.e. the ambient and high pressure phases, labelled phase I and phase II, respectively) were obtained using the VASP 4.4 simulation package[10] according to the following procedure. Initial geometries and space-group symmetry constraints were taken from experiment. In the case of unlocatable hydrogen atoms, intuitive positions were selected based on a close inspection of the heavy atom positions and assuming, but not constraining to, a C_{2v} structure for the H_2O molecule. A set of atomic position optimisations were performed initially such that a reasonable hydrogen bonding network would be in

place before any volume change was permitted. This was then followed by a series of single-point energy calculations where the lattice constants (multipliers for the cell vectors) were varied over a range from -7% to +7% of the experimental cell in increments of 0.5%, thus establishing the volumes of the unit cells that gave rise to the lowest energies. All subsequent optimisations were then held at these fixed volumes. The atomic positions and lattice parameters were then optimised on alternate cycles until convergence was achieved. Simulations were performed using a set of ultrasoft pseudopotentials[11] and plane waves expressed at an energy cut-off at 396 eV. The generalised gradient approximation (GGA) functional PW91[12] was used to model the exchange and correlation potentials, and the Brillouin zone sampled by one k-point at the gamma (Γ) position. Convergence criteria were set such that optimisation was achieved once forces reached less than 10^{-3} eV $Å^{-1}$ and SCF energy less than 10^{-4} eV. A series of single point energy calculations showed that PW energy cut-off and K-point sampling was sufficient.

The equilibrium structure work was then followed by a series of PW-DFT microcanonical (constant number of atoms, volume and energy) molecular dynamics calculations performed in P1 symmetry, in order to search the potential energy surface more completely, and to investigate the effects of temperature (i.e. free energy) on the resulting thermally-averaged structures. This also offered the opportunity to extract vibrational frequencies from the simulation by Fourier transformation of the autocorrelation function of the calculated forces, with low-frequency noise subtracted from the resulting spectra using a Blackman windowing function[13]. The basis set cut-off was lowered to 297 eV, and identical convergence criteria and k-point sampling as for the equilibrium calculations were used. With the equilibrium structures used as starting points, MD simulations were run using a time step of 0.6 fs, determined following careful consideration of the highest energy vibrational frequency for the system (the O-H stretch). Confirmation of the appropriateness of this time-step was obtained by careful analysis of the resulting conservation of free energy in the NVE ensemble. The first 0.12 ps of each simulation was discarded to allow the system to reach equilibrium; data were then collected over a further 0.84 ps. Averaged equilibrium temperatures obtained for the two phases were 217(16) and 220(20) K, respectively.

It is worth noting that our modelling approach is not without its flaws. As we have held the volume at a constant value (as obtained in the equilibrium calculation) throughout all our MD calculations, we have effectively increased the pressure since thermal expansion will cause an increase in volume that has not been accounted for. In addition, our calculations have at their heart density functional theory, with all the standard limitations that this method entails (e.g. the dispersion forces are not modelled). Nevertheless, our simulations have successfully reproduced the key features of the crystal structure geometries and experimental vibrational spectra within acceptable levels of accuracy.

3.2.3 Neutron diffraction

Time-of-flight (tof) neutron powder diffraction data at high pressure were collected using the PEARL beamline high-flux medium-resolution ($\delta d/d$ = 0.85%) diffractometer (HiPr) located at the ISIS Facility of the Rutherford Appleton Laboratory, Chilton, UK [14,15]. This experiment used a type V3b Paris-Edinburgh cell[16,17] equipped with standard WC/Ni-binder toroidal anvils and TiZr capsule gaskets (55 mm^3 initial volume)[18]. The tof diffraction patterns shown in the figure 3.1 were obtained after electronic focussing of the 1080-detector element spectra of the nine modules of the main $2\theta=90^o$ bank, normalisation of the summed pattern with respect to the incident beam monitor and the scattering from a standard vanadium sample and correction for the wavelength and scattering-angle dependence of the neutron attenuation by the anvil (WC) and gasket (TiZr) materials[19]. Full-profile Rietveld refinements of the resulting patterns were carried out using PC-GSAS[20] as implemented in the EXPGUI package[21].

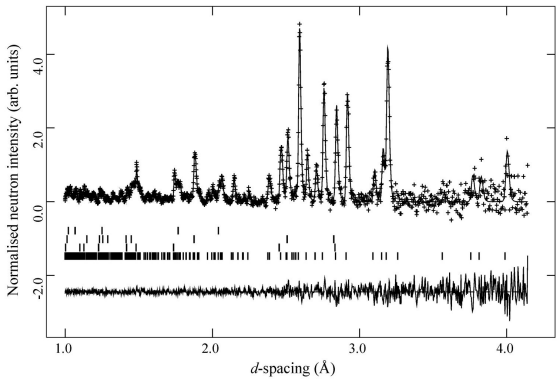

Figure 3.1 Neutron powder diffraction pattern at 11 tonnes loading.

Perdeuterated sodium formate dihydrate ($DCOONa.2D_2O$) was loaded into a standard capsule gasket in the form of a thick slurry (to prevent dehydration) along with a ~1 mm diameter lead pellet, the latter being present to provide a suitable pressure marker[22]. Prior to loading and sealing the capsule within the Paris-Edinburgh press a small quantity of perdeuterated isopropyl alcohol pressure medium was injected into the sample using a fine hypodermic syringe. Once loaded into the Paris-Edinburgh press, the sample was sealed within the capsule using an initial applied load of 6.5 tonnes. The applied load and, hence, the sample pressure, was varied and monitored by means of a computer-controlled hydraulic oil pressure system connected to the in situ hydraulic ram of the press.

In the time available for this experiment, neutron powder diffraction data were collected at 15 pressure points at cell loads between 6.5 tonnes and 40 tonnes, with data collection times ranging between 2 and 5 hours. Somewhat unexpectedly, the high-pressure $P2_1$ phase pattern of sodium formate dihydrate was observed at the initial load setting, at which the pressure was calculated to be 0.08(5) GPa. Basically the same diffraction pattern was observed up to the maximum pressure of 4.30(5) GPa in spite of the appearance of extra peaks in the pattern corresponding to the D_2O ice VI – first seen at 17 tonnes load – which subsequently transformed into ice VI at 32 tonnes load. The refined unit cell parameters and atomic coordinates shown in the tables 3.2 and 3.3 are those resulting from the profile Rietveld refinement of the 11 tonnes load pattern which corresponded to a pressure of 0.87(5) GPa. Note that, as $P2_1$ is a polar spacegroup with an arbitrary origin in *y*, the atomic coodinates were refined with *y*(Na) held constant at the value obtained from the X-ray study.

3.3 Results and discussion

3.3.1 Phase I- ambient pressure

Ambient pressure structural studies[23] of sodium formate dihydrate reveal a Cmca orthorhombic lattice with cell vectors a=7.070 Å, b=14.534 Å, c=8.706 Å, containing eight $NaHCO_2.2H_2O$ units. The sodium ion is arranged within an octahedral field, coordinated to two adjacent formate ions, with H_2O molecules filling the four remaining positions. Each ligand is bidentate, bridging between

adjacent sodium ions. In this manner a 2D sheet of sodium ions can be built. A network of hydrogen bonds extends in a parallel sheet holding adjacent sodium sheets in place (see Figure 3.2). Solid-state DFT calculations would be expected to perform well for this system: the structure contains only sodium and first-row elements and there is a discernable interaction in every direction (hydrogen bond or electrostatic), hence dispersion forces (which current DFT functionals fail to model) will be responsible for very little of the structural features. Our computational investigation began with this structure in order to verify that PW-DFT calculations can successfully model the key features of the cell, before turning to the high-pressure phase.

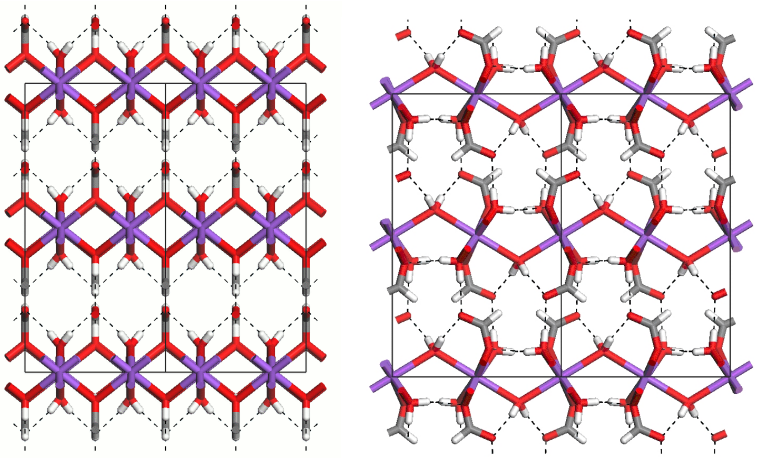

Figure 3.2 Phase I structure of sodium formate dihydrate, viewed along the *z* (left) and the *x* (right) axes.

	Phase I - ambient pressure		Phase II - high pressure		
	Experiment	Calculated	X-ray	Calculated[a]	Neutron
a (Å)	7.070 (4)	7.154	7.6852(9)	7.6419	7.6914(9)
b (Å)	14.534 (2)	14.479	3.5113(3)	7.1992	3.5187(3)
c (Å)	8.706 (2)	8.636	8.1103(17)	8.0583	8.1102(9)
α=γ (°)	90	90	90	90	90
B (°)	90	90	111.78(14)	111.46	111.81(1)
Volume (Å^3)	894.6 (1)	894.6	202.23(6)	412.6	203.79(2)

Table 3.2 Unit cell data for the two phases of sodium formate dihydrate.

[a] '*b*' vector doubled in simulation cell, see text.

	X-ray[a]			Calculated[b]			Neutron		
	x	*y*	*z*	*x*	*y*	*z*	*x*	*y*	*z*
Na	0.1830(16)	0.296(3)	0.642(3)	0.1914(3)	0.3120(6)	0.6578(4)	0.185(4)	0.296(10)	0.657(3)
C	0.081(3)	0.317(6)	0.211(5)	0.1053(5)	0.3182(3)	0.2296(3)	0.093(2)	0.288(10)	0.226(2)
O	0.0140(3)	0.291(4)	0.330(4)	0.0210(5)	0.3212(14)	0.3376(5)	0.017(2)	0.327(11)	0.337(2)
O	0.241(3)	0.114(5)	0.246(6)	0.2558(11)	0.1402(4)	0.2477(10)	0.246(2)	0.134(9)	0.245(2)
H	0.028	0.501	0.107	0.0436(6)	0.4840(3)	0.1054(2)	0.025(3)	0.446(10)	0.102(2)
O	0.336(3)	0.318(5)	0.949(5)	0.3629(11)	0.3072(5)	0.9659(5)	0.352(3)	0.347(10)	0.962(3)
H	0.433	0.481	-0.026	0.4573(8)	0.5136(2)	0.0049(6)	0.422(3)	0.576(10)	0.000(3)
H	0.302	0.238	0.037	0.3218(<1)	0.2484(<1)	0.0671(1)	0.303(3)	0.260(11)	0.0473(3)
O	0.376(3)	0.823(4)	0.605(5)	0.3646(<1)	0.8098(22)	0.5896(1)	0.362(3)	0.784(11)	0.589(2)
H	0.499	0.764	0.657	0.5023(2)	0.7744(50)	0.6385(3)	0.494(3)	0.768(11)	0.638(2)
H	0.337	0.922	0.495	0.3309(3)	0.8986(11)	0.4650(2)	0.341(3)	0.908(9)	0.480(3)

Table 3.3 Fractional coordinates of the asymmetric unit.

[a] hydrogen atom placed 0.9 Å from O atoms with O-H-O angle 180°

[b] standard deviations obtained for calculated positions by superimposing all asymmetric units.

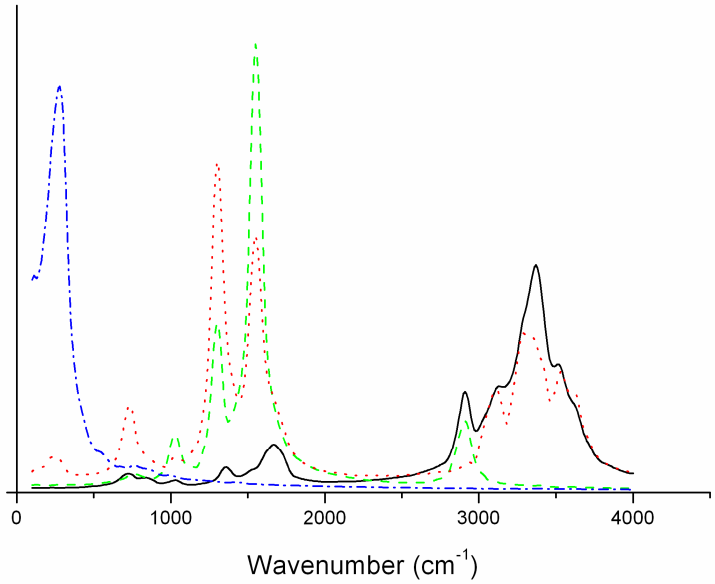

Figure 3.3 Calculated ambient pressure vibrational spectra. Solid line = hydrogen vibration, dashed line = carbon vibration, dotted line = oxygen vibrations and dot dashed line = sodium vibrations.‡

Initial optimisations changed very little from the experimental structure with no overall change in volume and only minimal changes in cell shape (see Table 3.2). Visual superposition of the two structures confirmed that the calculated minimum energy structure corresponded with that obtained from experiment. Comparing experimental distances with those calculated shows minimal differences. Na-O distances differed by a maximum of 0.025 Å, whilst the maximum bonded distance differed by at most 0.157 Å (in the case of hydrogen) and 0.049 Å (in the case of heavy atoms), well within computational boundaries.

In order to explore the potential energy surface (PES) further, a molecular dynamics (MD) calculation was undertaken. This allowed direct visualisation of the flexibility of the system and local wells to be accessed if the system has enough thermal energy to overcome any potential-energy barriers. Visualisation of the MD simulation showed that, despite the lack of symmetry constraints, the Cmca space group was essentially retained in this calculation. Furthermore, the main geometrical features were maintained, indicating a lack of close energy minima. Following the MD calculation, the forces were extracted from each step, subjected to an autocorrelation function and the resulting plots Fourier transformed to produce the vibrational spectrum (see Figure 3.3). In this approach, whilst it is not straightforward to analyze individual modes, as with a normal-mode analysis, performing the Fourier transform for selected atoms allows us to block out regions of the spectra for the different elements present. Hence although we cannot positively identify the nature of each vibrational mode, we can identify which modes correspond to which ions: e.g. peaks occurring in the 3000-3500 cm^{-1} range occur only on the hydrogen and oxygen element plots, and therefore relate to frequencies involving the water molecules only.

The calculated vibrational spectra of sodium formate dihydrate showed a number of easily identifiable peaks, with, for example the only vibration occuring from just carbon and hydrogen at 2910 cm^{-1}, which can be easily attributed to the formate C-H vibration. Similarly, two CO vibrations can be observed at 1300 and 1550 cm^{-1} which can be attributed to the formate ions (presumably C-O and C=O respectively). The low-frequency sodium vibration has been included. However, it is worth noting that this vibration will have occurred only seven times throughout the

length of the simulation (ca. 1 ps), so large errors are expected on the value of 280 cm^{-1}. Since interactions with the sodium ion are relatively weak, vibrations are expected to be in the far infrared region. Finally, O-H vibrations form a band between 3110 cm^{-1} and 3530 cm^{-1}.

The accuracy of the phase I simulations assured us that, as expected, PW-DFT calculations can successfully reproduce the key features of the unit cell. We now turn to the new high-pressure phase.

3.3.2 Phase II- high pressure

The high-pressure (hydrogen, $_1$H) structure crystallises at 1.7 GPa in a monoclinic $P2_1$ unit cell with unit cell parameter of *a*=7.685Å, *b*=3.511 Å, *c*=8.110 Å and β=111.78° as measured by X-ray diffraction. Each sodium ion retains the octahedral field as seen at ambient pressure. However, the sodium ions are now coordinated by three tridentate formate ions, two bidentate, and one monodentate water molecule (note each water molecule is experimentally only observed as an oxygen atom). The polydentate ligands bridge between adjacent sodium ions to form columns. Naturally finding the hydrogen atoms is imperative, as a hydrogen-bonding network, binding the sodium columns (figure 3.4), is likely to be a main driver dictating the crystal packing. Our computational studies were initialised with a structure where hydrogens were added so that no hydrogen atoms interrupted the octahedra and a simple hydrogen-bonding network was present. Initial optimisations showed large heavy-atom atomic displacements. This is often seen when one or two of the unit-cell axes are significantly shorter than the others, and the problem can often be alleviated by performing the simulation in a supercell (essentially adapting the unit cell to be as cubic as possible). In the case of sodium formate dihydrate phase II the b axis is less than half the a or c axis, so using a 1×2×1 supercell allowed the simulation to reproduce the heavy-atom positions. After optimising the supercell a minimal volume expansion was recorded (1.5%). Although P1 symmetry was used for the optimisation, the structure remained close to the experimental $P2_1$ space group. Adding energy to the system (MD simulation) resulted in no significant change in geometry, indicating that no other local minima were accessed in the simulation.

Comparing experimental heavy-atom distances with those calculated shows minimal differences. Na-O distances differed by a maximum of 0.066 Å, whilst the maximum bonded distance differed by at most 0.083 Å (formate ion), well within computational boundaries.

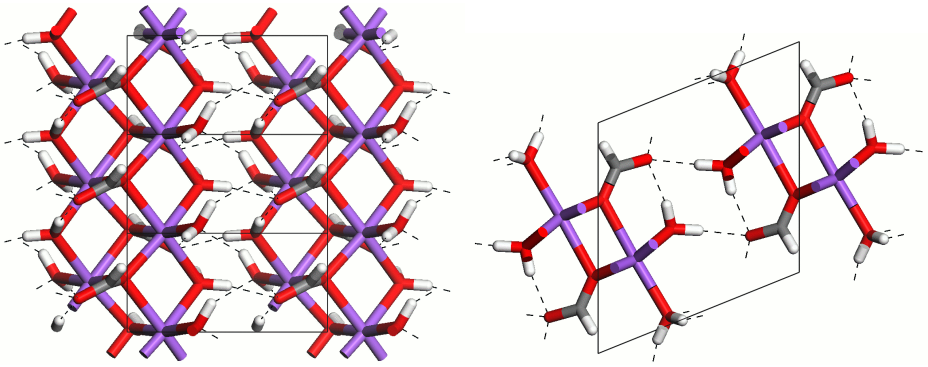

Figure 3.4 Computationally optimised phase II structure of sodium formate dihydrate, viewed along the *y* (left) and *z* (right) axes.

The predicted vibrational spectra showed many easily identifiable features, similar to that of phase I. The C-O vibrations have blueshifted by up to 20 cm^{-1} (to 1310 cm^{-1} and 1570 cm^{-1}), whilst the hydrogen vibrations have redshifted by as much as 50 cm^{-1} (figure 3.5), demonstrating that the hydrogen bond vibrations have been significantly affected by pressure. Subsequent neutron diffraction has allowed definitive proof of hydrogen (deuterium) positions. Heavy, high intensity, atoms appear in the same place with both hydrogen and deuterium structures leading to the belief that the isotopic substitution effect has little consequence at high pressure.

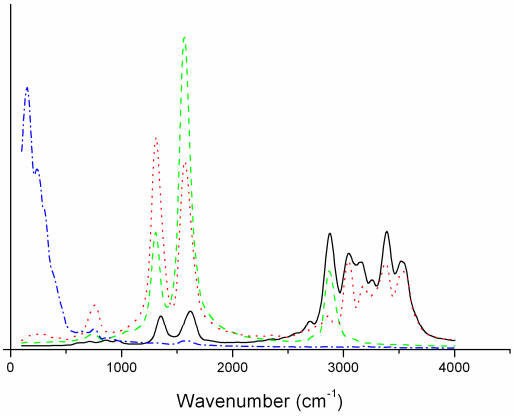

Figure 3.5 Calculated high pressure vibrational spectra. Solid line = hydrogen vibration, dashed line = carbon vibration, dotted line = oxygen vibrations and dot dashed line = sodium vibrations.‡

3.4 Conclusions

A new high-pressure phase of sodium formate dihydrate has been observed by X-ray diffraction with the hydrogen-atom positions found quantum mechanically, which were subsequently verified by a neutron difraction study. The ambient-pressure phase (phase I) is more stable by 3.25 kJ mol^{-1} (per $NaCO_2.2H_2O$) than the high-pressure phase (phase II). Both the ambient and high-pressure crystal structures of sodium formate dihydrate are characterised by six-coordinate Na^+ cations. In the ambient-pressure phase I crystal structure the Na^+ cation is coordinated to four water molecules and two formate anions, which form the vertices of an octahedral coordination environment. The octahedra are corner-sharing along the c axis direction and edge sharing along the b axis, to form slabs which are disposed in planes parallel to (0 1 0). These slabs are interconnected by hydrogen bonds; see Figure 3.2. At 1.7 GPa (or deuteration of the formate and water molecules), the coordination environment of the Na^+ cation changes substantially and, although an octahedral coordination environment is retained in the high-pressure structure, three water molecules and three formate anions now form the vertices of the octahedra. Each octahedron is edge-sharing with four of its neighbours so that columns of molecules are formed, that lie parallel to the monoclinic b axis, with adjacent columns bridged by hydrogen bonds; see Figure 3.4.

In the course of our neutron diffraction studies, we have found that there is a substantial deuteration effect on the ambient-pressure crystal structure and a previously unobserved $NaDCO_2.2D_2O$ polymorph is observed. The structure of this phase has monoclinic $P2_1/n$ symmetry and it is related to the high-pressure $P2_1$ phase via a translation of alternate Na-coordination columns parallel to the b axis.

‡ As the *y*-axis on our calculated spectrum is simply a measure of multiplicity, to make this graphically visible the sodium vibrational plot on Figure 3.3 was increased by a factor of 30 and on figure 3.5 increased by a factor of 50.

References

[1] A. M. Heyns, *J. Chem. Phys.*, **84**, 3610 (1986).

[2] L. Merrill and W. Bassett, *Rev. Sci. Instrum.*, **45**, 290 (1974).

[3] M. Walker, C. A. Morrison and D. R. Allan, *Phys. Rev. B.*, **72**, 224106 (2005).

[4] M. Nardelli, *J. Appl. Cryst.*, **32**, 563 (1999).

[5] SMART, Bruker AXS, Madison, Wisconsin, 1993; GEMINI, BrukerAXS, Madison, Wisconsin, 1999; SAINT Area-Detector Software Package, Bruker AXS, Madison, Wisconsin, 1997.

[6] A. Dawson, D. R. Allan, S. Parsons and M. Ruf. *J. Appl. Cryst.*, **37**, 410 (2004).

[7] S. Parsons, SHADE (2004), University of Edinburgh.

[8] G. M. Sheldrick, SADABS (2004). version 2004/1. University of Göttingen Germany.

[9] D. J. Watkins, C. K. Prout, J. R. Carruthers, P. W Betteridge and R. I. Cooper,CRYSTALS, Issue 12.0, Chemical Crystallography Laboratory, Oxford, UK, 2003.

[10] G. Kresse and J. Furthmueller, *Comp. Matter. Sci.*, **6**, 15 (1996).

[11] D. Vanderbilt, *Phys. Rev. B*, 41, 7892 (1990).

[12] J. P. Perdew, J. A. Chevary, S. H. Vosko, K. A. Jackson, D. J. Singh and C. Fiolhais, *Phys. Rev. B*, **46**, 5571 (1992).

[13] In-house code following accepted literature practise (M. P. Allen and D. J simulation of liquids).

[14] ISIS (1997) PEARL - Pressure and Engineering Research Line. In ISIS 97 - ISIS Facility Annual Report 1996-97, Rutherford Appleton Laboratory: 1997; ***Vol.*** **RAL-TR-97-050**, pp 28-29;

[15] ISIS (1996) Dedicated Facility for High Pressure Diffraction. In ISIS 96 - ISIS Facility Annual Report 1995-96, Rutherford Appleton Laboratory: 1996; ***Vol.*** **RAL-TR-96-050**, pp 61-62;

[16] J. M. Besson, R. J. Nelmes, G. Hamel, J. S. Loveday, G. Weill and S. Hull, *Physica B*, **180**, 907 (1992).

[17] R. J. Nelmes, J. S. Loveday, R. M. Wilson, J. M. Besson, S. Klotz, G. Hamel and S. Hull, Proceedings of the Symposium on Time-of-Flight Diffraction at Pulsed

Neutron Sources, 1994; J. D. Jorgensen and A. J. Schultz, *Eds., Amer Crystallographic Assoc: Buffalo,* **29**, 19.

[18] W. G. Marshall, and D. J. Francis. J. *Appl. Cryst.*, **35**, 122 (2002).

[19] W. G. Marshall, (1996) unpublished.

[20] A. C. Larson and R. B. Von Dreele, (2000) Los Alamos National Laboratory Report LAUR 86-748.

[21] B. H. Toby, *J. Appl. Cryst.*, **34**, 210 (2001).

[22] A. D. Fortes, Ph.D. Thesis, University of London, 2004; A. Z. Kuznetsov, V. Dmitriev, L. Dubrovinsky, V. Prakapenka and H.-P. Weber, *Solid State Comm.*, **122**, 125 (2002); R. A. Miller and D. E. Schuele, *J. Phys. Chem.* Solids, **30**, 589 (1969); D. L. Waldorf and G. A. Alers, *J. Appl. Phys*., **33**, 3266 (1962).

[23] K. Mueller, K.-J. Range and A.M. Heyns, *Z. Naturforsch., B: Chem. Sci*., **49**, 1179 (1994).

Chapter 4

Nitric Acid Monohydrates

4.1 Introduction

Nitric acid (HNO_3) is a strong, corrosive and non-volatile inorganic acid. It can be formed in the atmosphere by the conversion of nitrogen monoxide into nitrogen dioxide, and ultimately into nitric acid. This atmospheric nitric acid is one of the main constituents of polar stratospheric clouds and is thought to be one of the main contributors to the chemistry of ozone depletion. As the nitrogen monoxide required for the production of atmospheric nitric acid is closely associated with the combustion of fossil fuels, several studies have been conducted on the behaviour of a number of nitric acid hydrates, their phase diagrams and the crystalline structures of their different solid phases[1,2].

Nitric acid is known to form three hydrates, incorporating one, two or three water molecules, and a report has suggested the presence of a pentahydrate structure[3]. The first ambient pressure X-ray structure of nitric acid monohydrate (NAM) was reported by Luzzati[4], but as this structure failed to locate the hydrogen atoms, a more detailed structure was later reported by Delaplane[5]. The structure at ambient pressure is described as a network of $[H_3O]^+$ and $[NO_3]^-$ ions, which is consistent with NMR spectroscopy[6]. The crystal structure has pseudo-threefold symmetry around each of the ions. A network of H-bonds are present which form puckered slabs of $[NO_3]^-.[H_3O]^+$. There are no H-bonds between adjacent slabs (see Figure 4.1).

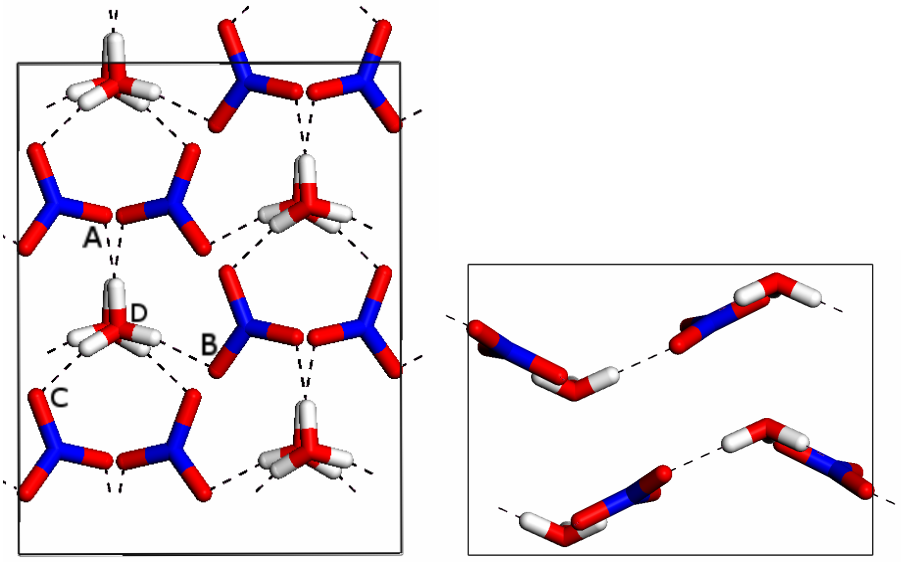

Figure 4.1 Phase I (ambient pressure) crystal structure of nitric acid monohydrate as viewed along the c (top) and a (bottom) axes. Hydrogen bonds are indicated with a dotted line. Labels A, B, C and D correspond to those in table 4.2.

We have now extended this work by undertaking a high-pressure single-crystal X-ray diffraction study of the nitric acid monohydrate species to 43 kbar and, to date, we have obtained two new phases. High-pressure crystallography makes use of the "neglected" thermodynamic variable and can be used to probe the balance between strong intramolecular forces and weak intermolecular forces in molecular solids. However, the method has one major limitation in that the diamond anvil cell used to compress the sample physically prevents the wide-angle diffraction data from being collected. As a consequence, high-pressure crystallography often generates refined structures of lower precision compared to standard X-ray crystallographic studies. But, by far the most serious implication relates to the positions of hydrogen atoms, which are at best difficult, and more often impossible, to assign. In some cases it may be possible to place hydrogen atoms intuitively following a careful visual inspection of the molecular geometry, but this can be unsatisfactory and creates an element of doubt in the resulting structure. This can be a particular difficulty if the intermolecular hydrogen-bonding network is the key interaction dictating the crystal packing arrangement. The use of solid-state quantum mechanical

modelling has, therefore, recently been used to resolve this issue successfully. Applying a similar methodology to that of Allan and Clark[7,8] complex H-bonding networks have been solved.

By taking the experimentally determined heavy-atom positions and placing the hydrogen atoms in physically reasonable starting positions, a structure can then be calculated that corresponds to an energy minimum. Altering the hydrogen positions and subsequently re-optimising acts as a secondary probe of the potential-energy surface (PES) and confirms that the geometry obtained was indeed the global minimum. Once found, additional studies can then be performed. For example, a molecular dynamics calculation animates the structure over a certain timescale at a given temperature, and thereby gives information about atom mobility and molecular binding which cannot be obtained from the static structure. Moreover, vibrational frequencies can be extracted from this simulation, automatically corrected for anharmonic effects, which provides another useful indicator of hydrogen-bonding interactions.

A number of previous computational studies on NAM have been published[9,10,11,10]. Escribano and Fernández initially studied a gas-phase dimer and found (at cc-pVTZ, B3LYP) the $HNO_3.H_2O$ moiety to be of lower energy. This study was followed by simulations using localised/pseudopotential basis sets with the density functional theory (DFT) formalism and showed that, in the solid phase $[H_3O]^+.[NO_3]^-$ was the more stable structure. Earlier work by Tóth[12] supported this with similar calculations using a plane wave/pseudopotential basis set. All four authors reported vibrational analysis of the species studied. The gas-phase calculations predicted $[H_3O]^+$ vibrations some 1000 cm^{-1} too high compared to the experimental condensed phase data[13,14], indicating that the gas-phase dimer model is not an appropriate representation of solid NAM. For the calculations utilising periodic boundary conditions, the predicted bands fell within expected computational limits of spectra measured experimentally[13,14].

In this chapter we report on the two new phases obtained for nitric acid monohydrate up to 43 kbar using X-ray crystallography. High-level quantum mechanical calculations (plane-wave density functional theory, PW-DFT) have been employed to complete the partial experimental structures. However, due to the nature of the structures presented, further theoretical techniques were required, allowing the hydrogen atom positions to be placed with a much greater degree of confidence.

4.2 Experimental and Computation Methodology

4.2.1 High-Pressure X-Ray Diffraction

The crystals were grown by loading and pressurising a 60% aqueous solution of nitric acid in a Merrill and Bassett diamond-anvil cell[15] that had been equipped with 600 μm culet diamonds and a tungsten gasket. The gasket had been pre-indented to a thickness of 100 μm and had a 200 μm hole drilled through it. As tungsten has a thick, inert, oxide layer, it is unreactive – even at the elevated pressures of the experiment. After the nucleation of several crystallites, the temperature was cycled close to the melting curve in order to reduce the number of crystallites, in a manner similar to that of Vos *et al*[16]. Finally, a single crystal was obtained at an initial pressure of 11 kbar. Subsequent pressure increase and a further two recrystallisations yielded new phases at 42 and 43 kbar.

The setting angles of strong reflections were determined for all three sample crystals on an Enraf-Nonius CAD4 diffractometer (equipped with a Mo X-ray tube) and a least-squares fit, following initial indexing, yielded orthorhombic unit cell parameters, for all three phases, listed in Table 4.1. Intensity data were collected for the crystals with the ω-scan method, at the position of least attenuation of the pressure cell, according to the fixed-ϕ technique. All accessible reflections were measured in the hemisphere $\pm h, \pm k, +l$ for the 11 kbar data set, and in the hemisphere $+h, \pm k, \pm l$ for the data collected at 42 kbar and 43 kbar, for $0\ \text{Å}^{-1} < \sin\theta/\lambda < 0.71\ \text{Å}^{-1}$. The intensities were corrected for absorption, averaged, and then used for structure solution by direct methods. The systematic absences were consistent with $Pna2_1$, *Pbca* and *Pcam* space groups for the 11 kbar, 42 kbar and 43 kbar data sets

respectively, and trial structural solutions in these symmetries were found to be acceptable. The final structural models were refined using the CRYSTALS suite of programs and the structural parameters for the various fits, along with the refinement statistics, are listed in Table 4.1. As the data and crystal quality deteriorated with pressure, the treatment of the atomic displacement parameters (or thermal parameters) was carried out differently in each of the three structural refinements. The data for both the 11 kbar, $Pna2_1$, structure and the 42 kbar *Pbca* structure were of sufficient quality for the displacement parameters to be refined anisotropically. However, a similarity constraint had to be applied to the *Pbca* structural refinement to ensure that the anisotropic displacement parameters remained physically reasonable. The 43 kbar data set contained a relatively large number of weak reflections and to overcome the concomitantly poor data-to-parameter ratio the atomic displacement parameters were refined isotropically.

Pressure / GPa	1.1	4.2	4.3
Crystal system	Orthorhombic	Orthorhombic	Orthorhombic
Space Group	$Pna2_1$	Pbca	Pcam
a/Å	6.051(5)	8.774(10)	4.476(3)
b/Å	8.473(5)	5.780(4)	5.464(8)
c/Å	5.364(5)	9.782(7)	10.096(17)
Volume/Å^3	275.0(4)	496.1(7)	246.9(6)
No. reflections for cell	22	25	25
$2\theta_{max}$(°)	80	80	76
Z	4	8	4
Reflections collected	684	1201	549
No. Unique [R_{int}]	317 [0.098]	450 [0.045]	242 [0.144]
No. $F>2\sigma(F)$	201	185	89
Parameters	47	21	13
R_1 [$F>2\sigma(F)$]	0.0561	0.1135	0.1331
wR_2 (*F*, all data)	0.0355	0.0572	0.1099
S	1.265	1.012	1.147
$\Delta\rho_{max}$ (eÅ^{-3})	0.25	0.62	0.61
$\Delta\rho_{min}$ (eÅ^{-3})	-0.30	-0.63	-0.50

Table 4.1 Crystallographic data for nitric acid monohydrate at increasing pressures.

4.2.2 Computational methods

Equilibrium structures for the nitric acid monohydrate series were obtained using the VASP 4.4 simulation package[17] according to the following procedure. Initial geometries and space-group symmetry constraints were taken from experiment. In the case of unlocatable hydrogen atoms, intuitive positions were selected based on a close inspection of the heavy-atom positions and assuming a planar structure for the $[H_3O]^+$ ion. A set of atomic position optimisations was performed initially so that a favourable hydrogen-bonding network would be in place before any volume change was permitted. This was then followed by a series of single-point energy calculations where the lattice constants (multipliers for the cell vectors) were varied, thus

establishing the volumes of the unit cells that gave rise to the lowest energies. All subsequent optimisations were then held at these fixed volumes. The atomic positions and lattice parameters were then optimised on alternate cycles until convergence was achieved. Phase I NAM calculations were performed in *P1* symmetry in a 1×1×2 supercell. For all other structures a 1×1×1 (i.e. crystallographic) cell was used and the appropriate symmetry constraints applied. Simulations were performed using a set of ultrasoft pseudopotentials[18] and plane waves expressed at an energy cut-off at 396 eV. The generalised gradient approximation (GGA) functional PW91[19] was used to model the exchange and correlation potentials, and the Brillion zone sampled by one k-point at the gamma (Γ) position. Convergence criteria were set such that optimisation was achieved once forces reached less than 10^{-3} eV A^{-1} and SCF energy less than 10^{-4} eV. In order to confirm that the equilibrium structures obtained were the global minima, second optimisations were performed using new initial geometries that differed radically in hydrogen-atom positions. New hydrogen locations were selected based on an unintuitive structure, where little or no H-bonding could be inferred. Following the optimisation procedure outlined above, second equilibrium geometries were obtained; comparing geometries (and associated energies) with those obtained in the first optimisations allowed confirmation as to whether global minima positions had been identified.

The equilibrium structure work was then followed by a series of PW-DFT micro canonical (NVE) molecular dynamics calculations performed in *P1* symmetry, in order to search the potential-energy surface more completely, and to investigate the effects of temperature (i.e. free energy) on the resulting thermally averaged structures. This also offered the opportunity to extract solid-state vibrational frequencies from the simulation by Fourier transformation of the autocorrelation function of the calculated forces, with low-frequency noise subtracted from the resulting spectra using a Blackman windowing function[20]. The basis set cut-off was lowered to 297 eV, and identical convergence criteria and k-point sampling as for the equilibrium calculations were used. With the equilibrium structures used as starting points, MD simulations were run using a time step of 0.7 fs, determined following

careful consideration of the highest energy vibrational frequency for the system (the OH stretch). Confirmation of this time-step was obtained by careful analysis of the resulting conservation of free energy in the NVE ensemble. The first 0.14 ps of each simulation was discarded to allow the system to reach equilibrium; data were then accrued over a further 0.7 ps. Averaged equilibrium temperatures obtained for the three phases were 246(22), 233(23) and 248(26) K, respectively.

It is worth noting that our modelling approach is not without its flaws. As we have held the volume at a constant value (as obtained in the equilibrium calculation) throughout all our MD calculations, we have effectively increased the pressure since thermal expansion causes an increase in volume that has not been accounted for. In addition, our calculations have at their heart density functional theory, with all the standard limitations that this method entails (e.g. the dispersion forces are not modelled). Nevertheless, our simulations have successfully reproduced the key features of the crystal structure geometries and experimental vibrational spectra within acceptable levels of accuracy for the nitric acid monohydrate series of structures.

Finally, isolated molecule calculations were performed in a box of vector length 10 $Å^3$. The box size was chosen in an attempt to reduce monopole-monopole interactions, yet keep the calculation size reasonable. To ensure a saturated plane-wave basis set, an energy cutoff of 800 eV was chosen. All other features of the calculations remain identical to those previously described for optimisations.

4.3 Results and discussion

4.3.1 Phase I- ambient pressure

A complete structural study of the ambient pressure phase of nitric acid monohydrate (NAM) was reported by Delaplane *et al*. As all atoms were located with a high degree of confidence, our computational investigation began with this structure, thus allowing the accuracy of the simulation to be assessed. Initial calculations yielded disappointing results, with large atomic displacements observed between calculated and experimental structures, causing the nitrate plane to tilt. A similar problem had been reported by Fernández, who noted that the problem could be alleviated by performing calculations on a supercell (1×1×3), rather than the 1×1×1 crystallographic unit cell. In our work we found that a 1×1×2 supercell was in fact sufficient; from this point on all results relating to ambient pressure calculations were performed in *P1* symmetry on a 1×1×2 supercell.

The resulting (calculated) equilibrium structure compared well with that obtained by Delaplane (see Table 4.2), with the majority of heavy-atom distances reproduced to within 0.03 Å and a minimal volume increase (1.5%; as current DFT functionals cannot calculate dispersion forces, some volume expansion is nearly always expected). Visual superposition of the two structures confirmed that the calculated minimum corresponded with that obtained from experiment. Although removal of the symmetry constraints in the calculation allowed subtle local changes, a geometry with close pseudo-$Pna2_1$ symmetry was maintained throughout.

	Ambient pressure		High pressure	
	Experimental[a]	Calculated (1×1×2)	Experimental[b]	Calculated (1×1×2)
Lattice (Å,°)				
a	6.2308(1)	6.2640	6.051(5)	6.1172
b	8.6439(1)	8.6889	8.473(5)	8.5491
c	5.4647(1)	10.9782	5.364(5)	10.8362
α = β = γ	90	90	90	90
Volume (Å^3)	294.32(1)	597.52	275.01(65)	566.69
Geometry[c] (Å)				
N-O_A	1.267	1.267	1.253	1.266
N-O_B	1.264	1.270	1.261	1.270
N-O_C	1.246	1.271	1.255	1.269
O_D---O_A	2.606	2.560	2.593	2.551
O_D---O_B	2.59	2.570	2.604	2.572
O_D---O_C	2.576	2.569	2.561	2.569
Energy/eV	-	-352.27610	-	-351.74466

Table 4.2 Selected experimental and computed (equilibrium structure) parameters for phase I (ambient and high pressure) nitric acid monohydrate (NAM).

In order to further explore the potential-energy surface (PES), a molecular dynamics (MD) calculation was then undertaken. This allowed direct visualisation of the flexibility of the system and local wells to be accessed if the system has enough thermal energy to overcome any potential-energy barriers. Visualisation of the MD simulation showed that, despite the lack of symmetry constraints, the *Pna2₁* space group was also essentially retained in this calculation. Furthermore, the main geometrical features were maintained, indicating a lack of close energy minima. Following the MD calculation, the forces were extracted from each step, subjected to an autocorrelation function and the resulting plots Fourier transformed to produce the vibrational spectrum (see Figure 4.2 and Table 4.3). In this approach whilst it is not straightforward to analyze individual modes, as with a normal mode analysis,

performing the Fourier transform for selected atoms allows us to block out regions of the spectra for the different elements present. Hence although we cannot positively identify the nature of each vibrational mode, we can identify which modes correspond to which ions: e.g. peaks occurring in the 2400-3000 cm^{-1} range occur only on the hydrogen and oxygen element plots, and therefore relate to frequencies involving the $[H_3O]^+$ ions only. Similarly, the $[NO_3]^-$ vibrations are predominately located between 700 and 1700 cm^{-1}. Vibrational spectra for NAM have been obtained experimentally and calculated by a number of authors. Our simulated spectra compare well with the experimental thin film studies[10,13,14].

Assignment [a]	Experimental	Calculated			
	Ambient pressure Phase I[a]	Ambient pressure Phase I	High pressure Phase I	High pressure Phase II	High pressure Phase III
asym str ν_3 $[H_3O]^+$	2644	2250-2940	2540-3040	2200-3200	2150-3185
sym str ν_1 $[H_3O]^+$	2230	2250-2940	2160-2540	2200-3200	2150-3185
asym bend ν_4 $[H_3O]^+$	1671	1650	1660	1670	1690
asym str ν_3 $[NO_3]^-$	1260, 1316	1310	1290	1250, 1420	1300, 1420
sym str ν_1 $[NO_3]^-$ [b]	-	1000	1000	990	960
sym bend ν_2 $[H_3O]^+$	1115	1200 (weak)	1160 (weak)	1150	1115 (weak)
sym bend ν_2 $[NO_3]^-$	813	760	750	750	750
asym bend ν_4 $[NO_3]^-$	735, 722	690	680	710, 830	680

Table 4.3 Calculated and experimental vibrational frequencies (cm^{-1}) for phase I (ambient and high pressure), phase II and phase III nitric acid monohydrate.

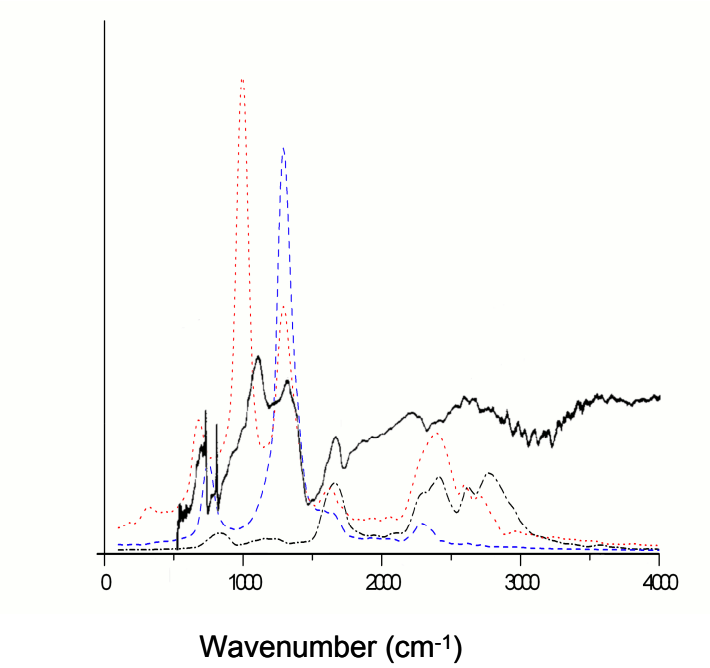

Figure 4.2 Predicted vibrational spectra for the ambient pressure Phase I NAM. Dotted line indicates oxygen vibrations, dashed line nitrogen and dot dashed line hydrogen.

Although our spectra are rather noisy and some signals rather broad, we appear to be matching the experimental spectra to within 2-10% for most peaks. In particular, in the case of the O-H symmetric and asymmetric stretching bands we have generated broad absorption bands in the correct region and closer to the experimental wavenumbers than the previously reported calculations, which were consistently higher than ours but nevertheless broadly consistent with our findings.[11,13,14] In any case, it should be remembered that the experimental bands for these two modes are also broad, noisy signals and so the literature values quoted are only approximate. Since vibrational frequencies obtained in our calculation do not impose the harmonic approximation they automatically include the effects of anharmonicity, which may be the reason for the improvement in fit with experiment that we observed in our results. Note, in the spectra obtained for all phases we calculated a peak at *ca.* 840 cm^{-1}, which is not recorded in the experimentally available data. We tentatively assign this peak to a weak $[OH_3]^+$ A_1 stretch (calculated in the gas phase, PW91, 6-31g* at 920 cm^{-1})[21]. As this peak is only

observed weakly in calculated spectra, it is not surprising experimentalists failed to observe this peak.

4.3.2 Phase I - 11 kbar

Our high-pressure crystallographic work (11 kbar) indicated a unit cell and heavy-atom structure very similar to the phase I, ambient-pressure, structure (see Table 4.2). As this study was unable to locate any hydrogen atoms, computational input was required to complete the structure. To this end, hydrogen atoms were placed in positions favourable for hydrogen bonding following a close inspection of the heavy-atom positions. In addition, in order not to bias the calculation, the oxonium $[H_3O]^+$ ion was assumed to be planar (*pseudo-*D_{3h} symmetry), although the space-group symmetry constraints imposed on the calculation ($Pna2_1$) would allow the local symmetry to drop to the non-planar (*pseudo-*C_3) arrangement.

A test calculation (atom optimisation only) showed a similar atomic displacement to that observed at ambient pressure; although hydrogen motion was to be expected, the experimentally well-defined heavy-atom displacement was a cause for concern. As the unit cell was very similar to the ambient-pressure structure we repeated the optimisation in *P1* symmetry using a 1×1×2 supercell and this approach was again found to be effective. Our calculated equilibrium structure gave a final unit cell volume of 566.7 $Å^3$, which is 3% larger than that of the experimental volume (550.0 $Å^3$,1×1×2 supercell). This is well within acceptable computational limits. Additionally, most heavy-atom distances were now reproduced to within 0.03 Å. Further, more stringent, tests were then carried out to probe the PES further from the minimum. This was achieved by altering the hydrogen positions so that either no hydrogen bonding could be observed or that a different hydrogen-bonding network existed. The majority of these structures reverted to the original equilibrium structure (with any minor energy differences attributed to convergence criteria). The results from these calculations differed in energy by at most 0.54 kJ mol^{-1} (per unit cell) and as all structures could be superimposed upon the equilibrium geometry this confirmed that the global minimum had indeed been achieved. A second non-

identical structure was found from these calculations but at a much higher energy (56 kJ mol^{-1} higher per cell) and so considered not to be significant.

Following the equilibrium geometry calculations, an NVE MD simulation was undertaken, with the temperature equilibrating at *ca.* 200 K. Animating the resulting simulation indicated that again there were no easily accessible close energy minima. All geometrical features observed in the equilibrium structure were maintained. We thus conclude that a pressure-induced crystallisation of phase I NAM has occurred, and the ambient-pressure phase must continue to be the most stable polymorph at pressures in the region of 11 kbar. As expected the high-pressure phase I calculated vibrational spectrum (Figure 4.3, Table 4.3) bore strong resemblance to that calculated for the ambient pressure phase. Superposition of the two plots (see Figure 4.4) showed very little difference except for subtle differences in the hydrogen-bonding region (2000-3000 cm^{-1}).

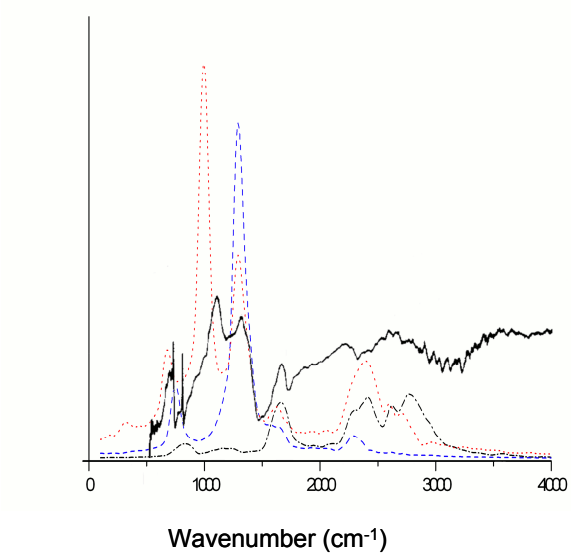

Figure 4.3 Predicted vibrational spectra for high pressure phase I NAM. Dotted line indicates oxygen vibrations, dashed line nitrogen and dot dashed hydrogen. The solid spectra indicates experimental results as obtained by Smith *et a1*.[13]

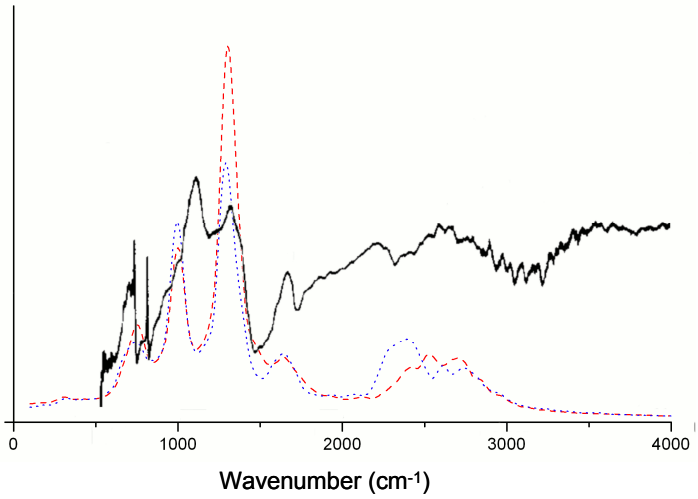

Figure 4.4 Predicted vibrational spectra for ambient and high-pressure phase I NAM. Dashed line indicates ambient-pressure and dotted line indicates high-pressure. (All vibrations have been combined). The solid spectrum indicates experimental results as obtained by Smith *et a1*.[13]

Most vibrational frequencies increase with pressure. An increase in frequency can be regarded as the potential well becoming steeper and for any system with anharmonicity the vibrational frequencies will be expected to change. Frequencies involving hydrogen atoms are more susceptible to change because small percentage changes in frequency manifest themselves as larger absolute differences in frequency and O-H vibrations are often appreciably anharmonic. Thus, in our simulations of this modest pressure increase we would expect to see changes in the O-H stretching region; N=O frequencies will be relatively unaffected. We conclude that our work on phase I (ambient and high-pressure) indicates that one potential-l energy minimum is present in both structures. The ambient-pressure minimum has been fully identified by Delaplane *et al.* and in this work the high pressure minimum obtained at 11 kbar has been studied and shown to be of the same architecture.

4.3.3 Phase II – 42kbar

Increasing the pressure further and recrystallising from the melt yielded a new phase at 42 kbar. Experimental parameters gave a heavy-atom structure with a very similar bonding motif to that observed at lower pressures (see Figure 4.5). The symmetry altered to *Pbca* and the unit cell parameters have increased to give a cell volume some 70% bigger with twice as many molecules as in the ambient pressure cell. Note that the primitive cell for this phase corresponds to the 1×1×2 supercell employed for phase I. The new bonding motif alters the nitrate ion and now three separate lengths are clearly visible (see Table 4.4). The more hydrogen bonds that are associated, the longer the bond (see Figure 4.5), such that $N\text{-}O_A < N\text{-}O_B < N\text{-}O_C$. Elongation upon increasing hydrogen coordination is a well recorded effect. For a review see Steiner[22].

	Experimental	Calculated	Experimental	Calculated
Lattice (Å,°)	Phase II	Phase II	Phase III	Phase III
a	8.774 (10)	8.7383	4.476	4.0635
b	5.780 (4)	6.050	5.464	6.0787
c	9.782 (7)	9.812	10.096	10.3760
$\alpha = \beta = \gamma$	90	90	90	90
Symmetry	*Pbca*	*Pbca*	*Pcam*	$Pca2_1$
Volume ($Å^3$)	496.1 (8)	518.7	246.9	256.3
Geometry[a] (Å)				
N-O_A	1.215	1.243	1.220	1.239
N-O_B	1.246	1.280	1.251	1.261
N-O_C	1.261	1.297	1.220	1.316
O_D---O_B	2.566	2.561	2.608	2.575
O_D---O_C	5.588	2.631	2.686	2.481
O_D---O_E	2.594	2.601	2.846	2.463
Energy (eV)	-	-350.03845	-	-176.55892

Table 4.4. Selected equilibrium geometries of NAM Phase II and Phase III.

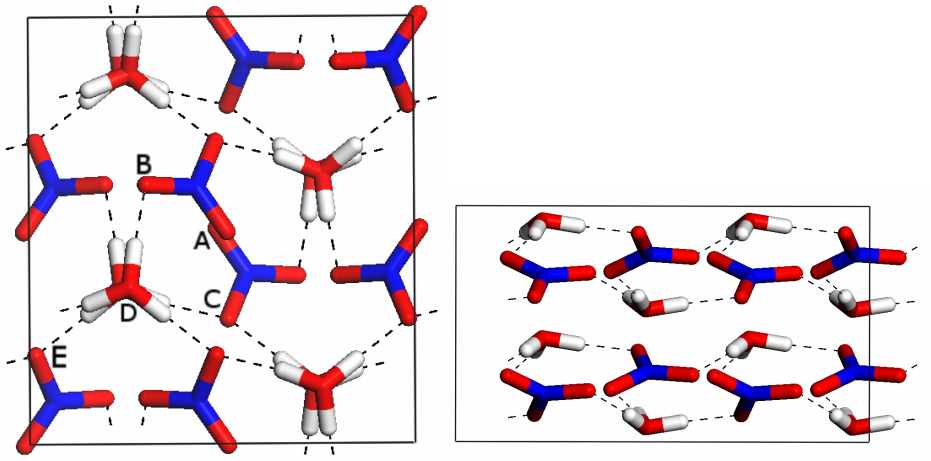

Figure 4.5 Phase II NAM, as viewed along the a (top) and b (bottom) axes. Hydrogen bonds are indicated with a dotted line. Labels A, B, C and D correspond to those in Table 4.4.

The equilibrium geometry calculation used the experimental unit-cell parameters, heavy-atom positions and estimated (planar $[H_3O]^+$) H positions for initial input. The results obtained are shown alongside the experimental geometry in Table 4.4. The equilibrium structure compared well with that obtained experimentally, with the majority of heavy-atom distances reproduced to within 0.04 Å and a minimal volume increase (4.6%). Visual superposition of the two structures confirmed that the calculated minimum corresponded to that obtained from experiment. The structure is very similar to that of phase I, although the increase in pressure caused the hexagonal style channels in which the oxonium ions are located to become better aligned due to the increased symmetry of the *Pbca* space group, so that the channels more closely approximate a pseudo-hexagonal geometry. With regards to the hydrogen-bonding network, alterations have caused one of the nitrate oxygens to have no hydrogen bonds, whilst another is now bifurcated and the third unchanged. This enables each molecule to thus retain three hydrogen bonds and again, as for phase I, the crystal is composed from slabs which are not interconnected by hydrogen bonds.

The MD simulation retained the main geometric features obtained in the equilibrium optimisation (including *pseudo-Pbca* space-group constraints), indicating that no other local minima were sampled in the calculation. This is not surprising given the similarity to phase I: hydrogen locations were straightforward to select, hence the initial geometry was close enough to the global minimum to not encounter any other minima. The integrity of the minimum obtained was then tested by restarting the simulation with random, but still physically reasonable, hydrogen atom positions. All but one of the structures perturbed in this way returned to that calculated initially, and as this outlier was higher in energy by some 90 kJ mol^{-1} (per unit cell) it was considered inaccessible and of no real significance.

The predicted vibrational spectra (Table 4.3) replicates many features shown in phase I with the most notable difference observed at 1420 and 830 cm^{-1} presumably due to the new H-bonding network forcing the doubly degenerate $[NO_3]^-$ ν_3 asymmetric stretch and ν_4 asymmetric bending modes to each split into two frequencies. We have not yet been successful in obtaining an experimental high-pressure IR spectrum of the high pressure phase II structure to verify these results as all attempts resulted in small water crystallites forming on the surface of the crystal, thus resulting in considerable interference with the sample signal.

4.3.4 Phase III – 43 kbar

The highest pressure structure obtained in this study occurred at 43 kbar. The heavy-atom structure indicated *Pcam* symmetry, but as this space group would constrain all oxoniums ions to be planar, for the computational study the symmetry was reduced to *Pca2₁*. Phase IV displayed none of the previous regular patterns observed in the lower pressure phases, that is to say hexagonal channels could no longer be observed. This lead to difficulties in selecting intuitive starting positions for hydrogen-atom geometries and so the light atoms were positioned as to favour no single hydrogen bond. Resulting optimisations produced an erroneous structure which had hydrogen bonds between $[H_3O]^+$•••$[NO_3]^-$ and $[H_3O]^+$•••$[H_3O]^+$ ion pairs. Upon initialising the MD simulation, where the symmetry was removed and energy added to the system, the structure changed substantially. Subsequent inspection of the resulting structures

showed that the oxonium ions rotated to form three hydrogen bonds (oxonium to nitrate) similar to the other phases (see Figure 4.6). The change in structure corresponded with a decrease in the free energy of the system, implying that this new structure was lower in energy, and hence a better approximation to the equilibrium geometry. For the calculated vibrational spectra (and geometry determination) only steps after this structure had stabilised were taken as useful data.

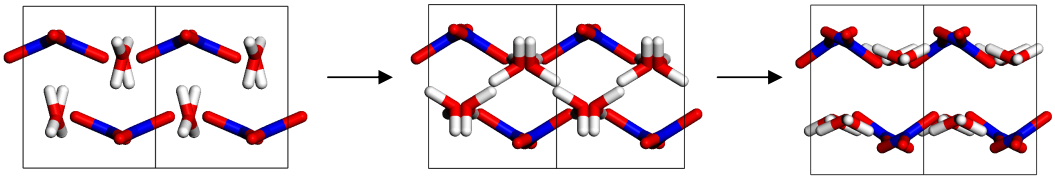

Figure 4.6 The progression of the structural optimisation for NAM phase III (as viewed down the 'c' axis). (a) Initial starting structure, (b) resulting optimised structure, (c) structure obtained from subsequent MD run.

As the MD simulation was performed in *P1* symmetry, a $Pca2_1$ structure was subsequently generated from this by applying symmetry to an arbitrary asymmetric unit. This structure was then optimised in accordance with the previous computational method. The newly obtained equilibrium geometry (see Table 4.4, Figure 4.7) showed some similarities with NAM phase II in that the structure was composed of hydrogen-bonded sheets and one of the nitrate oxygens is bifurcated between two hydrogens. This had similar effects on the bond lengths; the bifurcated oxygen is elongated with respect to the singularly H-bonded oxygen, which in turn is elongated with respect to the oxygen with no H-bonds. As a consequence, the predicted vibrational spectrum (Table 4.3) also showed many similarities with the phase II spectrum with, for example, a similar splitting of the asymmetric stretch.

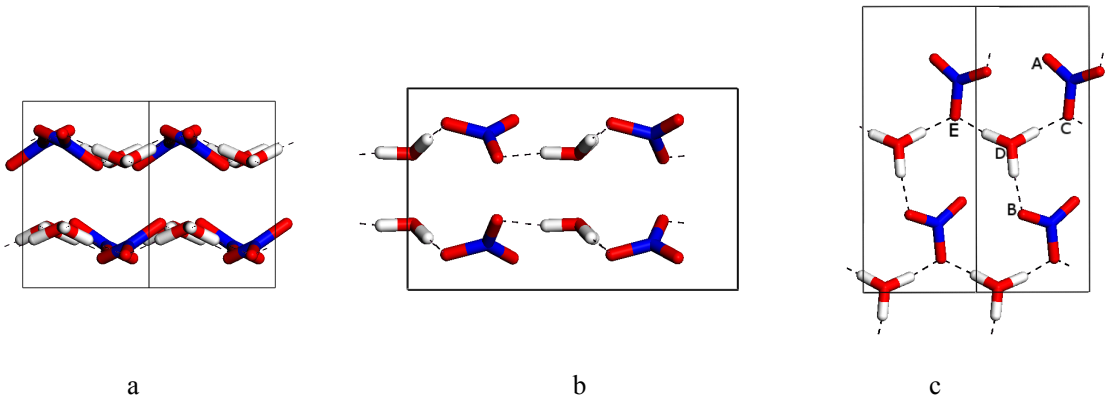

a b c

Figure 4.7 The final optimised structure for NAM phase III, (a) as viewed in the c axis, (b) the a axis, (c) and as a single slab taken from the 1 0 0 Miller plane. Labels A, B, C, D and E correspond to those in Table 4.4.

4.3.5 Calculated sublimation energies of the three phases of NAM

A final set of calculations was performed on the isolated species (H_2O, HNO_3, $[H_3O]^+$ and $[NO_3]^-$), as shown in Table 4.5. Comparing the energies of the molecules in the unit cells to those of the isolated molecules enables the total interaction energies, which can be thought of as approximating the sublimation energies, to be obtained. By dividing this value by the number of hydrogen bonds present average hydrogen-bond strengths can be obtained. [See Table 4.5; note that our values relate to the equilibrium (0 K) structure, and have not been corrected for the effects of zero-point energy.] Phases I and II clearly show that, as expected, increasing the external pressure caused the energy of the system to rise, and hence the average hydrogen-bond strength to decrease. Phase III, however, did not follow this trend, where a decrease in equilibrium energy and consequent increase in average hydrogen-bond strength was observed. This raised the question why Phase III appears to be overall the most stable and yet not occur experimentally until 43 kbar? As thermodynamic reasons cannot provide the answer (the change in volume between phases II and III is very small, leading to a small $P\Delta V$ term) we conclude that the process of crystallisation for this phase must be kinetically controlled.

Species	Energy (eV)	Average H-bond energy (kJ mol^{-1})[a]
H_2O	-14.248757	-
HNO_3	-28.592565	-
H_3O^+	-11.237980	-
NO_3^-	-28.477214	-
Phase I – ambient (per $H_3O.NO_3$ unit)	-44.0345125	38.4
Phase I – high (per $H_3O.NO_3$ unit)	-43.9680825	36.2
Phase II (per $H_3O.NO_3$ unit)	-43.7548063	29.4
Phase III (per $H_3O.NO_3$ unit)	-44.13973	41.8

Table 4.5 Summary of calculated energies for the NAM series. For Phases II and III the H-bond energy can only be regarded as an average as more than one type of H-bond is present in the crystal lattice.

4.4 Conclusions

The crystal structure of nitric acid monohydrate has been studied up to 43 kbar using X-ray crystallography and computational methods. Two new phases were found and characterised. Whilst X-ray crystallography was required to find the structures initially, computational methods were required to complete them. Although structural chemistry considerations could have been used to infer the hydrogen atom locations in the Phase-II and Phase-III structures from the oxygen-oxygen distances, the computational methods have not only provided us with the correct identification of the $Pca2_1$ symmetry of Phase-III but they have also offered us an unequivocal assignment of the bifurcated hydrogen bonds in both of these crystal structures. During the course of this work a simple computational methodology has been developed for exploring the local potential-energy surface. Using crystallographic input and applying a technique of heating (MD simulation) and cooling (optimisation) the system allows the structure to cross low-energy barriers and enter the lowest-energy geometry. In this manner the technique can be compared to a reverse simulated annealing in that heat is applied to the system to allow other

structures to be sampled, and on careful inspection the relative energies of any new structures can be observed. Hence, should a new, lower-energy, structure manifest itself during the simulation, it can be picked out for subsequent geometry optimisation calculation.

References

[1] N. Lebrun, F. Mahe, J. Lamiot, M. Foulon, J. C. Petit and D. Prevost, *Acta Crystallogr*., **B57**, 27 (2001).

[2] N. Lebrun, F. Mahe, J. Lamiot, M. Foulon and J. C. Petit, *Acta Crystallogr.,* **C57**, 1129 (2001).

[3] J. J. Marti and K. Mauersberger, *J. Phys. Chem*., **98**, 6897 (1994).

[4] P. V. Luzzati, *Acta Crystallogr.,* **4**, 239 (1951).

[5] R. G. Delaplane, I. Taesler and I. Olovosson, *Acta Crystallogr.,* **4**, 239 (1975).

[6] R. E. Richards and J. A. S. Smith, *Trans. Faraday Soc.,* **47**, 1261 (1951).

[7] D. R. Allan and S. J. Clark, *Phys. Rev. B,* **60,** 6328 (1999).

[8] D. R. Allan, S. J. Clark, M. J. P. Brugmans, G. J. Ackland and W. L. Vos, *Phys. Rev. B,* **58**, R11 809 (1998).

[9] R. Escribano, M. Couceiro, P. C. Gómez, E. Carrasco, M. A. Moreno and V. J. Herrero, *J. Phys. Chem. A*, **107**, 651 (2003).

[10] D. Fernández, V. Botella, V. J. Herrero and R. Escribano, *Phys. Chem. B,* **107**, 10608 (2003).

[11] D. Fernández, R. Escribano, T. Archer, J. M. Pruneda and E. Artacho, *Phys. Chem. A*, **108**, 10535 (2004).

[12] T. Tóth, *J. Phys. Chem. A,* **101**, 8871 (1997).

[13] R. H. Smith, M.-T. Leu and L. F. Keyser, *J. Phys. Chem*., **95**, 5924 (1991).

[14] G. Ritzhaupt and J. P. Devlin, *J. Phys. Chem.,* **95**, 90 (1991).

[15] L. Merrill and W. Bassett, *A. Rev. Sci. Instrum*., **45**, 290 (1974).

[16] W. L. Vos, L. W. Finger and R. J. Hemley, *Nature (London)*, **358**, 46 (1992).

[17] G. Kresse and J. Furthmueller, *Comp. Matter. Sci.*, **6**, 15 (1996).

[18] D. Vanderbilt, *Phys. Rev. B,* **41**, 7892 (1990).

[19] J. P. Perdew, J. A. Chevary, S. H. Vosko, K. A. Jackson, D. J. Singh and C. Fiolhais, *Phys. Rev. B,* **46**, 5571 (1992).

[20] in-house code following accepted literature practise (M. P. Allen and D. J. Tildesley, *Computer simulation of liquids*).

[21] Gaussian 98, Revision A.7 M. J. Frisch, G. W. Trucks, H. B. Schlegel, G. E. Scuseria, M. A. Robb, J. R. Cheeseman, V. G. Zakrzewski, J. A. Montgomery, Jr., R. E. Stratmann, J. C. Burant, S. Dapprich, J. M. Millam, A. D. Daniels, K. N. Kudin, M. C. Strain, O. Farkas, J. Tomasi, V. Barone, M. Cossi, R. Cammi, B. Mennucci, C. Pomelli, C. Adamo, S. Clifford, J. Ochterski, G. A. Petersson, P. Y. Ayala, Q. Cui, K. Morokuma, D. K. Malick, A. D. Rabuck, K. Raghavachari, J. B. Foresman, J. Cioslowski, J. V. Ortiz, A. G. Baboul, B. B. Stefanov, G. Liu, A. Liashenko, P. Piskorz, I. Komaromi, R. Gomperts, R. L. Martin, D. J. Fox, T. Keith, M. A. Al-Laham, C. Y. Peng, A. Nanayakkara, C. Gonzalez, M. Challacombe, P. M. W. Gill, B. Johnson, W. Chen, M. W. Wong, J. L. Andres, C. Gonzalez, M. Head-Gordon, E. S. Replogle, and J. A. Pople, Gaussian, Inc., Pittsburgh PA, 1998.

[22] T. Steiner, *Angew. Chem. Int. Ed.*, **41**, 48 (2002).

Chapter 5

Nitric Acid Dihydrates

5.1 Introduction

Nitric acid (HNO_3) and hydrates of nitric acid are ubiquitous and are used or produced in many processes. As one of the major components of polar stratospheric clouds (PSCs), nitric acid is the focus of much research. During the polar winter when PSCs freeze a deep hole in stratospheric ozone develops. It has been hypothesised that PSCs are responsible for ozone depletion, and the hydrates of nitric acid have been identified as possible catalysts[1]. Previous studies to investigate the catalytic pathway have only considered the hydrate crystal structures that form under ambient pressure conditions.[2,3] By applying pressure, the structural behaviour of a material can be systematically investigated, and any subsequent new phases obtained can be identified and characterised by diffraction methods.

Several studies have been conducted on the behaviour of a number of nitric acid hydrates, their phase diagrams and the crystalline structures of their different solid phases[4,5]. This chapter reports how high-pressure X-ray crystallography and quantum mechanical calculations can be combined to complete a structural investigation. In the previous chapter[6] nitric acid monohydrates (NAM) were explored. In this paper we now turn to the more complex case of nitric acid dihydrate (NAD). Of the two, NAD is the more complicated structure to generate, requiring thermal treatment to obtain a pure phase.

The X-ray structure of the nitric acid dihydrate has been more recently reported than that of the monohydrate analogue. To date two phases at ambient pressure have been described by Lebrun *et al.*[4,5] Central to the crystallography is the geometry of the $[H_5O_2]^+$ cation (known in the literature as the Zundel complex[7] or dihydronium ion). Dai *et al.*[8] reported a recent theoretical study which found a C_2-symmetry global minimum structure for this complex [Figure 5.1(a), labelled type 1]. In the two ambient-pressure crystal structures reported for NAD a further two conformations, also with C_2 symmetry, are observed [Figures 5.1(b) and 1(c), labelled type 2 and 3, respectively].

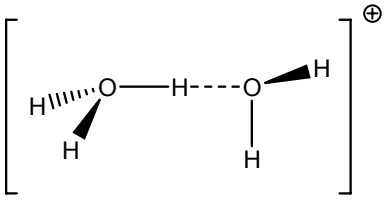

(a)

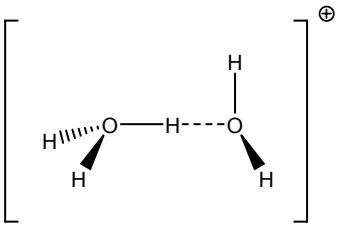

(b)

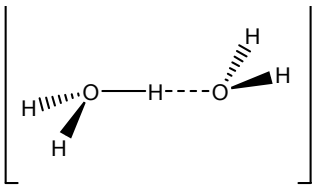

(c)

Figure 5.1 The three conformations of $[H_5O_2]^+$, (a) type 1, (b) type 2 and (c) type 3.

The low-temperature (200 K) ambient pressure (phase I) structure ($P2_1/n$) can be described as non-interacting bilayers of NAD units. An extensive network of hydrogen bonding makes up each of the monolayers, which are in turn connected through a longer hydrogen bond originating from an H_2O molecule (see Figure 5.2). Two forms of the dihydronium ion are present in this structure: type 2 cations are bonded solely in the monolayers, and type 1 are responsible for the bonding between the monolayers (see Figure 5.2).

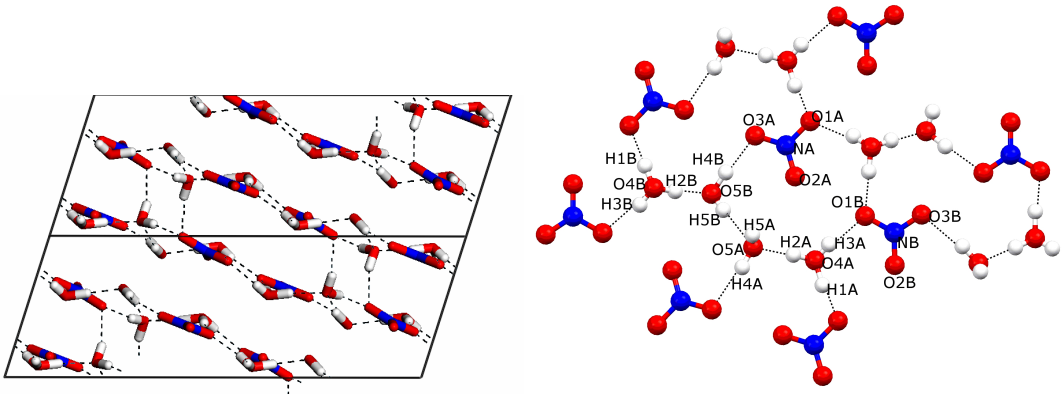

Figure 5.2 Crystal structure of phase I NAD (left) and connectivity map (right).

Slowly raising the temperature to 225 K generates a new polymorph of NAD. The shape of the unit cell has altered such that the longest crystallographic axis has changed from 'a' (phase I) to 'b' (phase II); a volume increase of 1% has also occurred upon temperature increase. The crystal structure of phase II has at least one hydrogen bond along each of the crystallographic axes. This polymorph crystallises in the same space group as phase I ($P2_1/n$) and a similar H-bonding motif can be observed, except that all layers are now held together by hydrogen bonds originating from the water molecules (four per unit cell). Once again, type 2 dihydronium ions form hydrogen bonds solely in the monolayers. However, in this phase it is type 3 ions which are responsible for the interactions between the layers (see Figure 5.3).

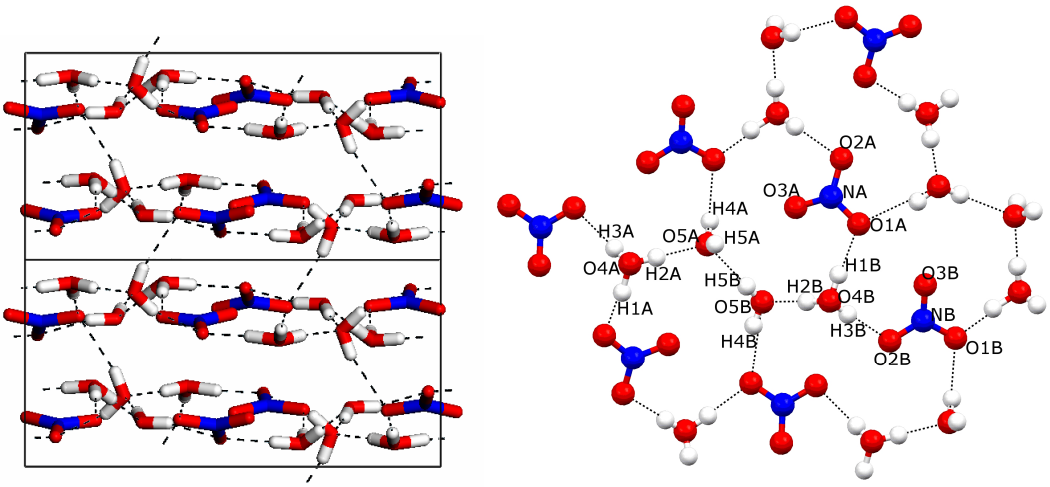

Figure 5.3 The crystal structure (left) and layer system (right) adopted by phase II of phase II NAD.

A number of computational and experimental studies on NAD have been published. Escribano[9] and Fernández[10] initially studied a gas-phase structure (*i.e.* isolated cluster) and found (at cc-pVTZ, B3LYP) the $HNO_3.2H_2O$ moiety to be of lower energy, compared to the ionic form $[NO_3]^-.[H_3O]^+.H_2O$. This study was followed by simulations using localised/pseudopotential basis sets with density functional theory (DFT) and periodic boundary conditions, which showed that in the solid phase $[NO_3]^-.[H_3O]^+.H_2O$ was the more stable structure. Both studies produced calculated vibrational spectra. Comparison with experiment[11] shows that the gas-phase calculations are not an appropriate representation for solid-state NAD, as they overestimate some modes by *ca.* 500 cm^{-1}. This is to be expected as large-amplitude, strongly anharmonic vibrations are misrepresented by the harmonic approximation, coupled to the fact that the gas-phase cluster is, in any case, a poor representation of the solid. Calculations performed with periodic boundary conditions fared much better, accurately reproducing the majority of vibrations to within a few cm^{-1}. However, some vibrations appear to be misrepresented, with for example the $[H_3O]^+$ symmetric stretch experimentally reported[12] to be in the region of 2714 cm^{-1} but calculated to be 2982-3017cm^{-1}, and no frequencies are calculated less than 1000 cm^{-1}. The clear improvement can be attributed to the superior model, as the periodic boundary conditions better reflect the repeating unit of the crystal. However, as the

vibrational frequencies were based on atomic Cartesian displacements (i.e. a harmonic oscillator), there is still room for improvement.

In the NAD crystal structure proton transfer occurs from the nitric acid to one of the water molecules, thus creating a unit cell containing $[NO_3]^-$, $[H_3O]^+$ and H_2O. Identifying the oxonium anion and water molecule sites in a high-pressure X-ray diffraction experiment is a considerable challenge. The sample is mounted in a diamond-anvil pressure cell, the nature of which restricts the volume of reciprocal space that can be accessed. The data set is not only more restricted than that collected from a conventional ambient-pressure study, but the intensity statistics of the reflections are also generally poorer. Consequently, the hydrogen atom positions are usually not determined in the crystal structures. DFT modelling can, however, be applied to complete the structure. Whilst Monte Carlo (MC) simulations are often applied in similar situations, the partially complete structure offered by experiment allows more computationally intense simulations to be used. Specific to this case, standard (i.e. modelling based on classical physics) modelling techniques can prove inaccurate when studying the protonated water dimer ion $[H_5O_2]^+$.

Completing the structure computationally is essentially a straightforward task: the unit-cell parameters and heavy-atom positions are supplied by experiment and the input model completed with approximate hydrogen-atom positions. The crystal structure is then optimised quantum mechanically in order to find the lowest energy atomic arrangement. Treating structures in this manner can create a problem, in that the geometry optimisation algorithm will only minimise the structure to the nearest local energy well, and there is no guarantee that this minimum represents the lowest energy structure on the potential-energy surface. Through our earlier study of nitric acid monohydrate at high pressure, we developed a computational procedure involving molecular dynamics (MD) calculations to probe the local energy surface more fully, and thus raise confidence levels on the hydrogen atom positions obtained.[5] Whilst this method successfully obtained complete structures for three different polymorphic phases of nitric acid monohydrate, the dihydrate derivative is a much more challenging case. In addition to the problem of identifying the $[H_3O]^+$

and H_2O sites, there exists the possibility that proton transfer can occur between these two molecules. The protonated water dimer $[H_5O_2]^+$ has been extensively studied due to its pivotal role in proton transfer in aqueous solutions[13] and so-called water wires[14]. However, this interesting ion presents several problems when studied from a theoretical perspective: a large flat potential-energy surface presents convergence issues, and large-amplitude, strongly anharmonic vibrations mean the harmonic approximation will not accurately represent the vibrational modes. Finally, the possibilities for low-energy rearrangement pathways generate multiple conformer issues. In our calculations we are able to sample the flat nature of the minimum by performing MD simulations, thereby allowing more of the potential-energy surface to be taken into account than would be possible by geometry optimisation alone, and would also allow any structural rearrangements due to skipping into other nearby energy wells to be observed. In addition, the vibrational frequencies we extract from our MD simulations are automatically corrected for anharmonic effects. Finally, we can run a series of single-point energies along a given trajectory to explore and visualise the potential-energy surface. Our methods of computational analysis are therefore ideally suited to allow meaningful study of the $[H_5O_2]^+$ ion within the crystal lattice.

In this chapter we report on *ab-initio* calculations on the previously known ambient-pressure polymorphs of nitric acid dihydrate. Also reported is a new phase recorded using high-pressure crystallographic techniques. The initial structure was obtained using single-crystal X-ray diffraction (3.8 GPa), with quantum mechanical calculations (plane-wave density functional theory, PW-DFT) then being employed to complete the partial experimental structure, thus allowing the hydrogen-atom positions to be located with a much greater degree of confidence. This was then followed by a high-pressure neutron diffraction experiment on the perdeuterated analogue system, thus allowing the validity of our computational model to be fully assessed. We also report the calculated vibrational spectra for the different structures studied.

5.2 Experimental and Computation

5.2.1 High-Pressure X-ray Diffraction

The crystals were grown by loading and pressurising a 68% (by weight) aqueous solution of nitric acid in a Merrill and Bassett diamond-anvil cell[15] that had been equipped with 600 μm culet diamonds and a tungsten gasket. A 68 wt% solution represents a HNO_3:H_2O ratio of 1:~1.65 indicating that dihydrate crystallises preferentially as single crystals over monohydrates and trihydrates. Some polycrystalline material was also present presumably due to the 1:1 monohydrate. The HNO_3 : H_2O ratio is of little significance for generation of phase III NAD. Subsequent experiments have found that ratios favouring a monohydrate crystallise as mixed dihydrate when under pressure . The gasket had been pre-indented to a thickness of 100 μm and had a 200 μm hole drilled through it. After the nucleation of several crystallites, the temperature was cycled close to the melting curve in order to reduce the number of crystallites, in a manner similar to that of Vos et al.[16] Finally, a single crystal was obtained at a pressure of 3.8 GPa. Subsequent pressure increases yielded the high-pressure phase of NAD.

The setting angles of strong reflections were determined on an Enraf-Nonius CAD4 diffractometer equipped with a Mo X-ray tube. Following initial indexing, a least squares fit yielded orthorhombic unit cell parameters, listed in Table 5.1. Intensity data were collected with the ω-scan method, at the position of least attenuation of the pressure cell, according to the fixed-ϕ technique. All accessible reflections were measured in the hemisphere $\pm h$, $\pm k$, $\pm l$, for 0 $Å^{-1}$ < $\sin\theta/\lambda$ < 0.71 $Å^{-1}$. The intensities were corrected for absorption, averaged, and then used for structure solution by direct methods.

	phase I		phase II		phase III			
	exp	calc	exp	calc	X-ray	calc (α)	calc (β)	Neutron
Space group	$p2_1/n$	$p2_1/n$	$P2_1/n$	$p2_1/n$	$p2_12_12_1$	p1	p1	$p2_12_12_1$
a (Å)	17.509(3)	17.431	9.674(3)	9.683	9.391(7)	9.483	9.458	9.4573(15)
b (Å)	7.619(4)	7.660	12.920(4)	12.944	3.127(2)	6.453[a]	6.518[a]	3.1776(3)
c (Å)	6.253(3)	6.382	6.484(3)	6.563	11.253(9)	11.294	11.211	11.3124(18)
A=γ	90	90	90	90	90	90	90	90
β	107.5(3)	108.63	97.71(3)	97.71	90	90	90	90
Volume ($Å^3$)	796(2)	807.54	803(1)	815.88	330.5(4)	691.2	694.3	340.0(9)
Z	8	8	8	8	4	8	8	4

Table 5.1 Crystallographic data for nitric acid dehydrate at elevated pressure.

The systematic absences for phase III NAD were consistent with the $P2_12_12_1$ space group, and an initial trial solution in this symmetry was found to be acceptable. The final structural model was refined using the CRYSTALS suite of programs[17] and the structural parameters from the various fits, along with the refinement statistics, are listed in Table 5.1. The data and crystal quality were sufficient to allow the displacement parameters to be refined anisotropically.

5.2.2 Computational methods

Equilibrium structures for the nitric acid dihydrate series were obtained using the VASP 4.4 simulation package[18] according to the following procedure. Initial geometries and space-group symmetry constraints were taken from experiment. In the case of unlocated hydrogen atoms (i.e. in the high-pressure phase III structure), nominal positions were selected based on a close inspection of the heavy atom positions and assuming pseudo-D_{3h} and C_{2v} structures for the $[H_3O]^+$ ion and H_2O molecule, respectively. A set of atomic position optimisations was performed initially so that a favourable hydrogen bonding network would be in place before any volume change was permitted. This was then followed by a series of single-point energy calculations where the lattice constants (multipliers for the cell vectors) were varied, thus establishing the volumes of the unit cells that gave rise to the lowest energies. All subsequent optimisations were then held at these fixed volumes. The atomic positions and lattice parameters were then optimised on alternate cycles, until

convergence was achieved. Phase III NAD calculations were performed using two different models (in *P*1 symmetry using a 1 × 2 × 1 supercell), corresponding to the two possible likely geometries for the $[H_3O]^+$ ion and H_2O molecule. For all other phases a 1 × 1 × 1 (*i.e*. crystallographic) cell was used, and the appropriate symmetry constraints applied. Simulations were performed using a set of ultrasoft pseudopotentials[19] and plane waves expressed at an energy cut-off at 396 eV. The generalised gradient approximation (GGA) functional PW91[20] was used to model the exchange and correlation potentials, and the Brillouin zones sampled by one k-point at the gamma (Γ) position. Convergence criteria were set such that optimisation was achieved once forces reached less than 10^{-3} eV $Å^{-1}$ and SCF energy less than 10^{-4} eV. A series of single point energy calculations showed that PW energy cut-off and K-point sampling was sufficient.

The equilibrium structure work was then followed by a series of PW-DFT microcanonical (NVE) molecular dynamics calculations performed in the *P*1 space group, in order to search the potential-energy surface more completely, and to investigate the effects of temperature (*i.e.* free energy) on the resulting thermally averaged structures. This also offered the opportunity to extract solid-state vibrational frequencies from the simulation by Fourier transformation of the autocorrelation function of the calculated forces, with low-frequency noise subtracted from the resulting spectra using a Blackman windowing function[21]. Here, the basis set energy cut-off was lowered to 297 eV, and identical convergence criteria and k-point sampling as for the equilibrium calculations were used. With the equilibrium structures used as starting points, MD simulations were run using a time step of 0.7 fs, determined after careful consideration of the highest energy vibrational frequency for the system (the OH stretch). Confirmation of this time-step was obtained by analysis of the resulting conservation of free energy in the NVE ensemble. The first 0.14 ps of each simulation was discarded to allow the system to reach equilibrium; data were then collected over a further 0.7 ps. The temperatures for phase I, phase II and phase III averaged to 243 K, 220 K and 218 K, respectively. A second simulation was subsequently performed on the phase I structure with a lower average temperature of 77 K.

Scans of the potential-energy surfaces were obtained by taking the relevant O•••O vectors and assuming a minimum O-H distance (around 0.9 Å); the remaining length [r(O•••O) — 2r(O-H)] was divided into nine equal fractions. Initial scans were obtained from single-point energy calculations with the hydrogen positioned at each fraction along the O•••O vector (figure 5.6). This was then followed by a second scan where the atomic positions were allowed to relax, with the exception of the two bridging oxygen atoms, which were fixed at their equilibrium geometry positions.

5.2.3 High-Pressure Neutron Diffraction

High-pressure neutron powder diffraction data were collected for $DNO_3.(D_2O)_2$ using the PEARL/HiPr diffractometer[22, 23] at the UK spallation neutron source, ISIS, located at the CCLRC Rutherford Appleton Laboratory. A solution (~100 mm^3) of composition ~1:1 was added to a TiZr capsule gasket[24] filled with loosely packed powdered silica wool which was used to inhibit the formation of large crystallites. A small pellet of aluminium foil was also added to act a pressure marker. The resulting capsule assembly was then compressed within a type V3b Paris-Edinburgh (P-E) pressure cell[25, 26] equipped with standard single toroid anvils with cemented WC cores (Ni binder). The P-E cell ram pressure was monitored and controlled by means of a computer controlled hydraulic system. The experiment was conducted without the use of a pressure transmitting medium due to the chemically aggressive nature of the sample. The maximum useful pressure was therefore limited to ~4 GPa by the onset of diffraction peak broadening resulting from non-hydrostatic stress within the sample.

Time-of-flight (tof) neutron powder diffraction data suitable for structure refinement were obtained by electronically focussing the 1080 individual detector element spectra of the main PEARL/HiPr $2\theta=90^o$ detector bank. The summed pattern was then normalised with respect to the incident beam monitor and the scattering from a standard vanadium calibration sample. Lastly, the diffraction pattern intensities were corrected for the wavelength and scattering-angle dependence of the neutron attenuation by the P-E cell anvil (WC) and gasket (TiZr) materials.[27] (See

Figure 5.4 for powder diffraction pattern.) Typical data collection times were 6 hrs at full ISIS beam, which equates to an integrated proton current of ~1 mA.hr. Full-profile Rietveld refinements of the tof neutron powder diffraction patterns were carried out using the GSAS package[28]. Sample pressures were calculated from the refined Al lattice parameters and the known room-temperature equation of state[29].

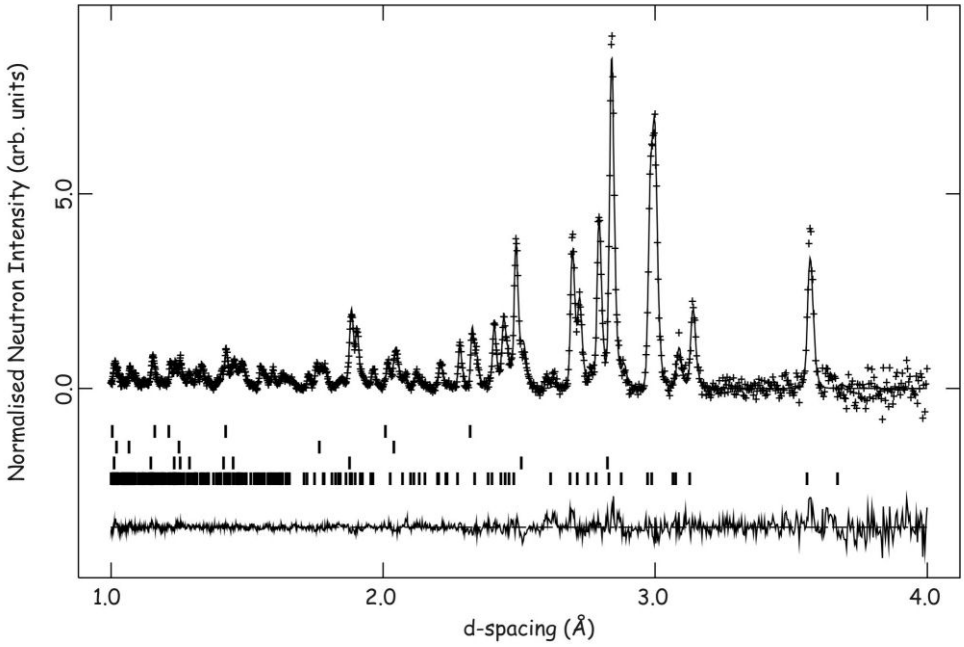

Figure 5.4 Powder diffraction pattern at 26 tonnes loading, with Al and silica wool.

5.3 Results and discussion

5.3.1 Phase I

Following a straightforward optimisation procedure the resulting (calculated) equilibrium structure compared well with that obtained experimentally (see Table 5.2), with the majority of heavy-atom distances reproduced to within 0.03 Å and a minimal volume increase (1.5%). As current DFT functionals cannot calculate dispersion forces (*i.e.* van der Waal interactions), some volume expansion is nearly always expected with in the GGA formulism. Visual superposition of the two structures confirmed that the calculated minimum corresponded well with that obtained from experiment. We can therefore conclude that the computational approach is capable of reproducing the key features of the nitric acid dihydrate structure.

	Phase I distances (Å)	
	exp	calc
N-O2 (A)	1.222(2)	1.244
N-O2 (B)	1.223(2)	1.240
N-O3 (A)	1.235(2)	1.265
N-O3 (B)	1.253(2)	1.277
N-O1 (A)	1.286(2)	1.301
N-O1 (B)	1.279(2)	1.301
O1A-O4A	2.550(2)	2.576
O1B-O4B	2.606(2)	2.630
O1A-O4B	2.628(2)	2.635
O1B-O4A	2.604(2)	2.592
O3A-O5B	2.768(2)	2.719
O5A-O3B(interplane)	2.940(2)	2.827
O3B-O5A	2.828(2)	2.778
O4A-O5A	2.559(2)	2.551
O4B-O5B	2.460(2)	2.422

Table 5.2 Phase I heavy-atom distances. For atom numbering see Figure 5.2.

In order to explore the potential energy surface (PES) further, a molecular dynamics (MD) calculation was then undertaken with the temperature equilibrated at approximately 200 K. This allowed direct visualisation of the flexibility of the system and any local wells to be accessed if the system has enough thermal energy to overcome any potential-energy barriers. Visualisation of the MD simulation showed that despite the lack of symmetry constraints a pseudo $P2_1/n$ space group was retained; furthermore the main geometrical features were still present. The hydrogen positions, however, showed some interesting behaviour. The type 1 $[H_5O_2]^+$ ion, [O4A-H2A-O5A, see Figure 5.1(a) and Figure 5.2] has O-H and H•••O distances of 0.93(2) and 1.64(2) Å, respectively, compared to calculated distances of 1.041 and 1.510 Å. This reflects the typical underestimation of O-H bond lengths by X-ray diffraction. The heavy-atom O•••O distances showed a much smaller deviation:

experiment 2.559(2) Å, calculated 2.560 Å. The hydrogen bonds linking $[H_3O]^+$ to H_2O, which are crystallographically in a layer {*i.e.* $[H_5O_2]^+$ type 2, O4B-H2B-O5B, see Figure 5.1(b) and Figure 5.2}, have O-H•••O distances of 0.91(3) and 1.55(3) Å respectively; in the calculated equilibrium geometry distances of 1.146 and 1.275 Å were determined. The heavy-atom structure remained close to that obtained experimentally, with the O4B•••O5B distance recorded at 2.460(2) and 2.422 Å by experiment and theory, respectively. This rather short heavy-atom bond distance, is indicative of a 'strong' hydrogen bond[30]. The shape of the PES for strong hydrogen bonds tends to be a broad flat single well, which potentially allows the phenomenon of proton migration to occur. When kinetic energy is added to the system (*i.e.* the MD simulation) we indeed observe the bridging hydrogens shuttling between O4B and O5B, and upon averaging remaining close to equidistant from both oxygens. After the hydrogen shuttling no further phase changes were observed from this simulation.

In order to explore the behaviour of the shuttling hydrogen bridge further, a second MD simulation was performed at a lower temperature (*ca.* 80 K). This calculation also sought to alleviate the concern that the equilibrium temperature for the phase I MD simulation was above that at which the phase II structure is observed experimentally. It was also believed that, should the temperature drop sufficiently, the mobility of the hydrogen atom would be reduced so that it associates with just one water molecule. To quantify the degree of proton shuttling observed in the two MD simulations, we define a parameter labelled δ, which denotes the deviation of the hydrogen atom from the centre of the O•••O vector. A value of zero indicates the bridging atom lies exactly in the middle of the bond, a negative value that the proton lies closer to O4B, positive O5B. A multiplicity plot of δ (expressed to two decimal places) averaged over all $[H_5O_2]^+$ type 2 ions in the unit cell for both MD runs is shown in Figure 5.5. As the temperature decreases it is clear that the hydrogen tends to locate more on one of the oxygen atoms (O4B) than the other. The equilibrium temperature for this simulation (*ca.* 80 K), is much lower than the conditions under which the phase was observed experimentally (225 K). Note, however, that even at the lower temperature the hydrogen does show some propensity to shuttle. The fact

that this was not observed experimentally is not surprising. The hydrogen atom is difficult to observe experimentally using X-ray diffraction, so in all likelihood a variable-temperature neutron diffraction study would be required to enable the temperature evolution of the hydrogen-atom position to be fully observed.

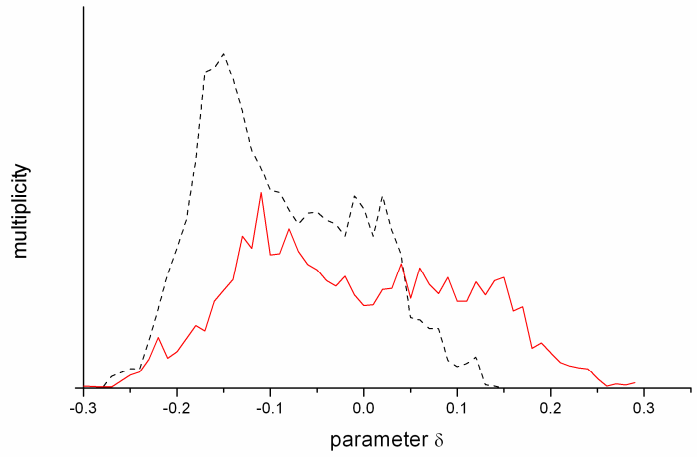

Figure 5.5 δ parameter plots. A negative value represents the bridging hydrogen lying closer to O4B, positive to O5B. Solid line represents high-temperature (243 K) MD, dashed line represents the low-temperature MD (77 K).

To visualise the nature of the potential-energy well for this O•••H•••O type 2 interaction PES scans were performed. The bridging hydrogen atom was transported along the O•••O vector in a set of nine increments from an initial O(4B)-H distance of 0.882 to an H•••O(5B) distance of 0.882 Å, assuming a linear OHO moiety. Initially the PES was generated from a series of single-point energy calculations, with all other atoms fixed at the equilibrium geometry. The results are presented in Figure 5.6. This was then followed with a second PES scan where all atoms (except the oxygen and hydrogen atoms directly involved in the short hydrogen bond) were allowed to optimise, allowing a mode softening to occur with the general shape of the PES remaining. This approximation is a rather crude one, (a more accurate PES could be obtained from a multidimensional parameter scan, where the OH distance is varied with the OHO angle and the O•••O vector, but the large number of steps required renders this calculation impractical). Since the general shape of the PES remained unchanged by these, more elaborate, calculations, they were not pursued

beyond that of a test on phase I type 1, which is not recorded in figure 5.6. The general shape of the PES can be observed and some explanation can be inferred as to why the phase I type 2 dihydronium ion conformation exhibits proton shuttling while the other conformations do not. Although the potential well around H2B showed the traits indicative of a shuttling hydrogen (large flat minimum), other potential surfaces appeared to be tilted, so as to favour a single hydrogen site. However, it must be noted that the potential-energy surfaces we calculate are derived from pure DFT calculations, and as such are expected to underestimate any barrier heights which may be present. (Indeed specific to this work is the study by S. Sadhukhan *et al.*[31] on the $[H_5O_2]^+$ cation which showed that the pure DFT functionals BLYP and PBE underestimate a gas-phase barrier height by up to 12 kJ mol^{-1}.) The issue of whether or not the shuttling phenomenon we observe in our MD simulation of the phase I structure of NAD is a genuine or artificial effect could be resolved by neutron diffraction, and this is work we will undertake shortly.

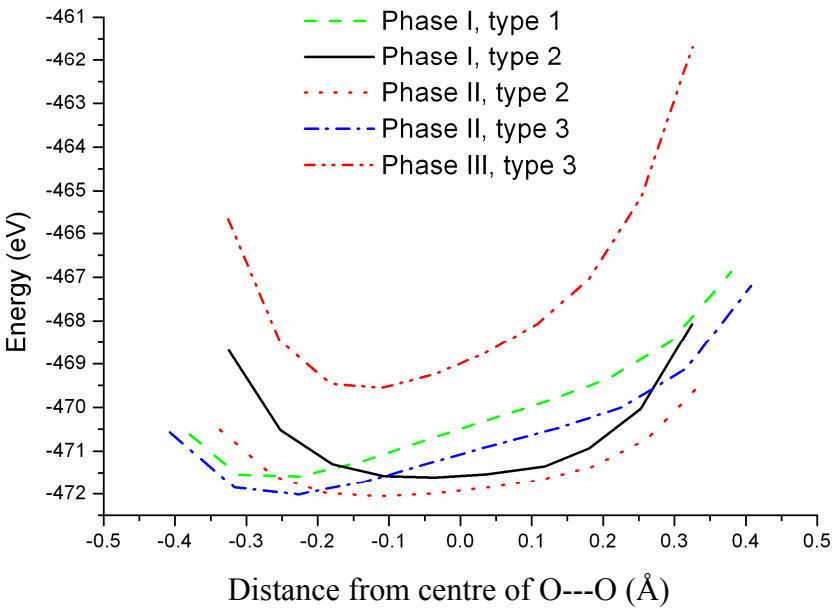

Figure 5.6 Single-point energy potential-energy surfaces. Phase I type 2 is the only conformation of the $[H_5O_2]^+$ ion that exhibits proton shuttling behaviour.

From the MD simulation a predicted vibrational spectrum may be produced, based on an autocorrelation of the forces obtained at each step. Whilst formal identification of each mode is not straightforward, as with normal mode analysis, performing the Fourier transform for selected atoms allows us to block out regions of the spectra for the different elements present. Hence vibrations involving the hydrogen atoms can be observed occurring at 2450-3610 cm^{-1}, whilst vibrations due to nitrogen are located between 650 and 1400 cm^{-1} and oxygen vibrations occur across the full range of the spectrum. The predicted vibrational spectra of NAD I (Figure 5.7) repeats many of the details shown in the experimental spectra, with broad intensities roughly where broad intensities are expected. As with all reported spectra in this chapter peak intensities do not translate to spectral intensities (i.e. are not weight averaged). It is worthy of note that obtaining experimental solid-state spectra of the hydrated nitric acid species is no simple matter as all the separate hydrate species are likely to be present. However, with the aid of X-ray crystallography, Tizek *et al.* are confident in their reported IR spectral assignment. With the exception of the $[NO_3]^-$ symmetic stretch (930 cm^{-1}), which is not IR active (and hence not present on the experimental spectrum), the predicted and experimental spectra show good correlation.

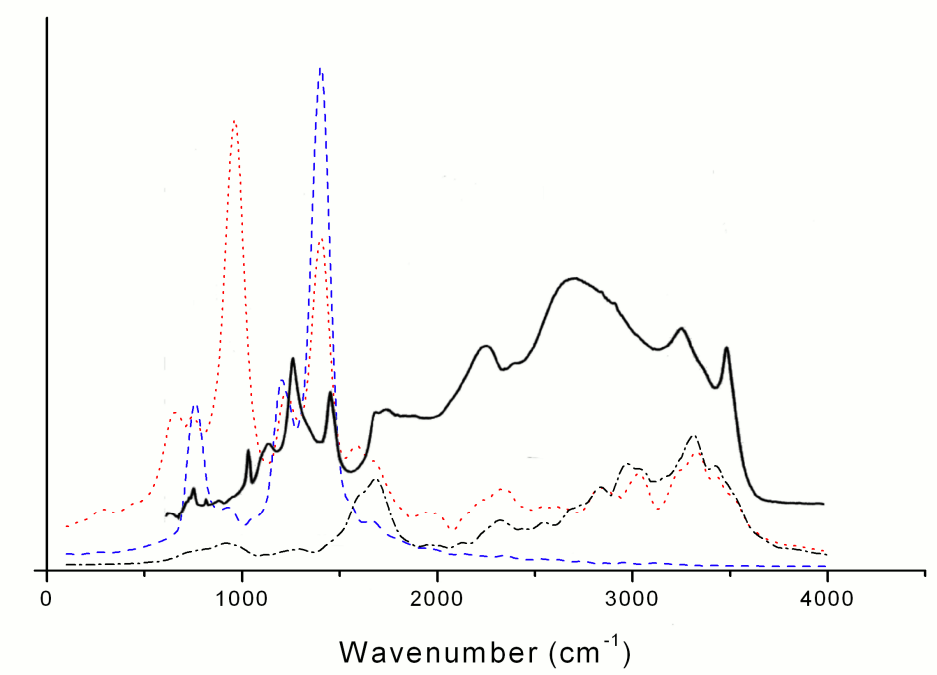

Figure 5.7 Vibrational spectra of NAD I, oxygen vibrations dotted, nitrogen vibrations dashed, hydrogen vibrations dot dashed. An experimental IR comparison[13] is included as a solid line.

5.3.2 Phase II (225 K)

The experimental study of this phase also reported all atomic positions with a high degree of accuracy, which again allowed us to check the quality of our simulations carefully. As with the phase I structure, the optimisation procedure was straightforward. The main structural features were retained (Table 5.3), indicating that the computational approach used to model this system was appropriate and could be extended to the work at high pressure, where much less of the structure is known from our X-ray diffraction measurements. To search for possible similar proton migrating phenomena as occurred in phase I, and to correct for possible problems originating from the trough-like nature of the PES, a full MD simulation was performed, allowing a complete assessment of structural changes resulting from an increase in temperature.

	Phase II distances (Å)	
	exp	calc
N-O2 (A)	1.214(4)	1.239
N-O2 (B)	1.227(4)	1.234
N-O3 (A)	1.265(4)	1.265
N-O3 (B)	1.246(4)	1.288
N-O1 (A)	1.263(4)	1.287
N-O1 (B)	1.278(4)	1.277
O1A-O4B	2.640(4)	2.633
O1B-O4A	2.521(4)	2.581
O1A-O5B	2.832(4)	2.809
O1B-O5A	2.827(4)	2.789
O2A-O4A	2.626(4)	2.601
O2B-O4B	2.663(4)	2.623
O5A-O2A(interplane)	2.884(4)	2.792
O4A-O5A	2.553(4)	2.547
O4B-O5B	2.459(4)	2.466

Table 5.3 Phase II heavy-atom distances. For atom numbering see Figure 5.3.

The two $[H_5O_2]^+$ geometries present in this structure are of types 2 and 3, it differs from phase I, which contains type 2 and the lowest-energy dihydronium conformation type 1. Interestingly, although this higher temperature polymorph contains the same dihydronium unit that displayed proton shuttling in the phase I structure (type 2), no migratory effect was observed in our molecular dynamics simulation. Performing a PES scan similar to that of phase I (*i.e*. stepping the *r*O-H distance from 0.919 to 1.527 Å in nine increment steps, with all other atoms fixed at equilibrium positions) produces a similarly shaped potential-energy well as observed for the type 2 unit in phase I, but the bottom of the well is slightly tilted, thus favouring a single hydrogen location (Figure 5.6).

The MD-extracted vibrational spectrum (Figure 5.8) repeats many of the characteristics of the previous phase; a broad O-H region, sharp O-N vibrations. The

broad nature of many of the vibrations makes characterisation difficult. Comparing the experimental spectra with that calculated, indicates many similarities; there are broad absorptions from approximately 3500 cm^{-1} to 1700 cm^{-1} and sharper absorptions below 1700 cm^{-1}. The accuracy of the simulation adds credence to the ability of PW-DFT calculations to model this system.

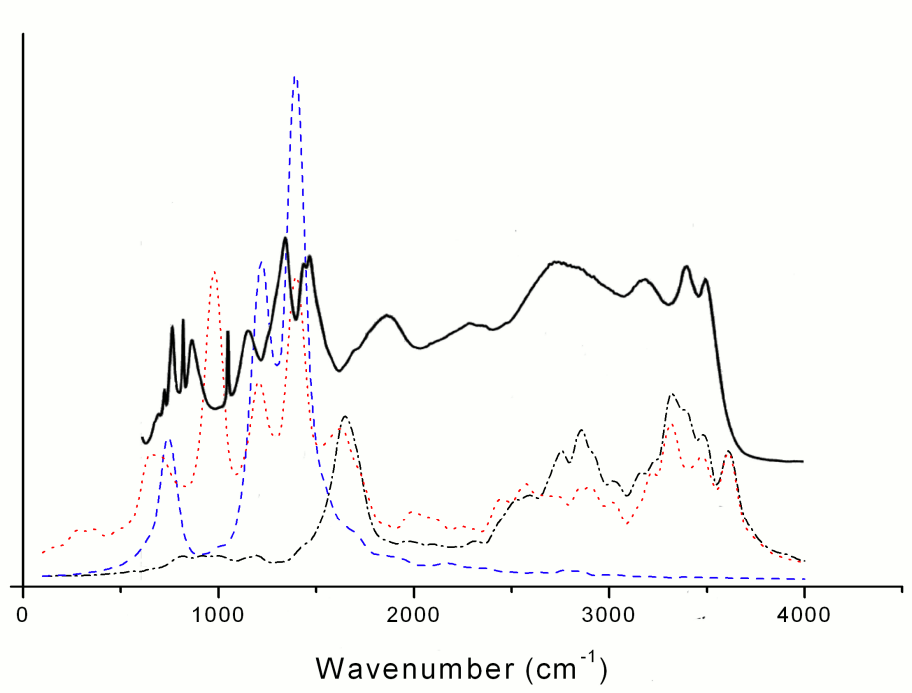

Figure 5.8 Vibrational spectra of NAD phase II, oxygen vibrations dotted, nitrogen vibrations dashed, hydrogen vibrations dot dashed. An experimental IR comparison[13] is included as a solid line.

From our modelling studies of the ambient-pressure phases of nitric acid dihydrate we conclude that PW-DFT has successfully reproduced the key geometric features of the two previously known phases. We now turn to the high-pressure structure, where our initial experimental measurements were unable to locate the positions of the hydrogen atoms. As a consequence, the nature of the dihydronium ion is undetermined for this phase, presenting an interesting modelling challenge for this previously unknown structure.

5.3.3 Phase III (3.8 GPa, 273 K)

5.3.3.1 High-pressure X-ray Diffraction

The heavy-atom structure obtained by single-crystal X-ray diffraction was found to be of orthorhombic $P2_12_12_1$ symmetry with a unit cell volume less than half the size of the ambient-pressure cells (see Table 5.4). The asymmetric unit of phase III NAD contains one $[NO_3]^-$ and one $[H_5O_2]^+$ ion, unlike the previous two phases that contained two $[NO_3]^-$ and two $[H_5O_2]^+$ ions. As this initial X-ray study could not locate hydrogen-atom positions, we are unable to distinguish between the $[H_3O]^+$ and H_2O sites, and also whether the dihydronium unit is of type 1, 2, or 3. Input was therefore required from quantum mechanical calculations and/or neutron diffraction to complete the structure. In this study we were fortunate to be able to do both. We undertook a computational investigation first in order to complete the X-ray diffraction refinement; this in turn provided a complete set of atomic positions as a starting model for the neutron diffraction study. A successful refinement of the neutron diffraction data would therefore validate our computational result.

	Phase III distances (Å)		
	X-ray	calculated	Neutron
N-O2	1.252(13)	1.268	1.245(9)
N-O3	1.252(12)	1.248	1.250(9)
N-O1	1.240(18)	1.288	1.240(9)
O1-O5	2.692(15)	2.666	2.717(22)
O1-O4	2.576(11)	2.592	2.623(22)
O2-O4	2.664(18)	2.608	2.725(21)
O3-O5	2.924(14)	2.951	2.925(23)
O4-O5	2.448(15)	2.451	2.370(21)
O5 – D3	-	1.367	1.377(21)
O1 – D4	-	1.627	1.820(21)
O3 – D5	-	2.096	2.128(20)
O1 – D1	-	1.574	1.661(21)
O2 – D2	-	1.604	1.745(21)

Table 5.4. Phase III heavy-atom distances. For atom numbering see Figure 5.8.

5.3.3.2 Computation

The X-ray diffraction study provided a set of starting parameters for the unit cell and heavy-atoms positions. As the $[H_3O]^+$ and H_2O sites were indistinguishable from the experimental study, two models were constructed, labelled α and β, where the two sites were interchanged. The $[H_3O]^+$ ion was started from a planar, pseudo-D_{3h} geometry (to prevent artificially favouring a particular structure) and the H_2O molecule from pseudo-C_{2v} local symmetry. Initial geometry optimisations of both models, however, yielded poor results, with unreasonable lattice parameters and large heavy-atom displacements. Large displacements arise in systems where one axis is very different from the others, due to the relative pressures exerted on each axis (smaller area = higher pressure). This problem can be resolved by doubling up to a supercell along any small axis. Further calculations performed with 1×2×1 supercells helped stabilise both models, reducing heavy-atom displacements to acceptable levels, with the majority of heavy-atom distances reproduced to within

0.04 Å and minimal volume increases (4.6%) in both cases (Tables 5.4 and 5.5). Despite the removal of all symmetry constraints, the structure maintained a pseudo $P2_12_12_1$ space group throughout the simulation.

Pressure / GPa	3.8
Crystal system	Orthorhombic
Space Group	$P2_12_12_1$
No. reflections for cell	17
$2\theta_{max}(°)$	80
Z	4
Reflections collected	843
No. unique [R_{merge}]	394 [0.052]
No. $F>4\sigma(F)$	278
Parameters	25
R_1 [$F>4\sigma(F)$]	0.1151
wR_2 (F, all data)	0.0355
S	1.209
$\Delta\rho_{max}$ (e Å^{-3})	0.66
$\Delta\rho_{min}$ (e Å^{-3})	-0.42

Table 5.5 Experimental and calculated lattice parameters for the three phases of NAD.

[a] Note 1 × 2 × 1 simulation cell used for phase III structure.

The two models produced equilibrium geometries of similar energies (α= 469.77995 eV and β=469.77255 eV), but with non-identical structures, each corresponding to the initial dihydronium ion conformation. Both of these structures were studied with MD simulations, allowing the hydrogen to shuttle, and hence a possible transition between the two structures may be observed. Model β, however, showed instabilities in the MD simulation, with large unrealistic displacements in the nitrate ion positions. Model α, on the other hand, appeared to be much more robust. On this basis model β was eliminated as a possible geometry, and the coordinates obtained

for the optimised structure of model α (Figure 5.9) put forward as a starting model for the high-pressure neutron diffraction study refinement.

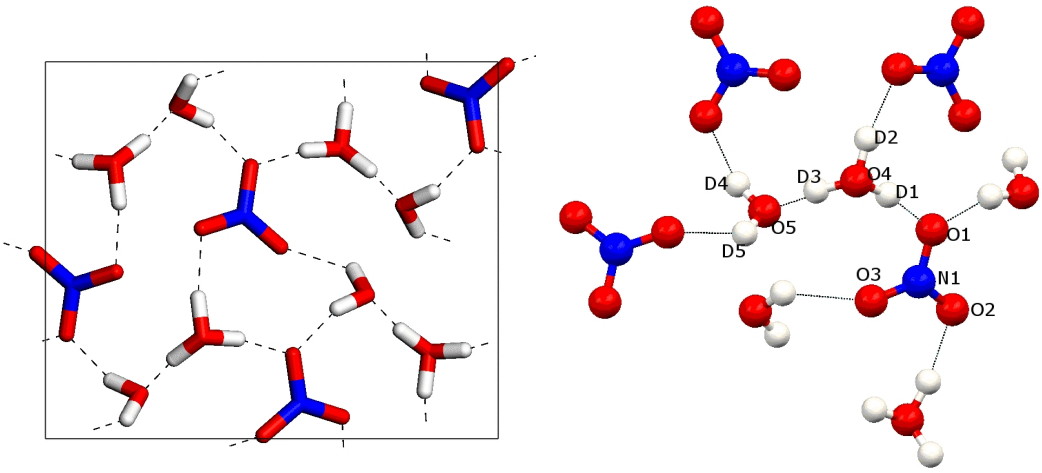

Figure 5.9 Crystal structure of NAD phase III (left) and connectivity map (right).

The dihydronium ion thus found in the simulation is of type 3 and shows no proton migration. A PES scan was performed to determine why this was, which indicated that the floor of the well appears to be tilted favouring just one hydrogen-atom location (see Figure 5.6). Hydrogen-atom migration therefore seems unlikely for this structure even at elevated temperatures.

The predicted vibrational spectra (Figure 5.10) displayed fewer, better defined peaks relative to phases I and II, which can be attributed to the smaller asymmetric unit of the phase III structure.

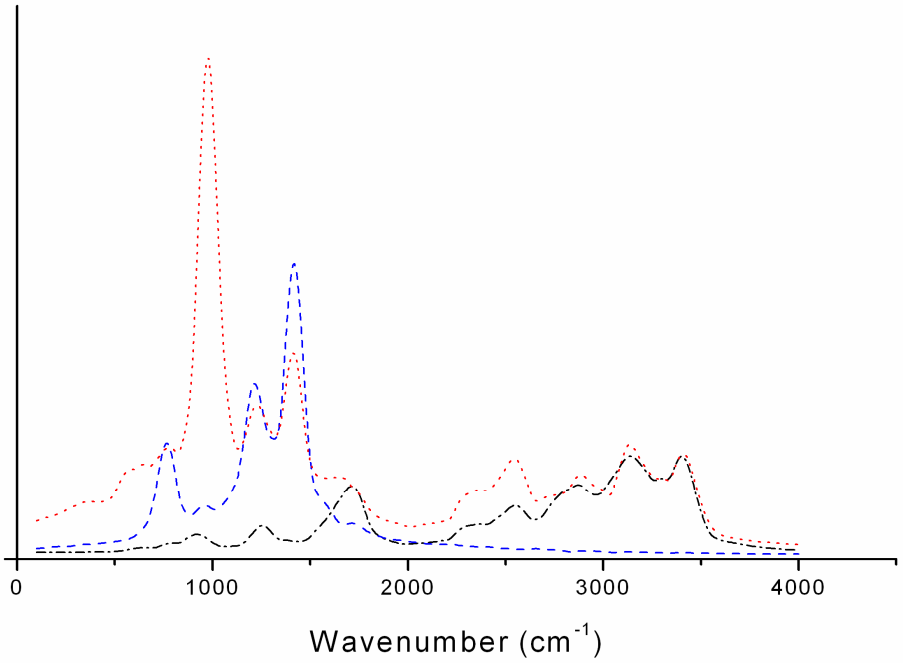

Figure 5.10 Vibrational spectra of high-pressure NAD phase III, oxygen vibrations dotted, nitrogen vibrations dashed, hydrogen vibrations dot dashed.

5.3.3.3 High-pressure Neutron Diffraction

Following the high-pressure neutron diffraction technique, phase III NAD was first observed at 1.33 GPa. Since simulations yielded promising results identifying hydrogen locations, the 0 K equilibrium structure was used as the model for refinement. Differences in pressure and the isotopic substitution can account for small differences but on the whole only minimal displacements are expected. The structure determined by neutron diffraction (Table 5.4) was remarkably close to that predicted by simulation, confirming the α model as the optimal structure.

5.4 Conclusions

Three nitric acid dihydrate species have been studied computationally. A new high-pressure phase was initially observed and characterised by X-ray diffraction and computational means, and the completed crystal structure proposed was later confirmed by neutron diffraction. The dihydronium ions present in each dihydrate are observed to form in three geometries. One of these – type 2 [Figure 5.1(b)] – shows the interesting feature of a shuttling hydrogen present in a short O•••O

linkage. This interesting phenomenon is easily overlooked experimentally, due to hydrogen having a minimal scattering density to diffract X-rays. Whilst the same conformation of the dihydronium ion is found on two other occasions (phases 1 and 2) the phenomenon of proton shuttling is observed in our MD simulations only once, indicating the sensitivity of the shuttling hydrogen to external potentials. Further work is required to examine this effect fully.

References

[1] M. J. Molina, T. –L. Tso, L. T. Molina, F. C. –Y. Wang, *Science,* **238,** 1253 (1987).

[2] G. Tóth, *J. Phys. Chem. A,* **101,** 8871, (1997).

[3] D. Salcedo, L. T. Molina, M. J. Molina, J. *Phys. Chem. A*, **105(9),** 1433 (2001).

[4] N. Lebrun, F. Mahe, J. Lamiot, M. Foulon, J. C. Petit, D. Prevost, *Acta Crystallogr.*, **B57,** 27 (2001).

[5] N. Lebrun, F. Mahe, J. Lamiot, M. Foulon, J. C. Petit, *Acta Crystallogr.*, **C57,** 1129 (2001).

[6] M. Walker, C. A. Morrison, D. R. Allan, *Phys. Rev. B,* **72,** 224106 (2005).

[7] G. Zundel, H. Metzger, *Z. Phys. Chem.*, **58,** 225, (1968).

[8] J. Dai, Z. Bačić, X. Huang, S. Carter, J. M. Bowman, *J. Chem. Phys.*, **119,** 13 (2003).

[9] R. Escribano, M. Couceiro, P. C. Gómez, E. Carrasco, M. A. Moreno, V. J. Herrero, *J. Phys. Chem. A*, **107,** 651 (2003).

[10] D. Fernández, V. Botella, V. J. Herrero, R. Escribano, *Phys. Chem. B*, **107,** 10608 (2003).

[11] H. Tizek, E. Knözinger, H. Grothe, *phys. Chem. Chem. Phys.,* **4,** 5128 (2002)

[12] H. Grothe, C. E. Lund Myhre, H. Tizek, *vib. Spec.* **34,** 55 (2004).

[13] N. Agmon, *J. Mol. Liq.*, **73-74**, 513 (1997).

[14] N. Agmon, *Chem. Phys. Lett.,* **244,** 456 (1995).

[15] L. Merrill, W. A. Bassett, *Rev. Sci. Instrum.,* **45,** 290 (1974).

[16] W. L. Vos, L. W. Finger, R. J. Hemley, *Nature (London)*, **358,** 46 (1992).

[17] P. W. Betteridge, J. R. Carruthers, R. I. Cooper, K. Prout, D. J. Watkin, *J. Appl. Cryst.,* **36**, 1487 (2003).

[18] G. Kresse, J. Furthmueller, *Comp. Matter. Sci.*, **6,** 15 (1996).

[19] D. Vanderbilt, *Phys. Rev. B*, **41,** 7892 (1990).

[20] J. P. Perdew, J. A. Chevary, S. H. Vosko, K. A. Jackson, D. J. Singh, C. Fiolhais, *Phys. Rev. B,* **46**, 5571 (1992).

[21] In-house code following accepted literature practise (Allen, M. P.; Tildesley, D. J. Computer simulation of liquids)

[22] PEARL - Pressure and Engineering Research Line. ISIS 97 - ISIS Facility Annual Report 1996-97, Rutherford Appleton Laboratory: 1997; Vol. RAL-TR-97-050, 28.

[23] Dedicated Facility for High Pressure Diffraction. ISIS 96 - ISIS Facility Annual Report 1995-96, Rutherford Appleton Laboratory: 1996; Vol. RAL-TR-96-050, 61.

[24] W. G. Marshall, D. J. Francis, *J. Appl. Cryst.*, **35**, 122 (2002).

[25] R. J. Nelmes, J. S. Loveday, R. M. Wilson, J. M. Besson, S. Klotz, G. Hamel, S. Hull, Proceedings of the Symposium on Time-of-Flight Diffraction at Pulsed Neutron Sources, J. D. Jorgensen, A. J. Schultz, *Eds. Amer Crystallographic Assoc: Buffalo,* **29,** 19 (1994).

[26] J. M. Besson, R. J. Nelmes, G. Hamel, J. S. Loveday, G. Weill, S. Hull, *Physica B*, **180**, (PtB), 907 (1992).

[27] W. G. Marshall, unpublished;

[28] A. C. Larson, R. B. Von Dreele, *Los Alamos National Laboratory Report LAUR* 2000, 86.

[29] R. G. Greene, H. Luo, A. L. Ruoff, *Phys. Rev. Lett.*, **73,** 2075 (1994).

[30] G. A. Jeffrey, An Introduction to Hydrogen Bonding, Oxford University Press, Oxford, 1997.

[31] S. Sadhukhan, D. Muñoz, C. Adamo, G. E. Scuseria, *Chem. Phys. Lett.,* **306,** 83, (1999).

Chapter 6
Completing the structure: supplementing limited experimental diffraction data with theory.

6.1 Introduction

Studying the behaviour of matter at high pressure is of paramount importance and finds many applications ranging from helping to explain the presence of life deep beneath the sea, to the likely structure of solids on other planets. Other applications include the formation of polymorphs in the pharmaceutical industry, where the unexpected formation of a new crystal packing arrangement can be a major chemical processing set-back which may incur considerable financial cost or even violate existing patent protections.

From a structural chemistry aspect, the method of choice for studying the high-pressure behaviour of crystalline materials is the diamond anvil compression cell (DAC),[1] as it is a small, simple device that is easily handled on a standard X-ray diffractometer. The method does have major limitations, however, in that a large percentage (typically 60%) of the diffraction data cannot be collected due to the physical presence of the DAC obscuring the wide-angle reflections, and the data that can be collected typically have poorer intensity statistics. As a consequence, high-pressure crystallography often generates refined structures without hydrogen-atom positions and the heavy-atom positions are often determined with lower precision compared to standard X-ray crystallographic studies. Definitive hydrogen-atom positions can of course be found experimentally via the collection of neutron diffraction data on the deuterated sample, but this makes the assumption that the deuterated structure is identical to that of the parent compound, which is not always the case.

Recent publications by us have demonstrated the use of ab initio modelling techniques to locate the hydrogen-atom positions[2, 3] thereby completing high-pressure structures without resorting to neutron diffraction experiments. The procedure is essentially straightforward: the unit cell parameters and heavy-atom positions are supplied by experiment and the input model completed with guessed hydrogen-atom positions. The crystal structure is then optimised quantum mechanically in order to find the lowest energy atomic arrangement. Whilst this approach does find an energy minimum there is no guarantee that it will be the global

one, in which the most thermodynamically stable structure is located. In order to achieve this, further steps must be taken. We demonstrated the application of molecular dynamics (MD) simulations to add energy to the system, thereby allowing it to cross some energy barriers to find the lowest point on the potential-energy surface (PES). Important to this chapter is the molecule hydroxylamine. The methodology presented in previous chapters failed to generate the correct experimental structure, so it is clear that a more exhaustive method is required. In cases where a definitive molecular connectivity cannot be inferred there is more opportunity for the simulations to settle on a non-global minimum. This paper attempts to address this point, and reports two proof-of-concept test studies where a Monte Carlo technique was use to generate initial hydrogen-atom geometries, each of which was then pursued to obtain the structure with the most thermodynamically favourable atom positions.

The basic principal behind Monte Carlo calculations is one of randomness. It has found application in a number of areas, including solving the self-consistent field equations, calculating electron correlation, structure optimisation and statistical studies to mention a few. In this work we have applied the Monte Carlo formalism to sample a larger area of the PES than could be obtained by the MD simulations alone. This is achieved by generating a large number of structures where the appropriate number of hydrogen atoms are connected at random positions to the heavy-atom structure, which, since it is known reliably by experiment, remains constant throughout all structures. We use two constraints in our otherwise random hydrogen atom placement, namely each H atom is placed 1 Å from its bonded heavy atom in a tetrahedral geometry. Whilst in reality these assumptions may not be perfectly true, holding parameters at these values allows more meaningful structures to be sampled initially; subsequent geometry optimisations are then run in the absence of any such constraints. It should be noted that our procedure was designed with simple molecules in mind where a tetrahedral geometry is likely; trigonal and linear geometries can be sampled from the optimisation steps. The higher co-ordinations (five, six, etc.) are not compatible with this code, but in principle there is no reason why they could not be programmed in a similar manner.

Following the random structure generation step, single-point energy (quantum mechanical) calculations can then be performed on each structure. Conceptually, should enough arrangements be sampled, one of them would be the energy minimum and hence the structure we are searching for. However, since the number of structures required to obtain the minimum in this way may be very large, a more efficient approach could be to perform geometry optimisations following the generation of each random structure. Since optimisations require many steps, tests are required to determine which method produces the most accurate results with greatest computational efficiency.

In this chapter we present our methodology for locating the hydrogen atoms in molecular crystalline materials based on a Monte Carlo random structure algorithm, followed by quantum mechanical geometry optimisations and molecular dynamics calculations. We illustrate our method with two test cases: acetic acid and hydroxylamine. Our input models relate to the known ambient-pressure polymorphs (i.e. the hydrogen atom positions are measurable by the experiment) and therefore act to validate our complete structures. Our goal is to demonstrate that it is possible to locate the light-atom positions using high-level computational modelling techniques, and thereby address the inherent limitations in solving high-pressure X-ray crystallography data sets.

6.2 Random structure generation: the theoretical basis

A methane molecule exemplifies locating the hydrogen atoms given one, two, three and four dependent points. To place all four hydrogen atoms one must first place one atom, and then add all further hydrogen atoms one at a time. This is based around the mathematical principle of two, three and four circles intersecting in space.

Given just a single carbon atom the hydrogen must be located on the surface of the sphere of radius r_i, as defined by equation 6.1:

$$r_i^2 = (x - x_i)^2 + (y - y_i)^2 + (z - z_i)^2 \qquad \textbf{equation 6.1}$$

where r_i is the radius of the sphere centred at (x_i, y_i, z_i).

Selecting random values of x, y and z that hold true to equation 6.1 determines the position of H1. To find H2 equation 6.1 must still hold, but H2 must also be located 109.5° from H1. Using the cosine rule a distance between H1 and H2 can be determined:

$$r_j^{\,2} = b^2 + c^2 - 2bc\cos(109.5°) \qquad \textbf{equation 6.2}$$

where b is the distance between C and H1, c is the distance between C and H2, and so r_j is the distance between H1 and H2. From r_j a sphere can be constructed, such that:

$$r_j^{\,2} = (x - x_j)^2 + (y - y_j)^2 + (z - z_j)^2 \qquad \textbf{equation 6.3}$$

where x_j, y_j and z_j are the coordinates of H1.

H2 must be located on the circle where the spheres (equation 6.1 and 6.3) meet, such that,

$$r_i^{\,2} - r_j^{\,2} = x_i^{\,2} - x_j^{\,2} + 2x(x_j - x_i) + y_i^{\,2} - y_j^{\,2} + 2y(y_j - y_i) + z_i^{\,2} - z_j^{\,2} + 2z(z_j - z_i)$$

equation 6.4

With re-centring and simple matrix rotations this circle can be reoriented to remove any z component, leaving

$$r_k^{\,2} = (x - x_k)^2 - (y - y_k)^2 \qquad \textbf{equation 6.5}$$

where

$r_k = r_j\sin(70.5°)$

$x_k = (x_j - x_i)\cos A + (y_j - y_i)\sin A$

$y_k = -(x_j - x_i)\sin A\cos B + (y_j - y_i)\cos A\cos B + (z_j - z_i)\sin B$

Where A is the angle between $\begin{pmatrix} x_j - x_i \\ y_j - y_i \end{pmatrix}$ and the y axis, and B the angle between the vector $\begin{pmatrix} x_j - x_i \\ z_j - z_i \end{pmatrix}$ and the z-axis. The z-coordinate is now a constant with respect to r_j, such that $z = (x_j - x_i)\sin B\sin A - (y_j - y_i)\sin B\cos A + (z_j - z_i)\cos B + r_j\cos(70.5°)$

and the hydrogen-atom coordinates can be found by selecting random values of x and y that are commensurate with equation 6.5.

To find the third and fourth hydrogen atoms an identical methodology can be followed: its position is where the circle (equation 6.5) meets the sphere (equation 6.6)

$$r_l^2 = (x - x_l)^2 + (y - y_l)^2 + (z - z_l)^2 \qquad \textbf{equation 6.6}$$

where r_l is the distance between H2 and H3 and x_l, y_l and z_l are the coordinates for H3.

The random number generator simply selects one of the two available positions. Note, to find the fourth hydrogen atom no random numbers are required, as simple trigonometry can find its location given the locations of the previous three atoms.

6.3 Experimental and Computational

6.3.1 Test cases

Our random-structure generation code and computational procedure was blind-tested against two test molecular crystals, to prove the procedure could successfully locate hydrogen atoms in experimentally accessible structures and to find the most efficient method of implementation.

6.3.1.1 Acetic acid (CH_3COOH)

The crystal structure of acetic acid was first reported by Jones & Templeton[4] minus the hydrogen atoms, and completed by Nahringbauer[5] and Jönsson[6] by an X-ray and neutron diffraction study, respectively. It is an ideal compound to start testing the methodology as it is a small hydrogen-bonded molecular system with a finite number of possible hydrogen geometries. The earlier experimental structure can be used to initialize the code; with no experimental hydrogen atoms the simulations can be performed without any bias towards a given structure. The results from these simulations can then be compared against those with experimental hydrogen data and the validity of the simulations graded.

Acetic acid crystallises in an orthorhombic $Pna2_1$ cell [a=13.32 (2), b=4.08 (1), c=5.77 (1) Å]. Jones & Templeton[4] suggested that the molecules form hydrogen-bonded chains interlinked with van der Waal interactions (Figure 6.1).

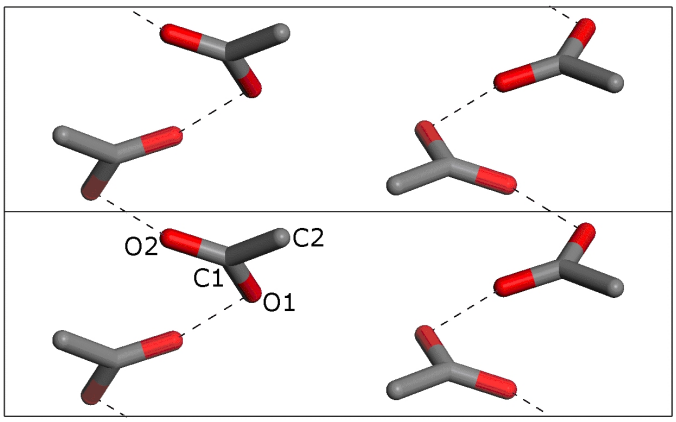

Figure 6.1 The acetic acid heavy-atom crystal structure as observed experimentally by Jones *et al.*[4]

The asymmetric unit was used to identify two possible hydrogen connectivities, which differed in the identity of the attached oxygen [O(1) or O(2); labelled acid 1 and acid 2, respectively]. Calculations were performed on an input bank of 40 possible structures (i.e. 20 random structures generated for each of the two different connectivities). This number of structures was used as more than 40 lead to large amounts of repetition in initial structures.

6.3.1.2 Hydroxylamine (NH_2OH)

The ambient-pressure structure of hydroxylamine has been the topic of some scientific debate. It was first reported by Meyers and Lipscomb[7], and as they could not locate the hydrogen-atom positions they offered three different structures as possible solutions. Recent crystallography experiments by Marshall[8] (neutron) and McGregor[9] (X-ray) successfully located the hydrogen atoms and hence can be used to verify our modelling work.

Hydroxylamine is a more rigorous test of our method due to the possible internal torsional twist of the -OH group with respect to NH_2. In order to assess this some preliminary isolated-molecule (Gaussian[10]) calculations were employed. The

energy required to rotate the -OH group between maximum and minimum positions on the potential-energy surface (PES) is 37 kJ mol^{-1}. As this energy penalty could feasibly be regained from hydrogen bonding and crystal packing we will therefore need to sample a large number of structures encompassing considerable geometric variation in our input bank. Another challenge offered from this test candidate is that the electron count of the -OH group is the same as for NH_2; there therefore exists the distinct possibility that the heavy-atom positions could be reversed during the X-ray solution. To this end we constructed two different structural models (type 1 and type2, see Figure 6.2) where the nitrogen and oxygen positions have been swapped over. In total 80 random structures were tested (40 from each model).

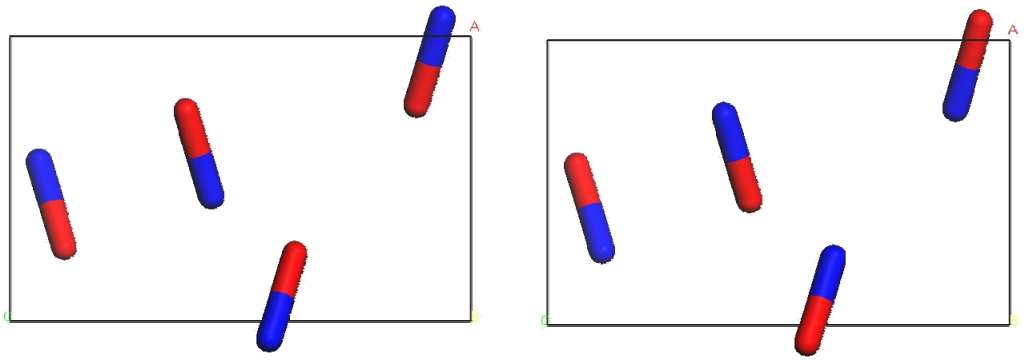

Figure 6.2 Heavy-atom configuration for type 1 structures (left) and type 2 structures (right).

6.3.2 Computational

Optimisations were performed using the VASP 4.4 simulation package[11] using a set of ultrasoft pseudopotentials[12]. Plane waves were expressed to a limit of 396 eV within the periodic boundary condition formulism. The generalised gradient approximation (GGA) functional PW91[13] was used to model the exchange and correlation potentials. For acetic acid the Brillouin zone was sampled by one k-point at the gamma (Γ) position; for the more challenging test candidate hydroxylamine a Monkhorst-Pack grid[14] of 3x3x2, corresponding to nine k-points, was employed. Convergence criteria were set such that optimisation was achieved once forces reached less than 10^{-3} eV $Å^{-1}$ and the values for self-consistent field (SCF) energies

varied by less than 10^{-4} eV on consecutive cycles. A series of single point energy calculations showed that PW energy cut-off and K-point sampling was sufficient.

After close examination of the optimisation calculations a number of structures which showed promising energies were used in a series of microcanonical (NVE) molecular dynamics calculations (performed in the P1 space group), in order to search the potential-energy surface (PES) more completely and to observe the effects of free energy on the structures. The basis set energy cutoff was lowered to 297 eV; all other convergence criteria and k-point sampling were identical to that used in the optimisations. The equilibrium structures were taken as starting points; each MD simulation was run using a 0.6 fs timestep, determined after careful consideration of the highest energy vibration. The simulations were allowed to accrue data over 0.9 ps, the first 0.12 ps of which were discarded to allow each system to achieve equilibrium.

The acetic acid MD simulations achieved an average temperature of *ca.* 225 K; further simulations at higher temperatures failed to reveal any further structures on the PES. Hydroxylamine MD simulations averaged temperatures of *ca.* 300 K. Higher temperature simulations failed to reveal any further structures.
Gas-phase calculations were performed using Gaussian 98[10] with a 6-311G* basis set and the hybrid DFT functional B3LYP[15]. A relaxed-PES scan was performed to rotate the H-O-N-H torsion angle through 180° (symmetry can account for the full 360°) to determine the energy barrier to internal rotation.

6.4 Results and discussion

6.4.1 Acetic Acid

Twenty structures for the acid models 1 and 2 were taken from the batch of randomly generated structures and subjected to single-point energy (SPE) and full optimisation calculation, the rationale being to identify whether the less computationally demanding SPE step is a stringent enough screener to reject the high energy structures. The results are presented in Figure 6.3.

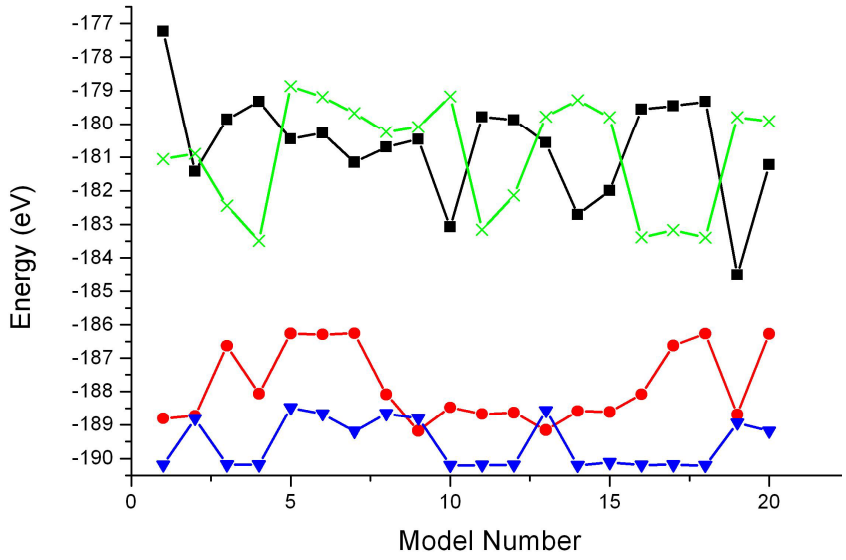

Figure 6.3 Energies obtained from the random structure acetic acid simulations. SPE calculations: box and cross and optimisations: circle and triangle for acid 1 and 2 respectively.

From Figure 6.3 it appears that whilst acid1 generated the overall lowest SPE structure, acid2 generated low SPE structures with a higher frequency, and the resulting optimised structures for this model also tended to be lower in energy. Geometrical data must also be taken into account, however. Experimentally *r*C1-O2 is 0.06 Å shorter than *r*C1-O1, implying that the hydrogen is bound to O1. Simulations show that whilst the acid1 model simulations correctly reproduce the ordering of the two CO bond lengths, the acid2 simulations consistently got it wrong. To compound this subtle effect, the acid2 simulations resulted in other heavy-atom displacements which were inconsistent with the experimental structure. Therefore the acid2 models, despite being the favoured solution on energetic grounds, are eliminated.

The acid1 geometry optimisations tended to fall into the same structure (and therefore the same energy well) (see Figure 6.4), with a heavy-atom geometry consistent with the experimental positions. In order to further explore the PES and model thermal energy for this cell, the structure found in the geometry optimisation process was taken forward for a molecular dynamics simulation. The output from this kept the same structure as found in the geometry optimisation exercise, and

added confidence to the prediction that the structure presented in Figure 6.4 is the most likely completed structure.

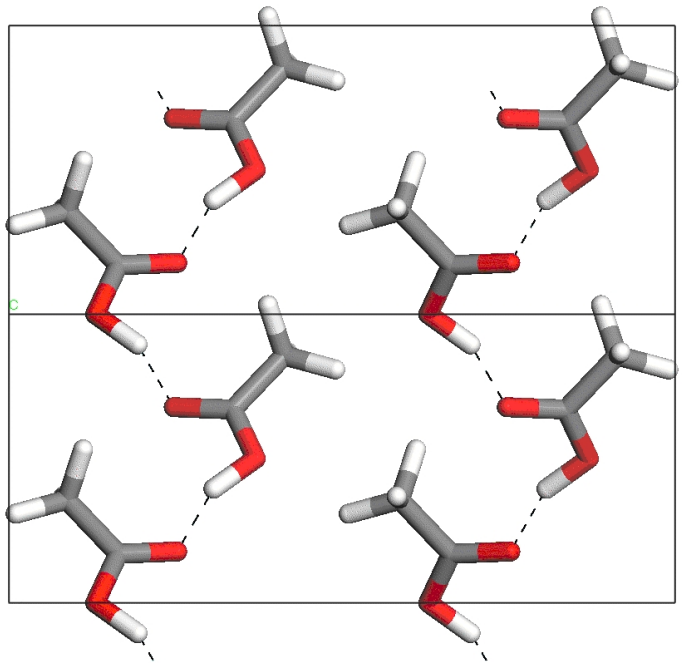

Figure 6.4 Computationally completed structure of acetic acid.

The computationally completed structure and the experimental structures of Nahringbauer[5] and Jönsson[6] show almost identical hydrogen-atom positions, with only minor differences, which can be easily accounted for with the limitations of the computational procedure (e.g. the inability of DFT to model van der Waal forces). The correct acid has been identified computationally, indicating that the random structure technique is adequate for completing structures of this nature.

6.4.2 Hydroxylamine

Forty structures of model type1 and type2 were generated at random, and subject to SPE and full geometry optimisations, with results presented in Figure 6.5.

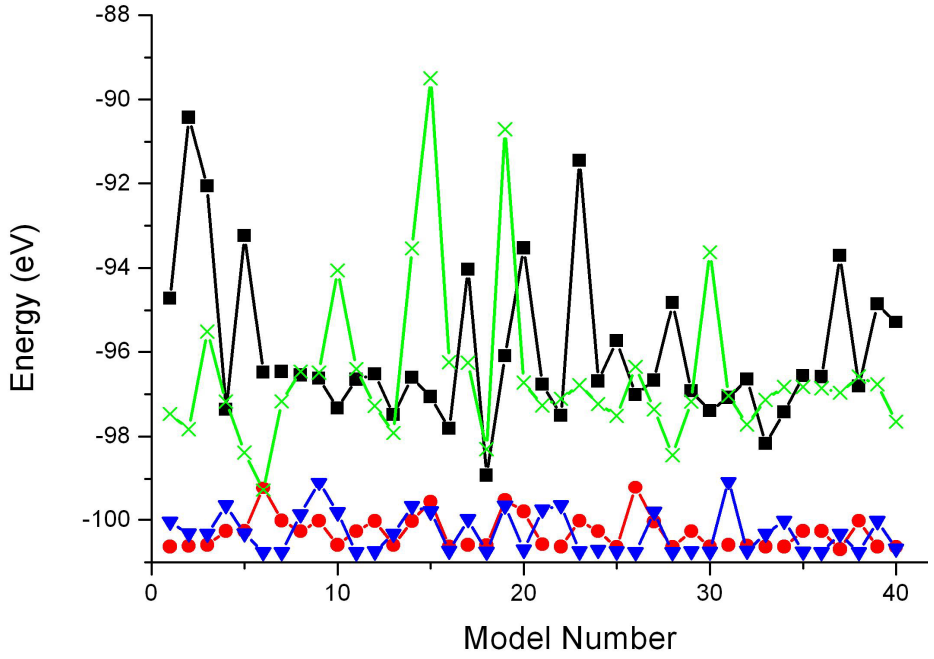

Figure 6.5 Energies obtained from the hydroxylamine simulations. SPE calculations: box and cross and optimisations: circle and triangle for type 1 and type 2, respectively.

From Figure 6.5 it is suggested that the lowest energy SPE and geometry optimisation structures were both produced from type 2 structures, However, the differences in energy are too subtle to point towards an indisputable structure, and in any case arguments must be reinforced with geometric evidence.

While a handful of low-initial-energy type 1 structures were observed in the optimisation process, only one of these did not show large heavy-atom displacements. Similarly a number of type 2 starting models gave favourable energies and minimal heavy-atom displacements, which upon close inspection of the calculation outputs revealed a common geometric minimum. On the basis of the SPE/geometry optimisation calculations, therefore, our initial bank of 40 input structures was reduced to two plausible structures, of type 1 and type 2 respectively. Interestingly, the two possible structures show many structural packing similarities (see Figure 6.6).

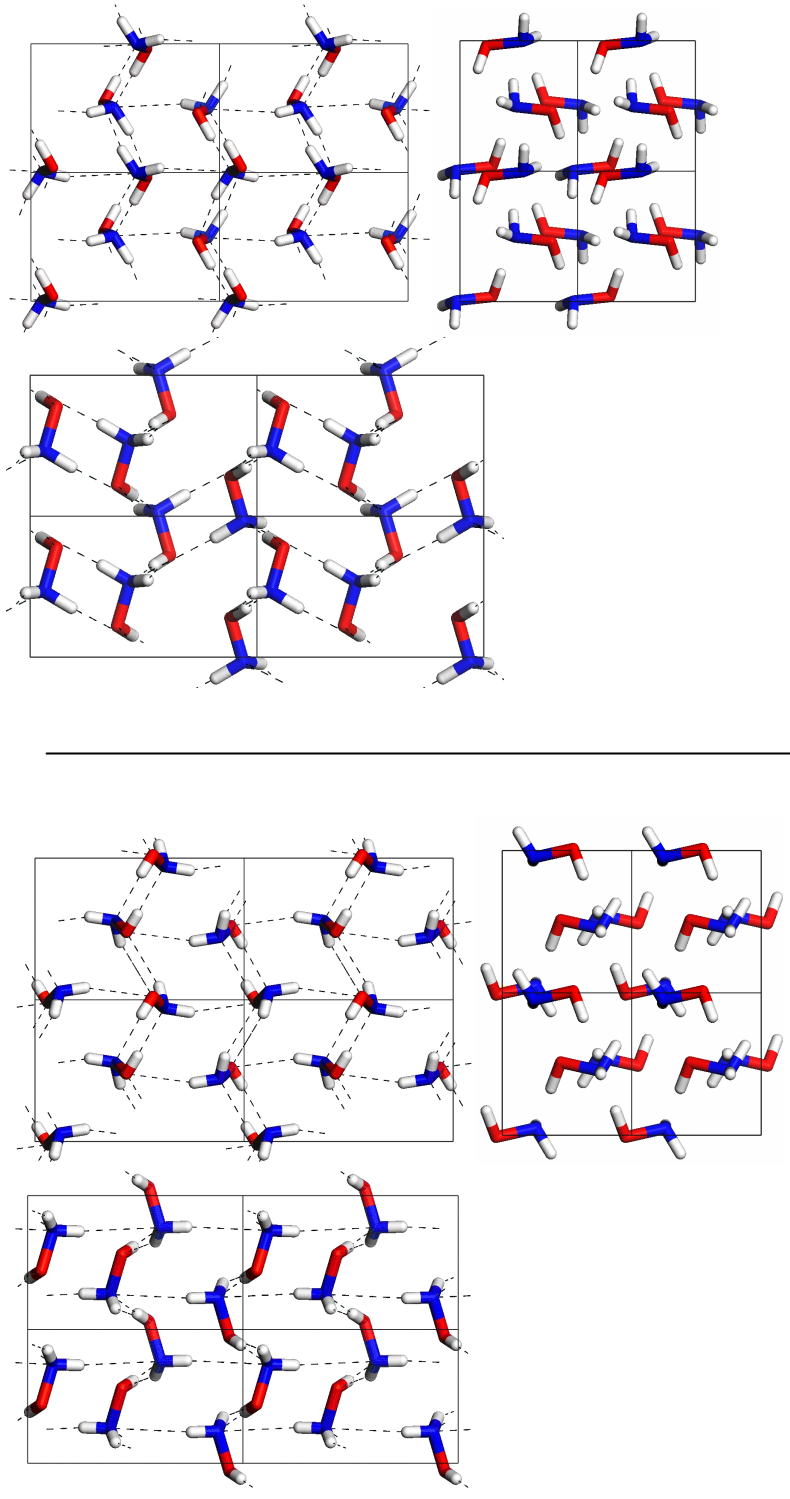

Figure 6.6 The two possible structures of hydroxylamine, type 1 (above) and type 2 6 (below) as identified by the geometry.

These two models were taken forward for use in MD simulations to include any thermal effects, following the methodology of Walker *et al.*[2] The low-temperature simulations (ca. 220 K) showed that both structures were stable, but upon increasing the temperature the type 1 structure appeared to break down, with large changes in relative heavy atom positions and orientations. This leaves the only possible solution to be the type 2 structure.

Comparing our computationally completed structure with that obtained experimentally[8,9] shows this method of sampling the PES is sufficient to complete structures where experimental data is minimal. The experimental and simulated structures appear to be very close. Of the three possible structures postulated by Lipscomb *et al.*, the resulting structure corresponds to the '(a)' model, which was also the model favoured by Jerslev[16].

6.5 Conclusions

Experimental data can be supplemented with theoretical data to complete X-ray structures with limited datasets. In this work we have applied random structure generation to provide complete input structures of the ambient pressure and temperature phases of acetic acid and hydroxylamine. From the acetic acid study it is clear that single-point energy calculations are far more valuable than optimisations. Nevertheless scrutiny of the optimisation can help highlight potential structures and, for a 0 K structure, optimisations are required. As for the hydroxylamine case SPE calculation and optimisation acted merely to suggest the most likely structures and MD simulations were required to eliminate all but one solution. The stability of a proposed model with respect to free energy can be a vital tool in completing a structure. By geometry optimisations alone hydroxylamine presented two potential structures; only upon the addition of free energy could one of these be eliminated.

The most efficient method of identifying the complete structure is initially to sweep through a large number of random structures with SPE calculations. The most promising structures are then pursued with optimisations, removing the assumptions made during the random structure generation. Optimised structures that adhere to the experimentally generated heavy-atom positions are pursued further with MD simulations to identify the presence of any local energy barriers. This latter technique may only be required if no reasonable structure can be inferred from the diffraction data or the geometry optimisation work fails to identify a unique solution.

References

[1] L. Merrill and W. A. Bassett, *Rev. Sci. Instrum.* **45**, 290 (1974).

[2] M. Walker, C. A. Morrison, and D. R. Allan, *Phys. Rev. B.* **72**, 224106 (2005).

[3] M. Walker, C. R. Pulham, C. A.Morrison, D. R. Allan, and W. G. Marshall, *Phys. Rev. B*. **73**, 224110 (2006).

[4] R. E. Jones and D. H. Templeton, *Acta Cryst.* **11**, 484 (1958).

[5] I. Nahringbauer, *Acta Chem. Scand.* **24**, 453 (1970).

[6] P.-G. Jönsson, *Acta Cryst. B* **27**, 893 (1971).

[7] E. A. Meyers and W. N. Lipscomb, *Acta Cryst.* **8**, 583 (1955).

[8] W. G. Marshall – unpublished.

[9] P. McGreggor – unpublished.

[10] Frisch, M. J., Trucks, G. W., Schlegel, H. B., Scuseria, G. E., Robb, M. A., Cheeseman, J. R., Zakrzewski, V. G., Montgomery, Jr., J. A., Stratmann, R. E., Burant, J. C., Dapprich, S., Millam, J. M., Daniels, A. D., Kudin, K. N., Strain, M. C., Farkas, O., Tomasi, J., Barone, V., Cossi, M., Cammi, R., Mennucci, B., Pomelli, C., Adamo, C., Clifford, S., Ochterski, J., Petersson, G. A., Ayala, P. Y., Cui, Q., Morokuma, K., Malick, D. K., Rabuck, A. D., Raghavachari, K., Foresman, J. B., Cioslowski, J., Ortiz, J. V., Baboul, A. G., Stefanov, B. B., Liu, G., Liashenko, A., Piskorz, P., Komaromi, I., Gomperts, R., Martin, R. L., Fox, D. J., Keith, T., Al-Laham, M. A., Peng, C. Y., Nanayakkara, A., Gonzalez, C., Challacombe, M., Gill, P. M. W., Johnson, B., Chen, W., Wong, M. W., Andres, J. L., Gonzalez, C., Head-Gordon, M., Replogle, E. S., and Pople, J. A. (1998), Gaussian 98, Revision A.7. *Gaussian, Inc., Pittsburgh PA.*

[11] G. Kresse, and J. Furthermueller, *Comput. Mater. Sci.* **6**, 15 (1996).

[12] D. Vanderbilt, *Phys. Rev. B.* **41**, 7892 (1990).

[13] J. P. Perdew, J. A. Chevary, S. H. Vosok, K. A. Jackson, D. J. Singh, and C. Fiolhais,. *Phys. Rev. B,* **46**, 6671 (1992).

[14] H. J. Monkhorst, and J. D. Pack, *Phys. Rev. B,* **13**, 5188 (1976).

[15] A. D. Becke, *J. Chem. Phys.* **98**, 5648 (1993).

[16] B. Jerslev, *Acta Cryst.* **11**, 511(1958).

Chapter 7

A Computational Study of the High-Pressure Structure of Hydroxylamine

7.1 Introduction

The water/ammonia hybrid, hydroxylamine (NH_2OH), is an important compound as it finds uses across many industries. For example it is a powerful reducing agent (i.e. anti-oxidant) and it can be used as an additive in adhesives. The salt, hydroxylammonium nitrate, is currently under investigation as a reductant for the nuclear reprocessing of plutonium and as a potential rocket fuel. Hydroxylamine is hydroscopic and can be explosive. Two fatal accidents have occurred relatively recently: the first, in Pennsylvania (1999), killed five people and destroyed a 45,000 ft^2 structure. The second occurred at the Nissin Chemical plant in Japan (2000), killed four and destroyed the plant. The associated risks of studying hydroxylamine highlight the benefits of computational modelling; to my knowledge modelling has caused no accidental fatalities.

Studying the behaviour of hydroxylamine under pressure is of interest to better understand the mechanism of explosion. For an experimental study, however, there are a number of potential problems that go beyond the issues of safe handling. There is difficulty differentiating between $-NH_2$ and -OH in diffraction studies due to the two functional groups presenting an identical number of electrons (X-ray) and similar scattering factors (Neutron). Hydrogen atoms are difficult to observe – more so in high-pressure experiments (see Chapter 2), and other experimental techniques such as vibrational spectroscopy provide little direct insight into the specific details of intermolecular bonding. To this end the diffraction and vibrational study to date[1] has failed to provide a complete understanding of the structural properties of hydroxylamine. With the experimental study yielding only partial results, it is now the turn of computational modelling to fill the gaps.

This chapter reports a computational study of high-pressure hydroxylamine. With the experimental data being so deficient, this case tests the computational techniques presented in the earlier chapters of this thesis to the limits. This is the second part of the study on polymorphism of NH_2OH. The first part is presented in Chapter 6, which demonstrated the successful identification of the ambient-pressure structure. This achievement lends support to our computational modelling approach,

thereby allowing the high-pressure analogue to be attempted with confidence. This study will begin with a complete understanding of the conformational properties of the isolated molecule, which will provide vital insight into the condensed phase structure.

7.2 The gas-phase molecular geometry of NH_2OH

Gas-phase calculations were performed to identify all possible stable conformations on the potential-energy surface (PES). At the rHF/6-311G* level a PES scan through the full range of the HNOH torsion angle (see Figure 7.1) revealed that an angle of ~120° produced the global minimum [Figure 7.2(a)], with a second minimum observed with a torsional angle of ~60° some 22.8 kJ mol^{-1} higher in energy [Figure 7.2(b)]. These two minima were separated by a maximum located 37.6 kJ mol^{-1} above the global minimum structure [Figure 7.2(c)].

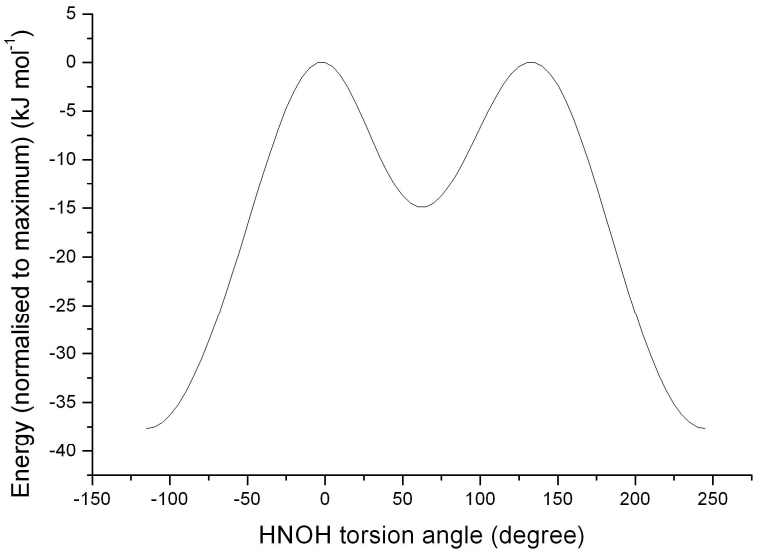

Figure 7.1 The gas-phase PES of NH_2OH, with respect to varying the HNOH torsion angle.

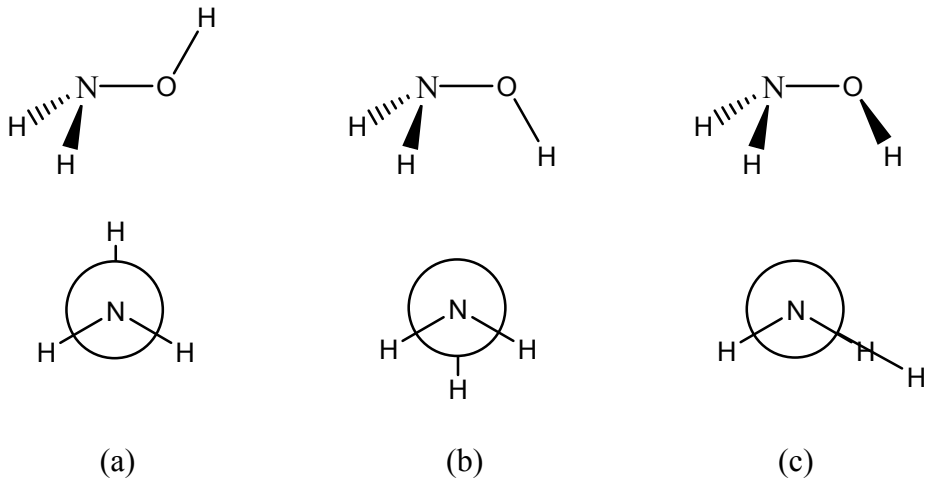

Figure 7.2. The two energy minima of hydroxylamine (a) the global minimum (referred to as 'open'), (b) a local minimum ('closed') and (c) the transition state.

Since the strength of a hydrogen bond (10-60 kJ mol^{-1} for moderate H-bonds) is comparable to the energy required to overcome this maximum it therefore follows that the molecular conformation present in the high pressure structure could be any of the three identified above (i.e. not just the global minimum). A non-biased investigation should therefore begin with sampling a large number of possible hydrogen-atom positions generated in a random fashion, as described in the preceding chapter. Also performed was a comparison of the NH_2OH molecule versus the NH_3O zwitterion, which was found to be 106.0 kJ mol^{-1} higher in energy than the NH_2OH molecule. Although this energy difference is considerable it is important to note that this simulation is gas-phase; in the condensed phases this energy difference may be compensated for by strong electrostatic interactions. A parallel may be drawn with amino acids: in an isolated state an amino acid molecule prefers the neutral form, where the carboxylate group is protonated, whereas in the condensed phases the amino group is protonated and the molecule carries a positive and negative charge. However, since the modelling techniques used are quantum mechanical in nature, should a lower energy structure exist where hydrogen transfer takes place this will automatically be modelled in our computational procedure.

7.3 Generating the trial structures for the high-pressure phase

Limited data collected from earlier X-ray and neutron diffraction studies had generated a partial solution (heavy atoms only) thought to conform to the symmetry space group Pnma.[2] The symmetry transformations described by this space group are:

(i) an n-glide [about the (¼, y, z) plane through (0, ½, ½)],

(ii) a mirror plane [the (x, ¼, z) plane],

(iii) an a-glide [about the (z, y, ¼) plane, through (½, 0, 0)],

(iv) an inversion centre [by definition through the origin (0, 0, 0)], and

(v) three 2_1 screw axes [about the (x, ¼, ¼), (0, y, 0,) and (¼, 0, z) axes and through (½, 0, 0), (0, ½, 0) and (0, 0, ½) respectively].

Systematically dropping symmetry elements can lead to a number of other space groups including $P2_12_12_1$. As evidence from the experimental study highlighted these two as the most likely candidates, our computational investigation made use of both of these to generate the input bank of starting structures. Note that as our molecular dynamics calculations will be performed in the absence of symmetry constraints, if another space group exists that gives rise to a lower energy structure then it should be sampled provided enough kinetic energy is injected into the system to overcome any barriers on the potential-energy landscape.

7.3.1 Pnma

This space group is the higher symmetry setting, and most notably forces the molecules to lie along a mirror plane. In identifying possible crystal structures that are commensurate with this setting three factors have to be considered, namely: (i) swapping the nitrogen and oxygen atom locations (giving structure types labelled type 1 and type 2), (ii) whether the molecules are assigned as 'opened' or 'closed', and (iii) reflecting in the plane normal to the *x* axis (see Figure 7.3). These operations lead to 8 basic structures, which were then completed by manually placing the hydrogen atoms using the Materials Studio graphic interface package[3]. Each structure was subjected to a single-point energy (SPE) calculation and then optimised in P1 symmetry, for ease of comparison with other symmetries. Those geometries that showed minimal heavy-atom displacements were subsequently pursued with

molecular dynamics calculations to further gauge the stabilities of the proposed structures.

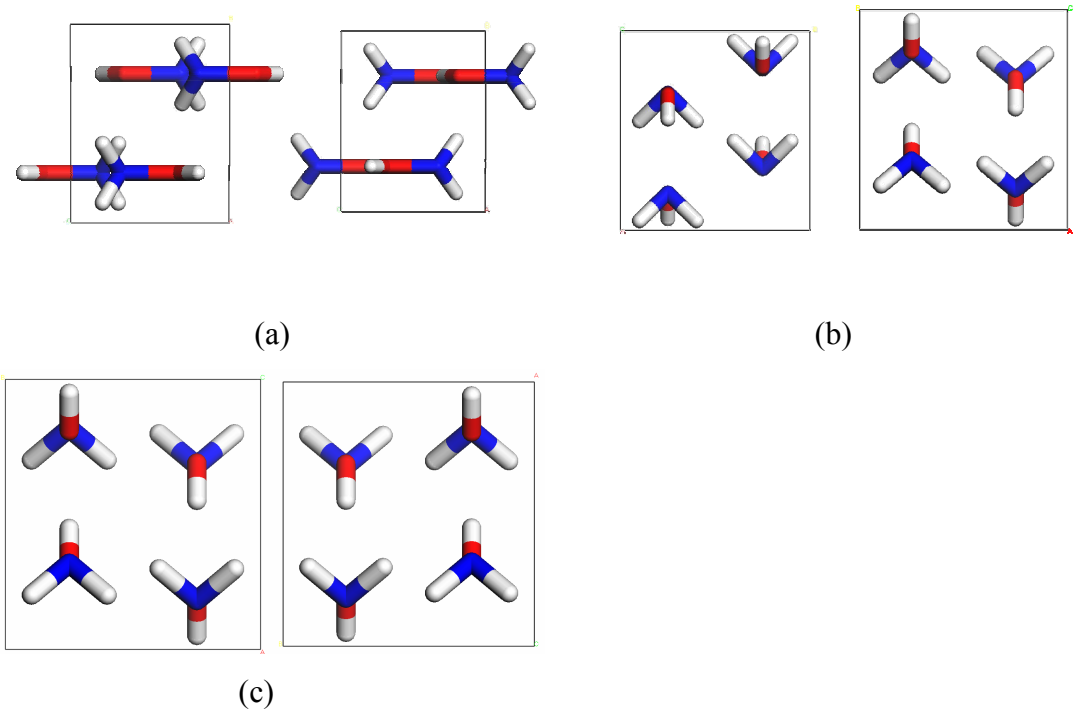

Figure 7.3 Graphical indication of (a) type 1 and type 2 structures, (b) opened and closed structures, and (c) the mirror (reflection in the plane normal to the *x* axis).

7.3.2 $P2_12_12_1$

The absence of a molecular symmetry operation in this space group allows the molecule to rotate around the N-O bond, giving rise to a much larger number of possible structures. A bank of 1200 structures were generated at random using the random structure generation code[4] for the type 1 and type 2 heavy-atom geometries (see Figure 7.4); 40 of these structures were then selected at random for our study.

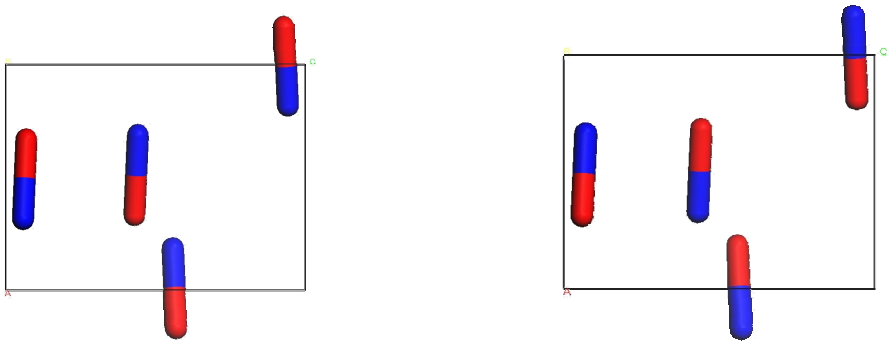

Figure 7.4 (a) Type 1 and (b) type 2 heavy atom structures conforming to space group $P2_12_12_1$.

After close examination of the optimisations a number of structures which showed promising energies (initialising below -92 eV) were used in a series of microcanonical (NVE) molecular dynamics calculations performed in the P1 space group.

7.4 Computational Methods and Procedures

Gas-phase calculations were performed using the software package Gaussian 98[5] utilising the 6-311G* basis set with restricted HF (for the PES scan) and the hybrid DFT functional B3LYP [6](for full molecular geometry optimisation). A potential-energy surface (PES) scan was performed to rotate the H-O-N-H torsion angle through 180° (symmetry can account for the full 360°), whilst allowing other parameters to optimise. An optimisation was also performed on the NH_3O molecule using the same basis set and level of theory.

Calculations with periodic boundary conditions (PBC) were performed using the VASP 4.4 simulation package[7] using a set of Vanderbilt ultrasoft pseudopotentials[8]. Plane waves were expressed to a limit of 396 eV within the PBC formulism. The generalised gradient approximation (GGA) functional PW91[9] was used to model the exchange and correlation potentials and the Brillouin zones sampled using a Monkhorst Pack grid[10] of 3x3x2. Convergence criteria were set such that optimisation was achieved once forces reached less than 10^{-3} eV $Å^{-1}$ and self-consistent field (SCF) results energy change less than 10^{-4} eV.

Microcanonical (NVE) molecular dynamics calculations (performed in the P1 space group), were subsequently undertaken on a number of optimised geometries in order to search the PES more completely and to observe the effects of free energy on the structures. The basis set energy cutoff was lowered to 297 eV, but otherwise convergence criteria and k-point sampling were identical to those used in the optimisations. The equilibrium structures were taken as starting points; each MD simulation was run using a 0.6 fs timestep, determined after careful consideration of the highest energy vibration. The simulations were allowed to accrue data over 1.2 ps, the first 0.12 ps of which, was discarded to allow each system to achieve equilibrium. Calculated vibrational spectra were obtained from a force autocorrelation and subsequent Fourier transform, using the forces obtained from each MD simulation. The first 0.24 ps of each simulation was discarded to allow each system to achieve equilibrium. Each atom type was used to generate different spectra, allowing identification of the species responsible for each vibrational mode.

Simulated annealing calculations were performed using the lowest energy non-optimised structures of type 1 and type 2. Two NVE-MD simulations with constrained heavy-atom positions were undertaken at 800 K and 200 K for 1.2 ps using the same timestep as above. After careful observation of the simulation energetics, the step which produced the highest temperature (since the simulation keeps energy constant this step represents the one in which the potential-energy well is deepest) was used to continue the simulation, by removing the forces and initialising with a new lower temperature. This simulation was regarded as complete once the temperature settled below 200 K; the highest temperature step from this run was then used to initialise an optimisation, the output from which was the final structure.

7.5 Results and discussion

7.5.1 Pnma geometry optimisations

Eight possible structures were generated with the heavy-atom positions as obtained experimentally. Each structure was subjected to a single-point energy (SPE) calculation and then fully optimised in P1 symmetry; the results are presented in Figure 7.5.

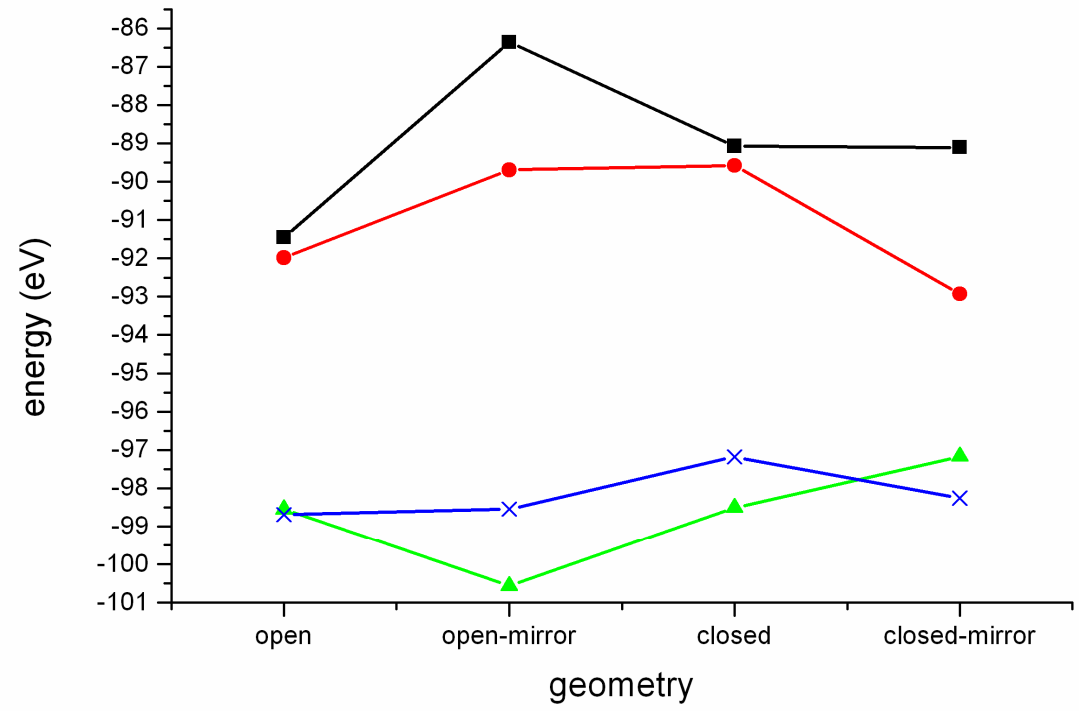

Figure 7.5 Circles represent type 1 SPEs, squares are type 2 SPEs, the crosses and triangles represent type 1 and type 2 optimisations, respectively.

Minimal information can be obtained from the SPE calculations due to the manual placement of the hydrogen atoms. The optimisations show that the two types of structures generate similar energies, with type 2 producing the lowest overall energy. Of the eight initial structures, those which displayed minimum heavy atom displacements (see Figure 7.3 for nomenclature) were:

(i) type 1 (open),

(ii) type 1 (closed, mirror),

(iii) type 2 (open, mirror),

(iv) type 2 (closed), and

(v) type 2 (closed, mirror).

All these structures remained in the Pnma space group despite removal of all symmetry constraints. Using these structures as the starting points for MD simulations (initialised at 800 K) all produced new, lower energy, structures upon twisting the H-N-O-H torsion, and thus breaking the mirror plane to conform to the lower symmetry space group, consistent with the $P2_12_12_1$ setting, the other experimental best-fit space group.

7.5.2 $P2_12_12_1$ geometry optimisations

Forty structures of type1 and type2 were taken from the batch of randomly generated structures for hydroxylamine, and subject to SPE calculation, with results presented in Figure 7.6.

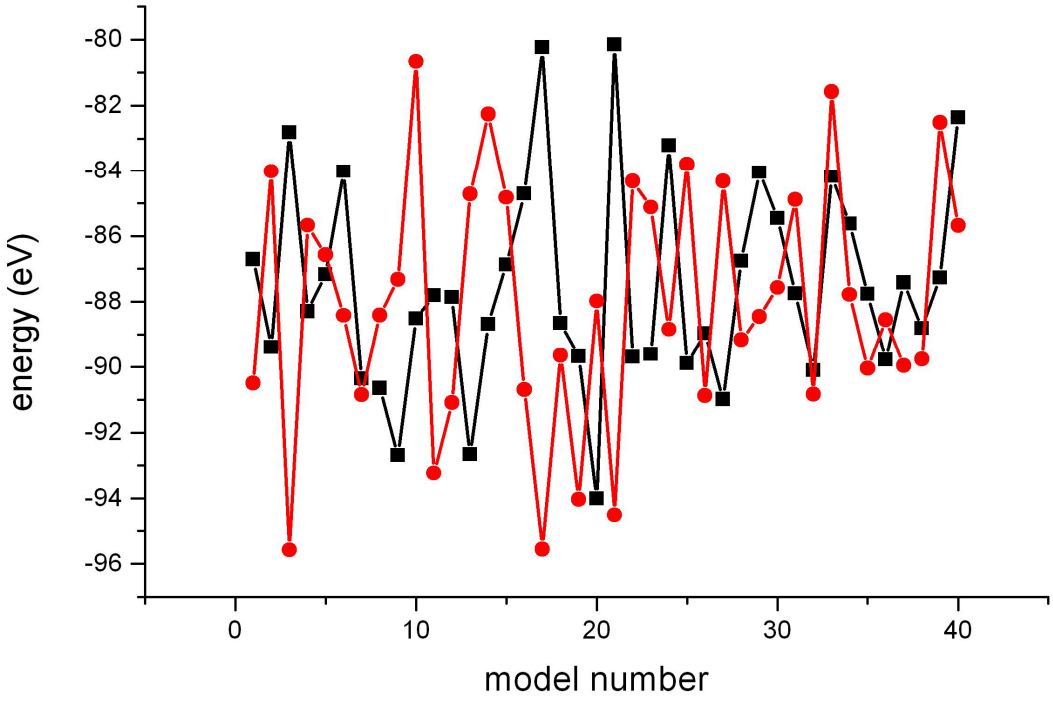

Figure 7.6. Square represents type 1 and circles type 2 SPE calculation.

Figure 7.6 shows that a type 2 structure has generated the lowest-energy point, but the type 1 structures have produced a number of feasible low-energy points. To help separate the type 1 and type 2 structures, geometry optimisations were performed on all random structures found to be more stable than -92eV. Minimal heavy-atom displacements were observed in a couple of the type 1 models and all the type 2 models, which were subsequently taken forward to the MD stage. (Note, due to the relatively low quality of the experimental data, larger atomic displacements were regarded as acceptable compared to the previous studies reported in this thesis.)

7.5.3 Molecular dynamics simulations

The results obtained from the MD simulations, performed for the collection of candidate structures found in the Pnma and $P2_12_12_1$ geometry optimisation series, revealed the intriguing result that the NH_3O zwitterion was found to be more stable than the NH_2OH form for all the crystal structures investigated. Taking the highest temperature structure obtained from the corresponding MD run, and subjecting the coordinates to a full geometry optimisation (with no symmetry constraints) the type 1 structures fell into just two unique structures, [see Figures 7.7 and 7.8 (models labelled α and β, respectively)]. The four type 2 structures yielded a single unique structure, identical to the β model found for type 1. The symmetry of the α-model was consistent with a pseudo $P2_1/m$ (within a 0.1 Å tolerance), which is commensurate with the original PNMA symmetry setting by dropping the symmetry elements (i), (iii) and two of the screw axes (v) listed in section 7.3. The symmetry of the β model adopted a pseudo-Pnma symmetry (within 0.5 Å tolerance) although a $P2_1/n$ structure symmetry was available with tighter tolerances (0.2 Å tolerance).

Whilst there are differences between the two structures, some recurring features are observed, namely the NH_3O zwitterion, the alignment of molecules into columns along the N-O axes, and each NH_3O molecule is aligned with another in the opposite direction. The differences between the two structures can be easily seen when the cell is viewed along the *y* axis: the α model is composed of non-interacting sheets, whilst the β model is composed of a fully hydrogen-bonded lattice. Repeating the MD simulation using these two structures as starting points generated no new structures, indicating that there are no other mimima accessible with the energy used in MD simulations. The atomic coordinates, experimental and calculated, are presented in Table 7.1.

A brief consideration of the one known parameter from the experimental diffraction study, namely the N-O bond length, reveals values of 1.432 and 1.429 Å for the α and β models, respectively, which compare well with the experimental values of 1.455 and 1.481 Å for the Pnma and $P2_12_12_1$ refinements respectively.

Lattice parameter/ Atomic coordinates	Pnma			$P2_12_12_1$			α model ($P2_12_12_1$)			B model ($P2_12_12_1$)		
a (Å)	5.49556			4.157			4.157			4.157		
b (Å)	5.20228			5.2189			5.2189			5.2189		
c (Å)	4.414378			5.5136			5.5136			5.5136		
O	0.6810	0.75	-0.1657	1.1676	0.9790	0.5696	1.2065	0.2489	0.1855	0.9370	0.4863	0.05389
O	0.1810	0.75	0.6657	0.6676	0.5210	0.4304	0.7097	0.2449	0.6807	0.0631	-0.0052	0.4505
O	0.8190	0.25	0.3343	-0.1675	0.4790	0.9304	0.2962	0.7446	0.8079	0.5664	0.5212	0.5559
O	0.3190	0.25	1.1657	0.3325	0.0210	0.0693	-0.2054	0.7499	0.3060	0.4363	0.9906	0.9517
N	0.6901	0.75	0.1853	0.8148	1.0162	0.5582	0.8627	0.2511	0.1668	0.5939	0.4873	0.0729
N	0.1901	0.75	0.3147	0.3148	0.4874	0.4418	0.3653	0.2455	0.6666	0.4052	0.0156	0.4322
N	0.8099	0.25	0.6853	-0.1676	0.4790	0.9304	0.6399	0.7439	0.8260	0.9078	0.4961	0.5715
N	0.3099	0.25	0.8147	0.3325	0.0210	0.0693	0.1380	0.7510	0.3264	0.0094	0.9833	0.9306
H	-	-	-	-	-	-	0.7947	0.2476	-0.0019	0.5370	0.5010	0.2610
H	-	-	-	-	-	-	0.7725	0.0878	0.2539	0.5063	0.6498	-0.0158
H	-	-	-	-	-	-	0.7764	0.4191	0.2490	0.5058	0.3156	-0.0020
H	-	-	-	-	-	-	0.2920	0.2480	0.4813	0.4611	0.0059	0.2434
H	-	-	-	-	-	-	0.2780	0.0794	0.7503	0.5083	-0.1418	0.5209
H	-	-	-	-	-	-	0.2794	0.4105	0.7531	0.4785	0.1911	0.5067
H	-	-	-	-	-	-	0.7098	0.7456	1.0122	0.9662	0.4920	0.7595
H	-	-	-	-	-	-	0.7290	0.9089	0.7413	1.0119	0.6563	0.4882
H	-	-	-	-	-	-	0.7283	0.5776	0.7420	0.9773	0.3220	0.4914
H	-	-	-	-	-	-	0.2069	0.7457	0.5124	0.5370	0.5010	0.2610
H	-	-	-	-	-	-	0.2258	0.9197	0.2465	0.5058	0.3156	-0.0020
H	-	-	-	-	-	-	0.2283	0.5888	0.2382	0.5063	0.6498	-0.0158

Table 7.1. Atomic coordinates obtained for the two experimental symmetries and the two proposed models in fractional coordinates. Note for the two experimental structures the nitrogen and oxygen identities can be exchanged.

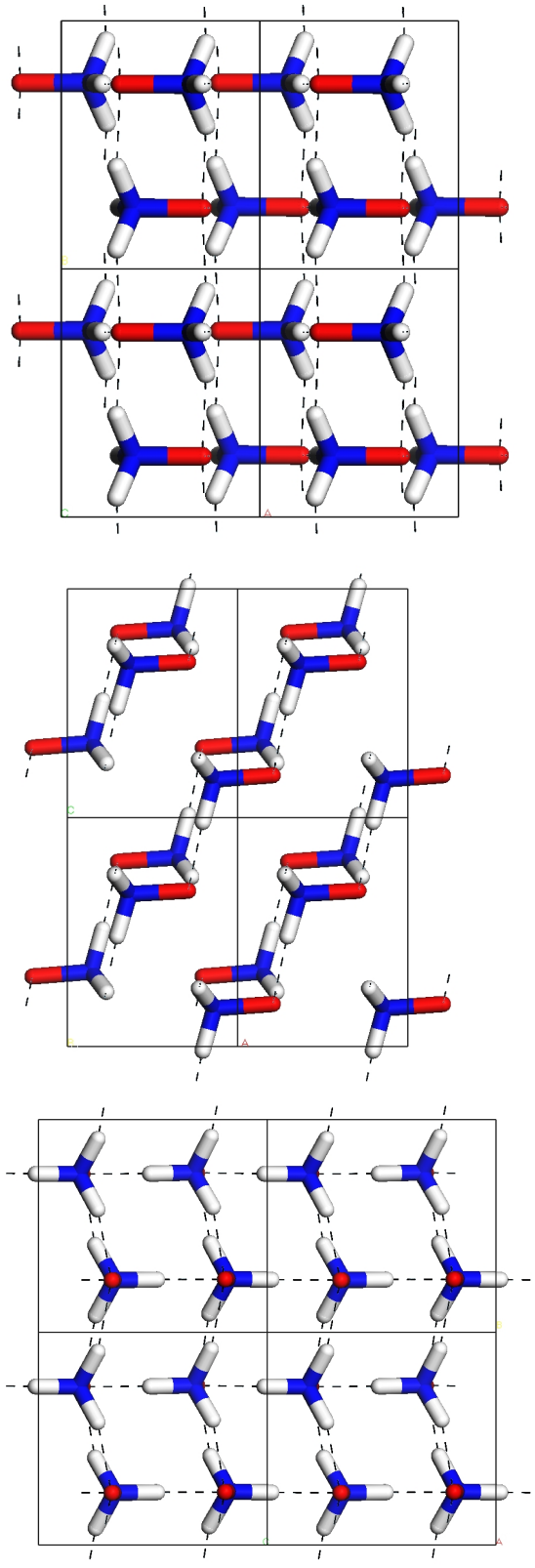

Figure 7.7 The optimised α model, viewed along the *z*, *y* and *x* axes. The energy of this structure is -100.32116 eV.

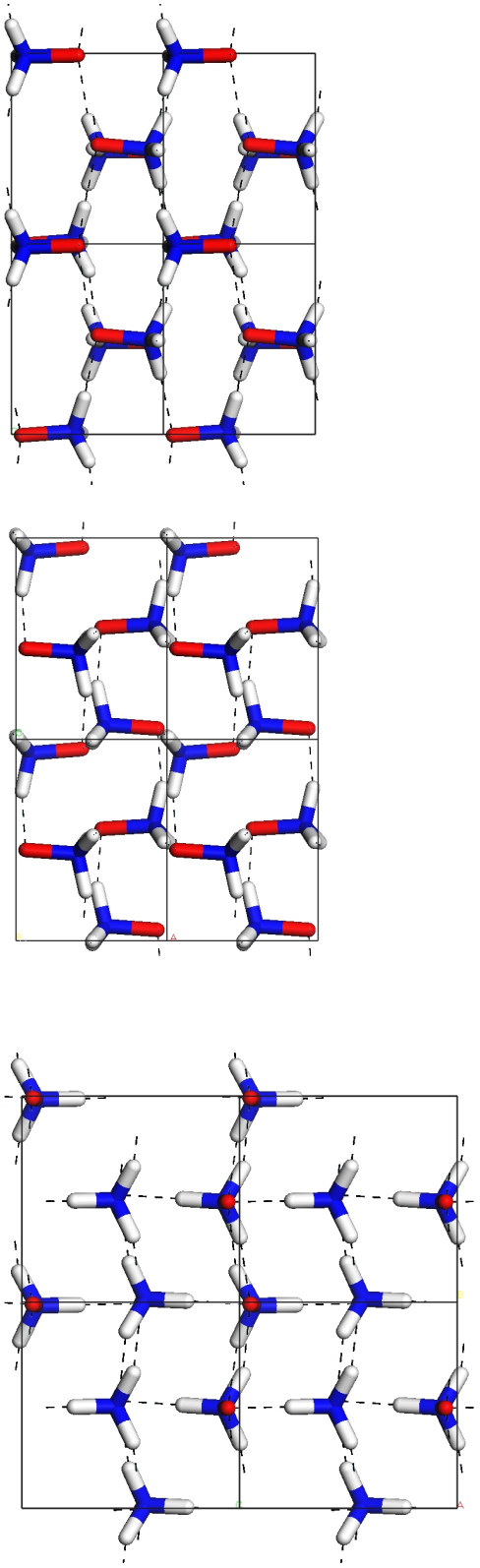

Figure 7.8 The optimised β model viewed along the *z*, *y* and *x* axes. Note this structure was obtained in several simulations, ranging in energy from -100.45699 to -100.47847 eV.

7.5.4. Simulated Annealing

To explore further whether the α and β structures identified from the MD simulations are the lowest-energy structures on the PES, simulated annealing calculations were performed. This was done by taking the lowest-energy type 1 and type 2 models identified from the batch of randomly generated structures, and depositing a large kinetic energy into the lattices via an NVE MD simulation.

The type 1 structure resulted in an amorphous structure, even after optimising all coordinates. To check the dependence on the initial structure used, a second simulated annealing simulation was performed, initialised from the next lowest energy type 1 structure. Similarly, the symmetry from this simulation was lost, resulting in a structure with 25% of molecules in the NH_2OH form while the remainder converted to the NH_3O zwitterion. This mixture of conformations remained even after geometry optimisation of the final MD structure. Furthermore, the remaining NH_2OH is not in a geometry that will directly allow transfer of the hydrogen atom to a neighbouring molecule to create a complete NH_3O structure. For the sake of completeness, further calculations were performed to manually 'force' the structure to completely NH_3O. Subsequent optimisations (of firstly just the hydrogen atoms and then the entire structure) showed further instabilities and the structure returned to an amorphous state. The second type 1 simulated annealing resulted in another amorphous structure with a higher energy still, highlighting the complex nature of PES, showing that simulated annealing is not always the best means to explore a structure. Simulated annealing starting from the type 2 models regenerated the β model found in the MD investigation.

It therefore follows from an intensive computational modelling program including random structure generation, geometry optimisation, molecular dynamics and simulated annealing that two models, labelled α and β have been identified. Of special interest is that both structures relate to NH_3O, rather than the NH_2OH form present in the ambient-pressure polymorph.

7.5.5 Calculated Vibrational Spectra

Whilst the experimental vibrational data previously obtained could not by themselves identify the structure of the high-pressure phase, and since our computational study has highlighted two possible structures (with significantly different three-dimensional patterns of hydrogen bonding), it may be possible that the experimental data can now be put to good use and identify the more likely structure.

Following the methodology used in previous chapters, vibrational spectra were extracted from the MD simulations for both the α and β models. For comparison a Gaussian calculation (B3LYP/6-311G*) was performed on the NH_3O zwitterion, which indicated C_{3v} symmetry and a N-O bond length of 1.351 Å . The vibrational frequencies obtained are shown in Table 7.2.

Frequency (cm^{-1})	Symmetry	Description
934	A_1	N-O stretch
1202	E	ONH bend
1639	A_1	ONH symmetric bend
1694	E	HNH bend
3106	E	N-H stretch
3147	A_1	N-H symmetric stretch

Table 7.2. Gas-phase vibrations of the NH_3O zwitterion

For the α model (which corresponds to an N-O bond length of 1.432 Å) the calculated vibrational spectrum is shown in Figure 7.9.

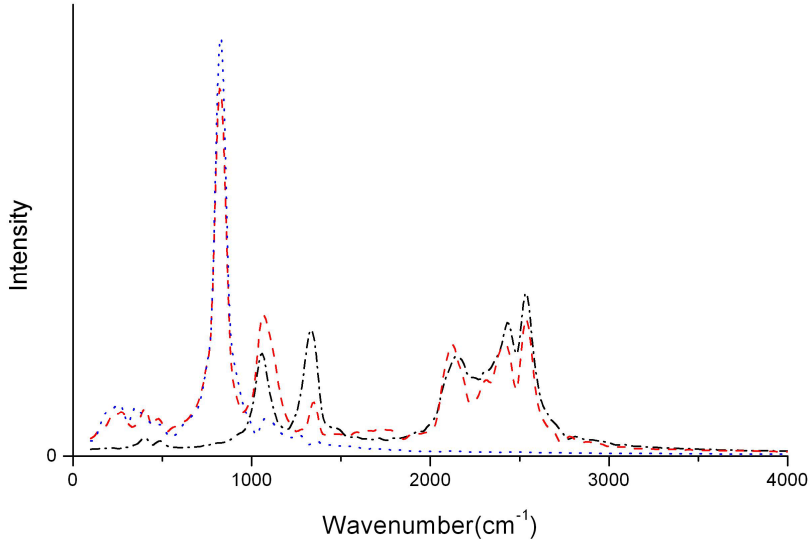

Figure 7.9 Calculated vibrational spectra for the α model. The dotted line represents oxygen vibrations, the dashed line nitrogen vibrations and the dot dashed line hydrogen vibrations.

As a quick comparison, the gas-phase calculation predicts vibrational bands in four distinct regions, which is also observed in our calculated solid state vibrational spectrum. In the α model the N-O bond vibrates at 830 cm^{-1}, some 100 cm^{-1} lower than in the gas phase, which can be attributed to the longer, weaker N-O bond. The next vibration, at 1080 cm^{-1} is the O-N-H bend, followed by a band at 1330 cm^{-1}, which is attributed to the O-N-H symmetric and H-N-H bends. The remainder of the frequencies are banded together in the N and H vibrations above 2100 cm^{-1}. Note that the gas-phase frequencies can only be used as a guide in interpreting the solid-state spectra as frequencies will red shift upon condensing due to hydrogen bonding weakening N-H interactions.

The calculated vibrational spectra for the β model shows a peak pattern similar to the α model, but, the peaks are blue shifted by some 200+ wavenumbers (Figure 7.10).

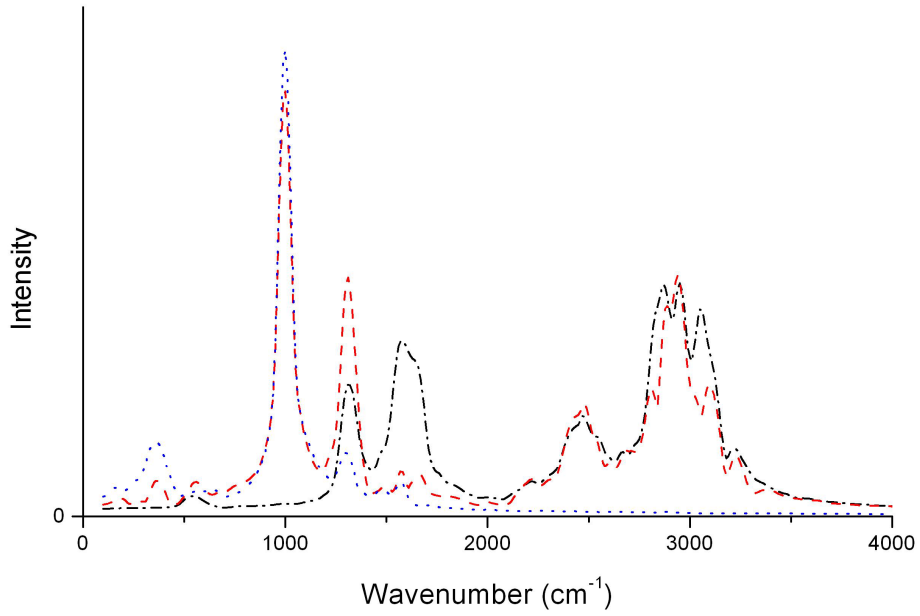

Figure 7.10. Calculated vibrational spectra for the β model. The dotted line represents oxygen vibrations, the dashed line nitrogen and the dot dashed line hydrogen.

The N-O stretch now vibrates at 1000 cm^{-1} despite a similar N-O bond length (1.429 Å) to the α model. The O-N-H bend now occurs at 1310 cm^{-1}, whilst the O-N-H symmetric bend and H-N-H bend occur at 1580 cm^{-1} and 1660 cm^{-1}. Once again the remaining vibrations are indistinguishable. However, the highest is above 3000 cm^{-1} compared to the α-model highest of 2540 cm^{-1}. For a simple comparison Figures 7.9 and 7.10 have been reduced to the same axis and showing all atomic motions in one line (see Figure 7.11), where the blue shift of the β model can be seen clearly.

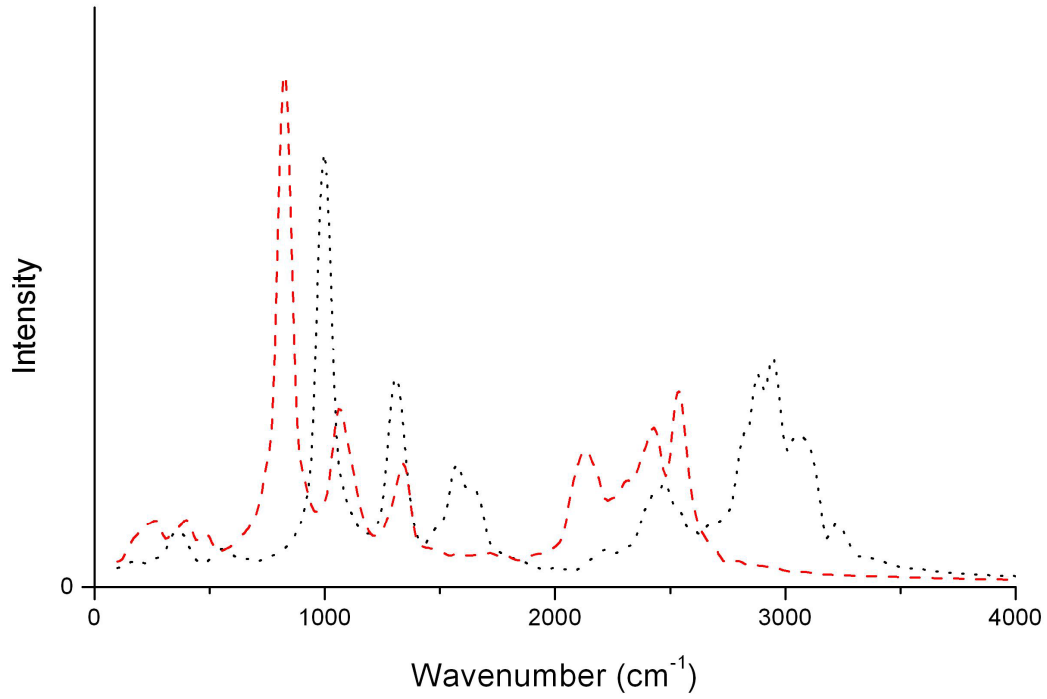

Figure 7.11. Comparison of the calculated vibrational spectra for the two proposed structures. The dashed line represents the α model whilst the dotted line represents the β model.

The difference in the two models can largely be explained by the electrostatic forces. The α model has better aligned dipoles, increasing the electrostatic forces in this model and increasing the negative charge on the oxygen atoms. This in turn improves its ability to act as a hydrogen-bond acceptor (A). Since a strong H---A bond can be regarded as weakening the donor (D) D-H bond, a lower N-H vibrational frequency is expected. In the α model the N-O distance is also longer, indicating a weaker bond, and so a lower frequency is also expected. In any case group theory predicts that all vibrations of A_1 and E symmetry will be Raman active. The experimental Raman spectrum of NH_2OH under pressure reported a clear N-O stretch at 985 cm^{-1}, which is very close to that of the β-model (1000 cm^{-1}, c.f. α model 830 cm^{-1}), leading to the conclusion that the only structure that fits the available dataset is the β model.

7.6 Conclusions

Unless the crystal is a high-energy polymorph, the NH_2OH molecule can be eliminated, as energy studies suggest that an NH_3O zwitterion is the most stable form at high pressure. Since the original motivation in studying the high pressure behaviour of hydroxylamine was to help shed light on the possible mechanism of explosion, these results suggest that proton transfer could be implicated. From the simulations the most likely proposed structure is the β model, which was observed five times from random structures and once from simulated annealing. A second structure, the α model, is observed only once, from type 1 starting structures. The α model is slightly higher in energy and shows many similarities to the β model. However, as the α model is composed of sheets of NH_3O molecules, van der Waal interactions (which are omitted in DFT-based calculations) will play some part in stabilising this structure, which may possibly overcome the 15.1 kJ mol^{-1} difference in energy. The closeness of energy between these two structures and the quality of the diffraction data available prevents clear structural assignment on diffraction data alone. Raman spectroscopy clearly indicates the N-O vibration of the high-pressure polymorph resonates at a frequency of 985 cm^{-1}, which is concordant with only one of our proposed models, allowing a definite structure to be proposed. An exhaustive computational study has therefore allowed completion of an experimentally incomplete structure. Although time-consuming and requiring a number of techniques, this work has completed a long time ‘bug bear’ of the Edinburgh of University Structural Chemistry Research Group and has shown that, even with minimal experimental data, simulations can be used to complete the picture.

References

[1] C.R. Pulham, P. McGregor, W. G. Marshall, unpublished work.

[2] T. Hahn, International tables volume A, 4th ed. Kluwer academic publishers (1996).

[3] Material studio graphical interface package version 2.2, Accelrys (2002).

[4] M. Walker and C. A. Morrison, manuscript in preparation.

[5] Gaussian 98, Revision A.7 M. J. Frisch, G. W. Trucks, H. B. Schlegel, G. E. Scuseria, M. A. Robb, J. R. Cheeseman, V. G. Zakrzewski, J. A. Montgomery, Jr., R. E. Stratmann, J. C. Burant, S. Dapprich, J. M. Millam, A. D. Daniels, K. N. Kudin, M. C. Strain, O. Farkas, J. Tomasi, V. Barone, M. Cossi, R. Cammi, B. Mennucci, C. Pomelli, C. Adamo, S. Clifford, J. Ochterski, G. A. Petersson, P. Y. Ayala, Q. Cui, K. Morokuma, D. K. Malick, A. D. Rabuck, K. Raghavachari, J. B. Foresman, J. Cioslowski, J. V. Ortiz, A. G. Baboul, B. B. Stefanov, G. Liu, A. Liashenko, P. Piskorz, I. Komaromi, R. Gomperts, R. L. Martin, D. J. Fox, T. Keith, M. A. Al-Laham, C. Y. Peng, A. Nanayakkara, C. Gonzalez, M. Challacombe, P. M. W. Gill, B. Johnson, W. Chen, M. W. Wong, J. L. Andres, C. Gonzalez, M. Head-Gordon, E. S. Replogle, and J. A. Pople, Gaussian, Inc., Pittsburgh PA (1998).

[5] Becke, A. D., *J. Chem. Phys.* **98**, 5648(1993).

[6] G. Kresse and J. Furthmueller, *Comp. Matter. Sci.,* **6**, 15 (1996).

[7] D. Vanderbilt, *Phys. Rev. B,* **41**, 7892 (1990).

[8] J. P. Perdew, J. A. Chevary, S. H. Vosko, K. A. Jackson, D. J. Singh and C. Fiolhais, *Phys. Rev. B,* , **46**, 5571 (1992).

[9] H. J. Monkhorst and J. D. Pack, *Phys. Rev. B,* **13**, 5188 (1976).

Chapter 8

Conclusions and Future Work

8.1 Conclusions

Minimum-energy structures can be of pivotal importance to structural chemists and lead towards rational material design. In many cases experimental techniques will completely identify the structure. However, where 'extreme' conditions are used, the experimental dataset can become restricted. It is here that theoretical techniques can be used to supplement experimental data by calculating minimum-energy structures given a partial experimental parameter set.

Structure optimisations are a valid means for locating a local energy minimum but are biased by the initial structure used and often fail to find the global minimum. Optimising a range of different starting geometries to generate a number of possible structures is one technique to probe the PES, but caution is required as the lowest-energy structure obtained in this way may not be a realistic one. MD simulations can work as a dual probe, crossing small energy barriers and testing the stability of a model with respect to free energy. It was in this way that sodium formate, nitric acid monohydrate, nitric acid dihydrate, acetic acid and the ambient pressure polymorph of hydroxylamine were studied. For all these cases the computational modelling generated a structure which, when compared to neutron diffraction data, matched experimental results.

The high-pressure polymorph of hydroxylamine has proved particularly difficult to study by experimental means. Prior to theoretical treatment studies by X-ray diffraction, neutron diffraction and vibrational spectroscopy were undertaken but each failed to elucidate the structure completely. Simulations generated two complete structures which were both energetically feasible and stable to the addition of free energy. Elimination of one of these structures was only possible by comparing the calculated N-O stretch with the actual experimental value. Taking this structure back to the neutron scattering pattern showed a promising fit, and overall the structure has been validated.

The work presented in this thesis therefore demonstrates the synergistic relationship that can exist between theory and experiment to find solutions in difficult cases.

8.2 Future Work

The work presented in this thesis could be extended in a number of directions:

1. There are many incomplete structures this technique can be applied to. For example there is second high-pressure hydroxylamine polymorph for which experimental data have been collected but the structure yet to be solved.
2. Metadynamics is another tool used by researchers to cross energy barriers and may prove useful. The basic principle behind metadynamics is that a short MD simulation probes the shape of the local minimum. A Gaussian function is then used to fill this potential energy well. The two steps are then repeated, allowing the simulation to cross higher energy barriers than just MD simulations alone. Low-frequency vibrational modes may make the MD step in these simulations prohibitively long, however, but a test case may prove useful for comparison.
3. Genetic algorithms have proved useful at predicting crystal structures from scratch. The work presented in this thesis uses some experimental data and simulation to complete complex structures. The two methods could be combined to allow the calculation of structures with only minimal experimental input.
4. Protein crystallography structures are generated with no hydrogen-atom data. The positions are inferred based upon the heavy-atom geometry and valence shell electron pair repulsion theory (VSEPR theory), or otherwise ignored. Whilst full DFT simulations are unlikely to prove fruitful on a sensible time scale, in principle the techniques shown in this thesis could be used with simpler force-field modelling methods. This would be quick and easy to test by repeating one of the known structures shown in this thesis. However, in

larger simulations it will be harder to detect any lower-energy structures from simulation (damping from rest of structure) but it is conceptually possible.

Appendix 1
Papers published

1. M. Walker, C.A. Morrison and D.R. Allan, Nitric Acid Monohydrates at High Pressure: An Experimental and Computational Study, Phys. Rev. B., 2005, 72, 224106.

2. M. Walker, C.R. Pulham, C.A. Morrison, D.R. Allan and W.G. Marshall, Nitric Acid Dihydrate at Ambient and High Pressure: An Experimental and Computational Study, Phys. Rev B., 73, 224110.

3. M. Walker, C.A. Morrison, D.R. Allan and W.G. Marshall, A new high pressure phase of sodium formate dihydrate; an experimental and computational study, Accepted by Dalton Transactions.

4. M. Walker and C. A. Morrison, Completing the structure: supplementing limited experimental diffraction data with theory, soon to be submitted to Acta Crystallographica section A.

5. M. Walker, C.R. Pulham, C.A. Morrison, D.R. Allan and W.G. Marshall, An Experimental and Computational study of the High Pressure structure of Hydroxylamine, Manuscript in preparation.

Appendix 2

Conferences and meetings attended

Hydrogen bonding and DFT (2004, Lyon, including a poster)

MSSC (2004, Imperial college London, including a poster)

USIC (2005, Glasgow, including a poster)

CCP5 (2005, Cardiff, including a poster)

DFT (2005, Geneva, including a poster)

BCA spring meeting (2006, Lancaster, including a presentation)

Appendix 3

Courses and lectures attended

UNIX 1, 2 and 3 (two day courses)

HTML (two day course)

Scientific visualisation (three day course)

Inorganic chemistry firbush (three, two day seminars)

School of chemistry inorganic/material chemistry seminars

Selected physics seminars

Effective writing (two day course)